RICE UNIVERSITY

Vulnerability Assessment of Coastal Bridges Subjected to Hurricane Events

by

Navid Ataei

A THESIS SUBMITTED
IN PARTIAL FULFILLMENT OF THE
REQUIREMENTS FOR THE DEGREE

Doctor of Philosophy

APPROVED, THESIS COMMITTEE

Dr. Jamie E. Padgett, Chair
Assistant Professor of Civil and
Environmental Engineering

Dr. Philip B. Bedient
Herman Brown Professor of Civil and
Environmental Engineering

Dr. Satish Nagarajaiah
Professor of Civil and Environmental
Engineering and Mechanical
Engineering and Material Science

Dr. Pol D. Spanos
Lewis B. Ryon Professor of Mechanical
Engineering and Material Science and
Civil and Environmental Engineering

HOUSTON, TEXAS
April 2013

ABSTRACT

Vulnerability Assessment of Coastal Bridges Subjected to Hurricane Events

by

Navid Ataei

Bridges are the most critical components of the transportation network. The functionality of bridges is important for hurricane aftermath recovery and emergency activities. However, past hurricane events revealed the potential susceptibility of these bridges under storm induced wave and surge loads. Coastal bridges traditionally were not designed to sustain hurricane induced wave and surge loads; and furthermore, no reliability assessment tool exists for bridges exposed to this hazard. However, such a tool is imperative for decision makers to evaluate the risk posed to the existing bridge inventory, and to decide on the retrofit measures and mitigation strategies.

This dissertation offers a first attempt to quantify the structural vulnerability of bridges under coastal storms, offering a probabilistic framework, input tools, and application illustrations. To accomplish this goal, first an unbiased wave load model is developed based on the existing wave load models in the literature. The biased is removed from the load models through statistical analysis

of the experimental test data. The developed wave load model is used to evaluate the response of coastal bridges employing single-physics domain Dynamic numerical models. Additionally, a high fidelity fluid-structure interaction model is developed to take into account the significant intricacies, such as turbulence, wave diffraction, and air entrapment, as well as material and geometric nonlinearities in structure. This numerical model provides insight on the influential parameters that affect the response of coastal bridges. Moreover, a Monte Carlo based Static Model methodology is developed to enable fast evaluation of the bridge deck unseating mode of failure. This methodology can be used for fast screening of vulnerable structures under hurricane induced wave and surge loads in a large bridge inventory.

New statistical learning tools are used to develop fragility surfaces for coastal bridges vulnerable to storms. The performance of each of these tools is evaluated and compared. The statistical learning approaches are used to enable reliability assessment using the more rigorous finite element models such as the Dynamic and FSI Models which is important for improved confidence and retrofit assessment. Additionally, a new systematic method to evaluate the limit state capacity functions based on the post-event global performance of the bridge structure is developed.

The application of the developed reliability models is illustrated by utilizing them for Houston/Galveston Bay area bridge inventory. The case study of Houston/Galveston Bay area reveals that more than 30% of bridges have a high probability of failure during an extreme hurricane scenario event. Two vulnerable bridge structures from the case study are selected to investigate the effect of different potential retrofit measures. Recommendations are made for the most appropriate retrofit measures that can prevent the deck unseating without significantly increasing the structural demands on other components.

Acknowledgements

This work is supported by Houston Endowment through SSPEED Center at Rice University, and also Shell Center for Sustainability. I gratefully acknowledge Houston Endowment, SSPEED Center, and Shell Center for Sustainability for the financial support of my research.

Many thanks go to my advisor Dr. Jamie Padgett for her support and encouragement throughout my research. It has been a privilege and my good fortune to work under the supervision of Dr. Padgett. Her inspiration and motivation will guide me for many years.

I would also like to thank my thesis committee Dr. Philip Bedient, Dr. Satish Nagarajaiah, and Dr. Pol Spanos. Dr. Bedient is the director and PI of the SSPEED Center, and I had the great opportunity to collaborate with him. I had the chance to take classes offered by Dr. Nagarajaiah and Dr. Spanos, which greatly improved my understanding of dynamics and vibrations, and helped me with my research.

My experience in graduate school has been great because of my great friends. They know how thankful I am for having them as my friends. I am grateful for having great officemates, Jay and Emily. I would also like to give a special

thank to my roommate, Jaime. I would like to extend my gratitude toward my friends: Keivan, Isaac, Srivishnu, Dharma, Behzad, Fabio, Meriad, Yenny, Ario, Candase, Soroush, Mihela, Zhenghua, Kameshwar, and many other friends that I have been associated with. I also appreciate all my friends outside of Rice University for all of their support during these years.

I would like to express my deep gratitude towards my parents for their unconditional support and wise advices throughout my life. Further, I would like to thank my future fiancé (!), Heather, for always being there even when she was not. Finally, I would like to thank my best friend and my sister, Nina.

Thank y'all!

Contents

List of Figures

List of Tables

Nomenclature

A	area
A_A	AASHTO coefficient for impact load
A_{brg}	bearing area of the anchor
A_g	girder area
A_N	anchor projected failure surface
A_{No}	anchor far from edges projected failure surface
A_p	pile end area
A_s	reinforcement area
A_{se}	bolt cross section area
A_{si}	pile side area
B_A	AASHTO equation parameter for impact load
C	capacity
C_d	drag coefficient
C_m	inertia coefficient
c	undrained cohesion strength of soil
$c_{h\text{-}va}$	Douglass horizontal wave load coefficient
c_r	Douglass coefficient for internal girders

$c_{v\text{-}va}$	Douglass vertical wave load coefficient
cov	coefficient of variation
D	structural demand
DS_j	j^{th} damage state
d_A	abutment displacement
d_{Ay}	abutment yield displacement
d_b	deck height
d_g	girder height
d_p	pile diameter
d_s	water depth during the storm
d_{se}	reinforcement diameter
d_w	wavemaker displacement
d_{w0}	wavemaker peak displacement
EDP	vector of engineering demand parameters
EDP	engineering demand parameter
E_{fi}	failure event of i^{th} span
e	error
e_1	model error for first damage state
e_2	model error for second damage state

e_3	model error for third damage state
$\mathbf{F}$	force vector
F_c	connection capacity
F_D	drag force
F_f	friction force
$F_{H\text{-max}}$	maximum quasi-static horizontal wave load
F_I	inertia force
FN	false negative
F_n	normal force
FNR	false negative rate
FP	false positive
FPR	false positive rate
F_s	AASHTO impact force
F_V	vertical wave load
$F_{V\text{-max}}$	maximum quasi-static vertical wave load
F_{Vt}	total AASHTO vertical force with model error
F	goodness of fit measure for classification
$\mathbf{f}$	body force
f_s	pile skin friction strength

f_{us}	steel ultimate strength
f_y	steel yield strength
f'_c	concrete compressive strength
$f_j(\bullet)$	j^{th} capacity limit state function
$G(\bullet)$	limit state function
G_j	j^{th} global performance measure
g	gravitational acceleration
H	wave height
$H_{\max}$	maximum wave height
H_s	significant wave height
h_{ef}	effective length of anchor
I	turbulence intensity
$\mathbf{IM}$	intensity measure vector
IM	intensity measure
j	parameter's index number
K	structural stiffness
k	turbulence kinetic energy
k_c	concrete breakout strength factor
L	constant in Longuett-Higgins joint PDF

L_H	hydraulic diameter
L_p	pile length
L_s	span length
l	lower bound for uniform distribution
l_d	development length
l_{emb}	embedment length
lim_j	j^{th} limit state
$\mathbf{M}$	mass matrix
m	wave number
m_0	first spectral moment
m_n	median value of normal distribution
m_l	median value of lognormal distribution
$\mathbf{N}$	normal vector
N_b	breakout strength of anchor far from edges
N_{cb}	breakout strength of anchor
N_g	number of girders
N_p	unmodified pullout strength of anchor
N_{pn}	pullout strength of anchor
N_s	steel breaking strength of anchor

N_{sim}	number of simulation
N_T	number of trees in random forest model
n	number of spans
n_1	wave number parameter for wavemaker
n_b	Number of bolts per span
P	precision
$\mathrm{P}[\bullet]$	probability
P_F	system level probability of failure
P_n	casted vote from the n^{th} tree
$P_{f\text{-}i}$	probability of failure of i^{th} span
p	pressure
Q_d	compression capacity of pile
Q_f	skin friction capacity of pile
Q_p	end bearing capacity of pile
q	end bearing strength of pile
R_H	horizontal strength of the system
R_V	vertical strength of the system
r	rail height
$\mathbf{s}$	intensity measure realization

TAF	trapped air factor in AASHTO equations
TN	true negative
TP	true positive
T_p	wave period
TPR	true positive rate
$\overline{T}$	mean wave period
t	time
t-z	pile axial load transfer curve
$\mathbf{u}$	fluid velocity vector
u	upper bound for uniform distribution
$u_{\max}$	maximum uplift
u^*	maximum skin friction displacement
V	volume
V_{sk}	shear key strength
W	deck width
W_s	span weight per unit length
$\overline{W}$	geometric parameter in AASHTO equations
$x,\ y,\ z$	spatial axes
$x_A,\ y_A$	geometric parameters in AASHTO equations

Z_c	relative surge elevation
α	API coefficient for cohesive soils
β_A	AASHTO coefficient for vertical wave force
$\beta_0, \beta_1, \beta_2$	regression coefficients
γ	unit weight
γ_{ld}	reinforcement size factor for development length
γ_w	water unit weight
Δ_b	bias removal function for AASHTO equation
Δ_{bV}	bias removal function for vertical Douglass
Δ_{bH}	bias removal function for horizontal Douglass
δG_j	reduction in the j^{th} global performance measure
δK	reduction in the lateral stiffness
δR_V	reduction in the vertical strength
δR_H	reduction in horizontal strength
ε	turbulence rate of dissipation
ε_1	model error term for AASHTO equation
ε_2	model error term for concrete breakout strength
ε_3	model error term for anchor pullout strength

$\varepsilon_{\max}$	maximum axial strain
ζ	standard deviation of normal distribution
η	free water surface
$\eta_{\max}$	maximum elevation of free water surface
κ	logarithmic standard deviation
λ	wave length
λ_c	lightweight concrete modification factor
μ	coefficient of friction
μ_d	dynamic coefficient of friction
μ_s	static coefficient of friction
ν	bandwidth of the wave spectral density
ξ	dimensionless wave height
ρ	density
ρ_c	concrete density
ρ_s	steel density
ς	dimensionless wave period
$\boldsymbol{\sigma}$	stress tensor
Φ	cumulative standard normal function

$\boldsymbol{\varphi}$	fluid velocity potential
φ_b	bond strength between concrete and steel
φ_s	shear design reduction factor
$\boldsymbol{\psi}$	stream function
ψ	cohesion to effective overburden pressure ratio
ψ_2,ψ_3	concrete breakout modification factor
ψ_4	anchor pullout modification factor
ω_A	geometric parameter in AASHTO equations

Chapter 1

Introduction

1.1. Background

More than 50% of the U.S. population lives within 50 miles of the shoreline, and development continues to occur at a rapid pace in regions susceptible to coastal hazards (Crossett et al. 2004). This results in heavier dependence upon the coastal transportation network as well as heightened development and siting of bridges in hazard prone regions. The performance of the bridge infrastructure in these regions is critical to support the safety and vitality of coastal communities. Only recently has the performance of coastal bridge infrastructure during hurricane events become a central focus of research studies. One of the contributing factors to this delay includes the ability to evacuate before hurricane landfall and hence a limited

threat of fatality due to bridge collapse (Ataei et al. 2010). However, the substantial damage to roads and bridges during Hurricane Katrina (44 highway bridges damaged) (NIST 2006) has highlighted to potential inhibition to post-disaster emergency response, reentry and recovery activities for a region, as well as substantial direct and indirect economic losses from a non-functioning transportation system. For example, the total losses during Hurricane Katarina, considering all direct and indirect losses, e.g. job losses, are estimated to exceed $100 billion (Mosqueda et al. 2007). Bridges were revealed to be the most vulnerable critical component of the transportation system, suffering damage during hurricane induced storm surges and wave loads (Figure 1-1), and costing a total of $1billion (Padgett et al. 2008) for repair and replacement alone without considering indirect consequences.

Figure 1-1. Damages to US-90 Bridge across Biloxi Bay during Hurricane Katrina (Padgett et al. 2008).

The occurrence of coastal bridge damage in hurricane induced storm surge events is not isolated to the 2005 Hurricane Katrina. In retrospect to the history of hurricanes, one can find many bridges that were fully destroyed or severely damaged. Bridges were destroyed during Hurricane Camille (1969), at Escambia Bay, FL during Hurricane Ivan (2004) (Douglass et al. 2004), in Hokkaido, Japan during the Songda Typhoon (2004) (Okada et al. 2006), and in Houston/Galveston, TX during Hurricane Ike (2008) (Stearns and Padgett 2010). Moreover, global climate change influencing sea level rise (ICF 2007), could likely yield more coastal bridges susceptible to inundation or surge and wave loading during future hurricanes.

Despite the above mentioned facts, there is currently no reliable method to probabilistically assess the vulnerability of existing bridge inventories in hurricane prone zones. Most research has addressed the estimation of wave and surge loads on bridge superstructure (Chen et al. 2009; Cuomo et al. 2009; Douglass et al. 2006; Huang and Xiao 2009; Jin and Meng 2011; Schumacher et al. 2008), identification of reconnaissance lessons and assessment of empirical data for limited bridges (Mosqueda et al. 2007; Padgett et al. 2008; Robertson et al. 2007), or hindcasting the previous hurricane data and prediction of storm wave and water surge in coastal regions (Chen et al. 2009; Chen et al. 2007). However, probabilistic

models of bridge vulnerability are essential to assess the risk posed to existing bridge inventories and to make decision about retrofitting of susceptible ones. The goal of this research is to provide a framework for reliability assessment of coastal bridges under hurricane induced wave and surge loads that can be further employed in risk assessment and loss estimate packages.

1.2. Goals and Scope

A central goal of this research is to provide viable methods for deriving fragility surfaces for coastal bridges under hurricane events, in support of regional risk assessment and mitigation. A fragility surface provides the conditional probability of failure (or survival) for a structural system given the hazard intensity. The fragility assessment can be presented in the form of Equation (1-1).

$$P_F = \mathrm{P}\left[\mathrm{G}(C, D) \le 0 \mid \mathbf{IM}\right] \tag{1-1}$$

where P_F is the probability of failure of the structure under the given mode of failure, G is the limit state function, C is the structural capacity, D is the structural demand, and **IM** is the vector of hazard intensity measures. This probability of failure can be plotted against **IM** to provide a visual interpretation of structural reliability under different hazard condition, known as a fragility

surface. Decoupling the hazard from the structural reliability allows for the application of the developed fragility surfaces to different hazard models. Therefore, if the probabilistic hazard models are updated in future, they can be integrated with the proposed structural reliability model.

Coastal bridges traditionally were not designed to sustain hurricane induced wave and surge loads; and furthermore, no reliability assessment tool exists for bridges exposed to this hazard. However, such a tool is imperative for decision makers to evaluate the risk posed to the existing bridge inventory, and to decide on the retrofit measures and mitigation strategies. The unique contributions of this research are as follows:

- Providing systematic methodologies to analyze and evaluate the response of coastal bridges under hurricane wave and surge;
- Offering probabilistic models for uncertainties involved in the capacity and demand modeling;
- Employing these methods for construction of fragility surfaces of coastal bridges;
- Comparing these methodologies in terms of accuracy and computational efficiency;

- Assessing the effectiveness of potential retrofit measures for bridges susceptible to coastal storms.

1.3. Dissertation Outline

This dissertation is organized into ten chapters. A brief overview of each chapter is provided here.

- **Chapter 2** provides a literature review which ranges from evaluation of hazard parameters, estimation of wave and surge forces, and reviewing the existing probabilistic studies on the performance of coastal bridges under hurricane-induced wave and surge.

- **Chapter 3** presents the existing wave and surge load models for coastal structures with an emphasis on coastal bridges. The basic foundations of fluid dynamics that are employed in the evaluation of wave forces are also revisited in this chapter. Additionally, bias removal functions and model error terms are developed for the wave load models.

- **Chapter 4** describes and compares alternative finite element modeling strategies for coastal bridges and provides validation of the developed

models through comparison with the experimental test data. This chapter offers insight into viable modeling strategies for coastal bridges.

- **Chapter 5** describes hazard and structural random variables. The most influential hazard parameters are determined as intensity measures that the bridge failure probability will be conditioned upon. Also, a comprehensive sensitivity study is performed in order to identify the significant parameters that their uncertainty should be considered in the reliability analysis. Appropriate probability distribution functions for these random variables are defined. Also, the sampling strategy that is used in this research is described in this chapter.
- **Chapter 6** provides methods to evaluate the reliability of coastal bridges under hurricane induced wave and surge loads. This chapter combines the random variables with the developed numerical models in Chapter 4 to provide the reliability assessment framework of coastal bridges. Additionally, a Monte Carlo based Static Model for rapid screening of bridges vulnerable to the deck uplift failure mode is introduced in this chapter.
- **Chapter 7** presents different statistical learning methods that can be used to classify the categorical data. These methods are applied to evaluate the

fragility models of coastal bridges for the deck unseating failure mode. The accuracy of different structural modeling approaches is compared with each other after utilizing these statistical learning methods to the outcome of the simulations.

- **Chapter 8** presents the potential retrofit measures for coastal bridges subjected to hurricane wave and surge to prevent the deck unseating. This chapter also introduces a new systematic method to derive the capacity limit state functions for retrofitted bridges based on the post-event global performance.
- **Chapter 9** demonstrates the application of the proposed reliability frameworks for coastal bridges subjected to hurricane events by applying the developed methods to the Houston/Galveston Bay area bridge inventory. Additionally, this chapter evaluates the effectiveness of different retrofit measures on the deterministic response as well as their impact on the fragility response of the two vulnerable bridges in the case study region.
- **Chapter 10** summarizes the contributions of this dissertation, and proposes the prospect of future work related to reliability and risk assessment of coastal bridges vulnerable to storm surge and waves.

Chapter 2

Literature Review

This chapter presents a state of the art review of the existing studies on the performance of coastal bridges under hurricane induced wave and surge loads. First a review of wave and surge hindcasting is provided. The wave and surge hindcasting (and forecasting) provides the input hazard data that can be used for reliability assessment of coastal bridges. Also, reconnaissance reports on the coastal bridges damages observed in the past hurricane events are presented in this chapter. Additionally, experimental and numerical studies on the evaluation of wave and surge forces on bridges are reviewed in this chapter. Finally, the concepts of reliability assessments are briefly reviewed.

2.1. Wave and Surge Hindcast and Forecast

The literature on the evaluation of wave and surge is briefly reviewed to provide perspective on the input hazard modeling that can be potentially coupled with the fragility models developed in this dissertation. To conduct risk assessment of coastal bridges, the fragility of the structure should be integrated with the probabilistic hazard models. If the probabilistic hazard estimates are not available, the risk assessment can be performed for scenario events. As an example, a sample risk assessment for residential buildings under hurricane can be found in Kennedy et al. (2011).

One of the main focuses of past research on coastal storms is on the evaluation of the storm surge and wave caused by hurricanes (Chen et al. 2009; Chen et al. 2007; CHG 2011). The main objective of these studies is to provide a system that can hindcast the expected values of surge and wave height for the past hurricane event accurately. These models can be used later to develop probabilistic hazard models and also to forecast the wave and surge from future hurricanes (FEMA 2010). An accurate forecast of storm surge is useful for local officials to define the mandatory and recommended evacuation zones. Also, these predictions can be used to update the flood maps for any given areas, and to support the

zoning of the coastal regions (FEMA 2010). Most of the models for evaluation of wave and surge values along the US Gulf Coast are developed in finite element or finite difference software packages. These models cover a large area of the land and ocean with relatively large grid size. The grid size significantly reduces in nearshore regions and points of interest such as channels and rivers (Chen et al. 2007; Xu et al. 2007). These models are briefly reviewed here since the wave and surge scenario events that will be utilized in Chapter 9 to assess the risk of Houston/Galveston Bay area bridges are generated based on the similar models.

Xu et al. (2007) presents the numerical simulation for hindcasting waves generated by Hurricane Juan. They employ SWAN (Simulating WAves Nearshore) (2010) software nested with WAVEWATCH-III. The generated waves are compared to the in situ buoys data. This work suggests that an accurate wave prediction is highly dependent on accurate simulations of storm winds. Chen et al. (2009) work presents the surge values hindcast of Hurricane Katrina. They couple ADCIRC (2010) and SWAN (2010) to calculate the wave height and surge elevation. The results of the developed model agree with the observed data at selected buoys.

One of the major projects, in order to update the flood maps along the gulf Coast is performed by FEMA and Army Corps of Engineers (FEMA 2010). The preliminary report on surge values and flood maps has been released for the state of Texas (FEMA 2010). Simulations of wave and surge are performed by coupling ADCIRC (2010) and SWAN (2010) software packages on a super-computer system at University of Notre Dame. A detailed finite element model of Texas and Louisiana coastal regions is constructed using the LiDAR data. The simulations for over hundred different hurricane scenarios are performed using different wind field properties generated by sampling over a joint probability distribution of wind field parameters, known as the Joint Probability Method (JPM). The JPM provides the parametric wind properties that can be used in a computer simulation to define the maximum surge elevation and its associated probability, based on five hurricane parameters:

1. Central pressure;
2. Radius of maximum wind speed;
3. Hurricane forward speed;
4. Landfall location;
5. The angle of the storm track relative to the coast.

One of the main controversies of the traditional JPM is the lack of sufficient data to develop a five dimensional joint probability function. Also, in the application of JPM, it is assumed that the storm characteristics are constant near the coast, which is not a valid assumption. The JPM is modified in the FEMA draft report to overcome some of the shortcoming of the original model (FEMA 2010). This new model, referred to as JPM-OS, provides the mean probability densities of the wind field data, as well as the dispersion. After obtaining the wind field data, a deterministic analysis provides the storm surge values. The probability of this storm surge is evaluated by numerical integration of the convolution of storm surge output and the five dimensional joint probability distribution of storm parameters. The final outcome of this work for Texas coastal region could be used to evaluate the probabilistic hurricane wave and surge hazard models for Houston/Galveston Bay area.

2.2. Reconnaissance Reports on the Vulnerability of Coastal Bridges

Field evidence of the vulnerability of bridges from past hurricanes has been documented in reconnaissance reports. One of the first report on the vulnerability

of coastal transportation systems is provided by Douglass et al. (2004). This report illustrates observed damages to roads and bridges during Hurricane Ivan. Different damages, including scour, barge impact, and deck unseating have been observed in the field (Douglass et al. 2004). These observations suggest that the existing coastal road system is highly vulnerable to hurricane events.

The Mosqueda et al. (2007) study investigates post-disaster field reconnaissance of the Gulf Coast immediately following Hurricane Katrina. In this study, structural damages to bridges are examined. Bridge span shifting and unseating is one of the common damages that was observed in Hurricane Katrina. Erosion at bridges' abutments also caused disruption of service. In some cases, bridge structures remained intact but were inaccessible because approaches were washed out.

The study by Padgett et al. (2008) categorizes observed damages to bridge infrastructure during past hurricanes. The most common and the most severe failure mode for bridges is the unseating of individual spans due to wave and surge-induced loading. Impact of barges and oil rigs is another source for potential damage in coastal regions. For instance, during Hurricane Katrina, the eastbound I-10 Pascagoula Bridge was impacted by a barge and a tugboat, which led to

extensive damage to the bridge. Another possible type of damage is scour and erosion of the abutment, or slope failure. Also, the equipments of movable bridges were severely damaged due to water inundation in past hurricane events. In many cases, water inundation destroyed lift motors, rendering structurally sound bridges immovable.

Although the earthquake and hurricane are completely different natural hazards, some similarities exist in type of damages from both hazards (Padgett et al. 2008). Bridge deck unseating during Hurricane Katrina, which resulted in a considerable amount of damage and losses, is also a common problem in seismic events. The observations indicate that using simple details, such as transverse shear keys, could help to mitigate the damage and to minimize the repair costs (Padgett et al. 2008).

Okeil and Cai (2008) study twelve bridges to document the damage caused by Hurricane Katrina. Different types of bridges, such as railroad, movable, steel, and concrete bridges are surveyed. The authors conclude that storm-surge induced forces can easily overcome measures taken for anchoring existing bridges, since short and medium spans are rarely designed for uplift forces (Okeil and Cai 2008). This study suggests that the best solution to prevent extensive damages to coastal

bridges is to build the new structures above the highest storm surge level. Also, some recommendations on the repair or strengthening of vulnerable bridges are provided. Similar to the previous study, the authors suggested the introduction of shear keys for coastal bridges, which appear to reduce the possibility of unseating (Okeil and Cai 2008).

A report on the performance of the water crossing bridges in the Houston/Galveston Bay area after Hurricane Ike is presented by Stearns and Padgett (2010). Other reports on the performance of the engineered structures during coastal storms (NIST 2006; Rees 2010; Robertson et al. 2007), and collapse mechanism of a case study bridge (Okada et al. 2006) also exist in the literature. These reports also lead to similar conclusions and recommendations that are in line with the previously mentioned references. A summary of the potential damages to coastal bridges based on the reconnaissance reports is shown in Figure 2-1. The bridge deck unseating is one of the predominant modes of failure according to the past reconnaissance studies. However, there is no reliability model to assess the potential of this mode of failure. This dissertation provides different reliability models that can be used to evaluate the deck unseating probability of failure.

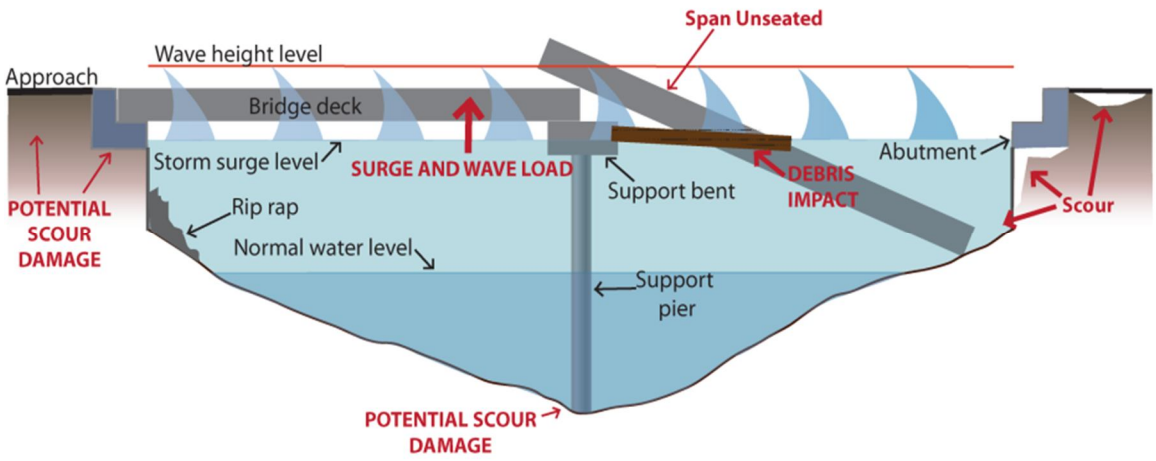

Figure 2-1. Potential damages to coastal bridges subjected to hurricane induced wave and surge loads.

2.3. Wave and Surge Loads on Bridge Decks

One of the major focuses of many studies on coastal bridges is on the evaluation of wave and surge forces on bridge decks. Petroleum and oil industries have devoted considerable effort to study the effects of wave loads on offshore platform decks. Hence, many of the approaches for estimating the wave loads on bridge decks are developed based on the available formulations for offshore structures. However, considering the fact that coastal bridges are typically located in shallow bodies of water with unique design features, the application of these models to coastal bridges is questionable and has received increased attention in recent years. One of the first related studies on wave forces was carried out by Kaplan et al (1995). The Kaplan et al. (1995) study proposes a mathematical model for estimating the forces

on cylinders and plates of offshore structures. Kaplan et al. (1995) method is based on the Morison equation (1950) that includes drag and inertial terms. This approach estimates the forces for offshore platforms with large clearance between deck and still water level. Hence, it is not appropriate for coastal bridges, as they typically have smaller clearance. In addition, the Morison equation is valid when the structural members' dimensions are very small in comparison to wave length, which is not the case for coastal bridges. Therefore, recent studies focus on the coastal bridges geometry in evaluation of wave forces.

The Cuomo et al. (2009) study investigates the role of the trapped air under the bridge decks through experimental testing. The experimental set-up consists of a 1:10 Froude scale model of a concrete girder-type bridge. The model is subjected to a series of wave loads with differing water depths, wave periods and heights, and deck opening configurations (Cuomo et al. 2009). The pressure at different locations along the bridge deck is recorded during the test. The effect of cavity in the deck is evaluated by opening the pre-designed holes in the deck. The water pressure on the bridge deck reduces when the opening size is small; however, large openings do not change the water pressure. Nevertheless, the total force should decreases as the opening size increases due to the reduction of area. This research,

though valuable, does not provide insight on the total wave and surge loads; since local pressures are only reported.

Schumacher and his colleagues (2008) present a new experimental method to evaluate the wave forces on bridge decks. The scale of the experimental test is relatively large (1:5). Also, the horizontal stiffness of bridge substructure can be varied by a guide system to reflect different substructures. Based on the preliminary results of this research, it is revealed that both horizontal and vertical forces are larger for the flexible substructure (Schumacher et al. 2008). This is not necessarily anticipated since it is commonly assumed that the rigid structure would attract higher forces. This research is still ongoing and more results are expected in early future (Schumacher et al. 2012).

The report by Douglass et al. (2006) on wave loads provides an extensive literature review of available methods to calculate wave forces on bridge superstructures. This report presents a case study conducted on the US-90 Bridge at Biloxi Bay damaged during the 2005 Hurricane Katrina and estimates the wave forces using various existing wave force prediction methods that have been derived for similar structures such as jetties. Finally, based on experimental testing conducted at Texas A&M in a wave basin, this report proposes new equations to

estimate maximum horizontal and vertical forces on bridge decks (Douglass et al. 2006). These equations are based on the assumption that wave forces are linearly proportional to the "hydrostatic reference load," which is the equivalent force acting on the bridge deck if there is air on the other side of the deck. These equations provide a simple method to rapidly evaluate the peak forces on the bridge decks. The proposed equations by Douglass et al. (2006) are specifically developed for coastal bridges and will be examined in more details in the following chapter.

The Marin and Sheppard (2009) study develops a mathematical model to predict the forces on bridge decks due to storm surge and wave loads in the time domain. The proposed model breaks the wave loads into components of drag, inertia, buoyancy, and slamming forces. The basis of their method builds on the Kaplan et al. (1995) work and the Morrison equation (1950). However, they improve the estimation by adding the added mass computations and discretizing the domain. The proposed algorithm was tested with field data of the I-10 Escambia Bay Bridge and gave acceptable agreement (Marin and Sheppard 2009). The findings of this study form the foundation of the equations that are used in the development of AASHTO (2008) equations. AASHTO (2008) equations provide

the peak horizontal and vertical loads on bridge decks. Similar to the Douglass et al. (2006) equations, AASHTO equations are also specifically developed for coastal bridges. AASHTO (2008) and Douglass et al. (2006) equations are fully presented in the next chapter.

Most of the existing literature provides the peak vertical and horizontal wave forces on bridge decks. Although this information is valuable in preliminary risk assessment, complete time histories of wave forces are required for detailed nonlinear dynamic analysis of coastal bridges. Besides AASHTO equations for wave loads on bridges, this research also utilizes fluid-structure interaction (FSI) models to capture the inherent intricacies involved in the wave and surge loads and to provide more insight on the response of the bridges as well as estimation of wave forces. One of the relevant FSI models for the evaluation of the wave forces is presented here.

Huang and Xiao (2009) study develops a 2D numerical model for calculation of wave loads on bridge deck. The numerical model is based on Reynolds–averaged Navier-Stokes (RANS) equations for the main flow. Turbulence is added to the equation by using the $k-\varepsilon$ turbulence model. Another important problem to

tackle here is the boundary condition. The free surface boundary equation is shown below (Huang and Xiao 2009):

$$\frac{\partial \eta}{\partial t} + u_j . \nabla \eta = 0 \tag{2-1}$$

where η defines the free surface level and u_j is the fluid velocity in the j^{th} direction. To solve the governing equations, a uniform rectangular mesh is generated, and values for velocity, pressure, and turbulence parameters are calculated at the center of each cell. The equations are divided with respect to time and are solved using finite difference method. The model is applied to the I-10 Escambia Bay Bridge that was damaged during Hurricane Ivan. The results show that the uplift force on the deck is more than the weight of the deck. Consequently, the bridge deck had to be displaced and unseated, as observed in the event aftermath.

2.4. Probabilistic Studies and Reliability Assessment

2.4.1. Fragility Assessment of Structural Systems

Fragility of a structural system provides the conditional probability of failure (meeting or exceeding a damage state) for given hazard parameters, known as intensity measures (*IM*s). In other words, the probability of structural demand

exceeding a damage state under a given combination of hazard can be estimated. As mentioned in Chapter 1, the general from of fragility can be written in the form of Equation (1-1), repeated here for convenience:

$$\mathrm{P}\left[DS_j \mid \mathbf{IM}=\mathbf{s}\right] = \mathrm{P}\left[\mathrm{G}(C,D)=0 \mid \mathbf{IM}=\mathbf{s}\right] \tag{2-2}$$

where DS_j is the j^{th} damage state of structural system with corresponding capacity limit state C and $\mathbf{s}$ is a realization of intensity measures. The structural fragility can be integrated with the probabilistic hazard models to estimate the risk. More holistically, the fragility model can be used to evaluate the probability of loss (Ellingwood and Wen 2005):

$$\mathrm{P}\left[\mathrm{Loss}\right] = \mathrm{P}\left[\mathrm{Loss}|DS_j\right]\mathrm{P}\left[DS_j \mid \mathbf{IM}=\mathbf{s}\right]\mathrm{P}\left[\mathbf{IM}=\mathbf{s}\right] \tag{2-3}$$

where 'Loss' is an appropriate loss metric. The term P[**IM**=**s**] is a measure of the intensity of the hazard and can be evaluated using the probabilistic hazard model; P[DS_j|**IM**=**s**] is the structural fragility; and P[Loss|DS_j] is the conditional probability of loss (Ellingwood and Wen 2005). The goal of this study is to characterize the fragility P[DS_j|**IM**=**s**]. Decoupling the loss estimate into its components as shown in Equation (2-3) allows for the application of the developed reliability models to different hazard and loss models in different regions.

Therefore, if the probabilistic hazard models are updated in future, they can be integrated with the proposed structural reliability model to assess the risk.

Fragility curves have been developed for earthquake hazard to support seismic risk assessment. Example fragility models can be found in Ellingwood and Kinali (2010) for steel frame buildings, in Nielson and DesRoches (2007) for highway bridges, and in Padgett and Desroches (2009) for retrofitted highway bridges, to name a few. However, there are no similar fragility models for hurricane-induced wave and surge hazard.

2.4.2. Reliability Assessment of Coastal Bridges under Hurricane Hazard

Only a few probabilistic studies on the performance of coastal bridges exist in the engineering literature. Meng and Jin (2007) present a method to calculate the wave forces on the bridge superstructure by integrating the pressure on the superstructure surfaces. They propose a simplistic probabilistic model by considering the wave height as the only random variable. Therefore, the proposed method can only be employed for a particular scenario with given water surge elevation. A Rayleigh distribution is used for the wave height. To obtain the pressure, the velocity (and subsequently pressure) potential function is solved in

the x-z plane by finite difference method. The probability of failure, which is defined as the exceedance of wave forces form the deck weight, is estimated for the I-10 Escambia Bay Bridge in their study. The water level is assumed to be at the bridge deck level. Based on the presented calculations in this study, the probability that the wave uplift load exceeds the self weight for this bridge during Hurricane Katrina is over 70% (Meng and Jin 2007).

Padgett et al. (2009) study provides empirical fragility curves for bridges damaged during Hurricane Katrina. Most bridges has simply supported concrete superstructure with a small clearance. The correlation between damage and different hazard and bridge parameters is investigated by using multivariate logistic regression. The number of spans and surge elevation highly correlate to the increasing level of damage (Padgett et al. 2009).

2.5. Summary

This chapter reviewed the literature corresponds to the performance of coastal bridges under hurricane wave and surge as well as the evaluation of hurricane-induced wave and surge hazard. The hurricane-induced wave and surge hazard models are required to assess the risk posed to coastal bridges. Advanced numerical

models for evaluation of wave and surge have been developed for different coastal regions. These models are briefly reviewed in this chapter since they could establish the foundation for the probabilistic hazard models in future. The potential application of the hurricane wave and surge models for risk assessment is illustrated in Chapter 9 for Houston/Galveston Bay area bridge inventory.

A summary of the reconnaissance reports on coastal bridges performance after hurricane events is also provided in this chapter. The predominant structural damage is the bridge deck unseating. Also, severe damage is expected from the impact of barges and other floating objects to the bridge structure.

The research on estimation of wave and surge loads on bridges is still ongoing. Main findings from the past research on wave loads are presented in this chapter. The previously developed wave load equations for offshore platforms are not applicable to the coastal bridges due to their different geometry. Two main wave load models that are specifically developed for coastal bridges are presented in AASHTO (2008) and Douglass et al. (2006). A comparison of the forces predicted by these two methods with the past experimental test data is presented in the next chapter and new bias removal function are developed.

Finally, the review of past literature reveals that there is no reliability assessment framework for coastal bridges. A reliability framework is required for coastal bridges in order to support the risk assessment and mitigation, lifeline route evaluation and retrofit selection and prioritization. The following chapters of this dissertation are aimed towards developing reliability assessment of coastal bridges to support the aforementioned objectives.

Chapter 3

Modified Wave and Surge Loads on Coastal Bridges

This chapter first reviews the basic concepts of computational fluid dynamics, which are the fundamentals for evaluation of hydrodynamic forces on any structures. This includes an overview on Navier-Stokes equations and the stream function. Navier-Stokes equations are the basis for the fluid flow in the fluid-structure interaction finite element model that will be introduced in Chapter 4. The stream function is suggested by AASHTO (2008) to solve the fluid domain and calculate the forces on substructure. Additionally, more details on the existing wave load models for coastal bridges are presented in this chapter. Finally, appropriate modifications to these wave load models based on experimental test

data are proposed. In order to increase the accuracy of the wave load models, bias removal functions are developed for the existing wave load models. These modified wave load models are the basis for the response analysis that will be conducted as a part of reliability assessment of coastal bridges.

3.1. Solution of the Fluid Domain

3.1.1. Navier-Stokes Equations

The fluid domain should be first solved in order to calculate the forces on bridge structures. The most general equations for fluid flow are Navier-Stokes equations (Currie 1974). These equations stem from applying the Newton's second law along with the conservation of mass, momentum and energy to a control volume of fluid. Navier-Stokes equations are of interest in mathematics. The existence and smoothness of the solution has not been proven for the three dimensional (3D) case. Clay Mathematics Institute (2012) has called this as one of the seven most important open problems in mathematics, and has offered a prize of $1,000,000 for its solution.

The general form of equation of motion can be written as:

$$\rho \frac{D\mathbf{u}}{Dt} = \nabla.\sigma + \mathbf{f} \tag{3-1}$$

The operator on the left hand side of Equation (3-1) is defined in Equation (3-2):

$$\frac{D}{Dt}(\bullet) = \frac{\partial}{\partial t}(\bullet) + \mathbf{u}.\nabla(\bullet) \tag{3-2}$$

where ρ is the fluid density, $\mathbf{u}$ is the velocity vector, σ is the stress tensor, $\mathbf{f}$ is the body force vector, $\frac{\partial}{\partial t}(\bullet)$ is the partial derivative with respect to time, and ∇ is the gradient operator. This general equation of motion, along with the conservation laws should be solved for a given fluid to obtain the velocity and pressure fields. In engineering applications, water is considered as an incompressible fluid, which reduces the computational burden. Nonetheless, the solution for above equation is highly demanding, especially in the case of a turbulent flow. It is generally believed that the Navier-Stokes equations describe turbulence properly (Rosa 2006). The numerical solution of the Navier-Stokes equations for turbulent flow becomes infeasible due to the extremely fine mesh that is required for stability. To overcome this problem, time averaged equations, such

as Reynolds-averaged Navier-Stokes (RANS) equations are used in computational fluid mechanics (Rosa 2006).

3.1.2. Stream Function

The stream function is used to solve the fluid flow in a two-dimensional (2D) plane. The difference between the stream function at any two arbitrary locations values provides the volumetric flux between the two points. The stream function is defined such that its curl provides the fluid velocity:

$$\mathbf{u} = \nabla \times \psi \tag{3-3}$$

where ψ is the stream function. Similar to the velocity potential, the stream function should also satisfy the Laplace equation. For a moving wave, extra boundary conditions are imposed on the stream function. These equations are zero vertical velocity at the bottom, kinematic free surface boundary condition, presented in Equation (2-1), and dynamic free surface boundary condition (Dean 1965):

$$\frac{p\left(x\right)}{\rho g} + \frac{1}{2g}\left(u_1^2 + u_2^2\right) + \eta - \frac{1}{g}\psi_t = 0; \quad z = \eta \tag{3-4}$$

where $p(x)$ is wind pressure on the surface, x and z denotes horizontal and vertical axes respectively, g is the gravitational acceleration, and η is the free water surface elevation. The dynamic free surface boundary condition is the unsteady form of the Bernoulli equation. The objective is to find the stream function that satisfies the Laplace equation and all the imposed boundary conditions. Dean (1965) provided an approximate solution to these equations in the form of a harmonic series. The series can be expanded to as many terms as required to provide the desired level of accuracy. The stream function solution to the Laplace equation provides a more accurate velocity field, especially for large wave heights in comparison to the linear wave theory.

3.2. Simplified Methods for Estimation of Wave Forces

3.2.1. Morison Equation

One of the well known simplified methods for approximation of fluid forces on structures is the Morison equation (1950). The equation is comprised of a drag term and an inertial term that provide the hydrodynamic force, F, parallel to the flow direction (Morison et al. 1950):

$$F = F_D + F_I = \frac{1}{2}\rho C_d A u_y \left|u_y\right| + \rho C_m V \dot{u}_y \tag{3-5}$$

where C_d is the drag coefficient, A is the cross sectional area of the body perpendicular to the flow direction, u_y is the water velocity in y direction, C_m is the inertia coefficient, V is the volume of the body and $\dot{u}_y$ is the water acceleration. It should be noted that the Morison equation is for uni-directional fluid flow. Additionally, the Morison equation is valid when the structural members' dimension is small in comparison to the wave length; therefore, there is no diffraction effect. AASHTO (2008) recommends calculating the forces on the bridge piers by using this equation.

3.2.2. AASHTO Specifications for Wave Loads on Bridge Decks

3.2.2.1. AASHTO Peak Wave Forces

The AASHTO (2008) equations for peak wave forces were derived from the extensive studies of Marin and Sheppard (2009). Their wave load model has been developed based on a physics-based model, that was established upon the results of the experimental test data (Sheppard and Marin 2009), and has been determined to be accurate in practice (Marin and Sheppard 2009).

The vertical force on the bridge deck is composed of drag, inertial and buoyant forces, which comprise the quasi-static component of the force, in addition to the impact force due to the trapped air. The maximum quasi-static vertical force per unit length is calculated by (AASHTO 2008):

$$F_{V-\max} = \gamma_w \overline{W} \beta_A \left(-1.3 \frac{H_{\max}}{d_s} + 1.8 \right) \left[1.35 + 0.35 \tanh(1.2T_p - 8.5) \right] \times \left(\begin{array}{c} b_0 + b_1 x_A + \frac{b_2}{ya} + b_3 x_A^2 \\ + \frac{b_4}{y_A} + \frac{b_5 x_A}{y_A} + b_6 x_A^3 \end{array} \right) (TAF) \tag{3-6}$$

where γ_w is the unit weight of water, $H_{\max}$ is the wave height, d_s is the total water depth during the storm surge, and T_p is the wave period. Coefficients b_0 to b_6 are defined by the geometric properties of the deck, and TAF is a factor to adjust the vertical quasi static force for the amounts of entrapped air. $\overline{W}$ and β_A are defined as (AASHTO 2008):

$$\overline{W} = \left[\lambda - \frac{\lambda}{H_{\max}} \left(Z_c + \frac{H_{\max}}{2} \right) \right]; \text{ if } \frac{\overline{W}}{W} < 0.15, \text{ then } \overline{W} = 0.15W \tag{3-7}$$

$$\begin{aligned} \beta_A &= 0; \text{ if } \eta_{\max} - Z_c \le 0 \\ \beta_A &= \frac{\eta_{\max} - Z_c}{d_b}; \text{ if } 0 < \eta_{\max} - Z_c \le d_b \\ \beta_A &= 1; \text{ if } \eta_{\max} - Z_c > d_b \end{aligned} \tag{3-8}$$

and x_A and y_A are defined as (AASHTO 2008):

$$\begin{aligned} x_A &= \frac{H_{\max}}{\lambda} \\ y_A &= \frac{\overline{W}}{\lambda} \end{aligned} \tag{3-9}$$

The associated impulse-type force, designated as slamming force, per unit length is shown in the following equation (AASHTO 2008):

$$F_s = A_A \gamma_w H_{\max}^2 \left(\frac{H_{\max}}{\lambda} \right)^{B_A} \tag{3-10}$$

A_A and B_A take into account the surge and wave crest position with respect to the deck. Coefficient A_A asymptotically approaches zero rapidly as the water elevation exceeds the deck elevation, leading to nearly zero slamming force when the deck is submerged.

The maximum horizontal wave load is defined as (AASHTO 2008):

$$\begin{aligned} F_{H-\max} = \gamma_w \pi \left(d_b + r \right) \left(\omega_A + \frac{H_{\max}}{2} \right) \left(\frac{H_{\max}}{\lambda} \right) \\ \exp\left[-3.18 + 3.76 \exp\left(-\frac{\omega_A}{\lambda} \right) - 0.95 \left[\ln\left(\frac{\eta_{\max} - Z_c}{d_b + r} \right) \right]^2 \right] \end{aligned} \tag{3-11}$$

where

$$\omega_A = \lambda - \frac{1}{2}\left(Z_c + \frac{H_{\max}}{2}\right)\left(\frac{\lambda}{H_{\max}}\right);$$
$$\text{if } \lambda - \frac{1}{2}\left(Z_c + \frac{H_{\max}}{2}\right)\left(\frac{\lambda}{H_{\max}}\right) \geq W, \text{ then } \omega_A = W \tag{3-12}$$

This research proposes to remove the bias from these equations prior to implementation in any bridge reliability framework based upon comparison with existing experimental test data as discussed in the next section.

3.2.2.2. Bias Removal

It is vital to have an unbiased equation for estimation of wave forces for reliability assessment. Thus, in this part of the research, the AASHTO equations are compared with available experimental test data in the literature in order to remove any possible bias, as well as quantify uncertainty about the predictive models.

Experimental test data are extracted from Bradner (2008) and Sheppard and Marin's (2009) report to Florida Department of Transportation. A total number of 550 points were extracted from these references. These experimental test data are shown in Appendix I. The result of the AASHTO equations versus experimental test data is shown in Figure 3-1. This figure shows the comparison of forces per unit volume in terms of the relative surge elevation, Z_c. The results suggest that

the AASHTO equations are conservative for negative values of Z_c, corresponds to the submerged deck. Thus, a bias removal function is introduced in order to match the mean value of analytical equations with experiment. Different regression models have been tested to develop a reasonable bias removal function. Stepwise regression has been conducted to identify the significant parameters in the regression model. The final regressed bias removal function, named as Δ_b, is a degree two polynomial, which is shown in Equation (3-13). The R^2 value of the regressed equation is 0.89.

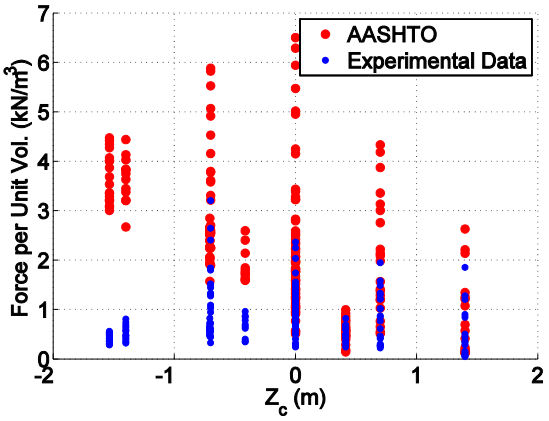

Figure 3-1. Comparison of AASHTO equation and experimental test data.

$$\frac{\Delta_b}{W^2} = 0.347 - 1.316Z_c - 0.126H - 0.102T_p + 0.200Z_cH - 0.071Z_cT_p + 0.114HT_p \tag{3-13}$$

Δ_b has the dimension of force per unit length. Figure 3-2 plots the calculated error and the regressed surface (in three dimensions, T_p is not shown), which indicates a good regression model. Figure 3-3 depicts the results after adding the bias removal equation to the AASHTO equations.

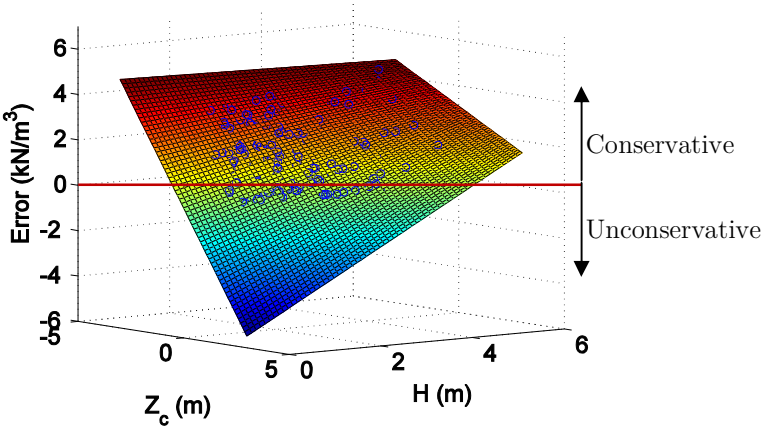

Figure 3-2. Error in the AASHTO equation versus the regressed bias removal function.

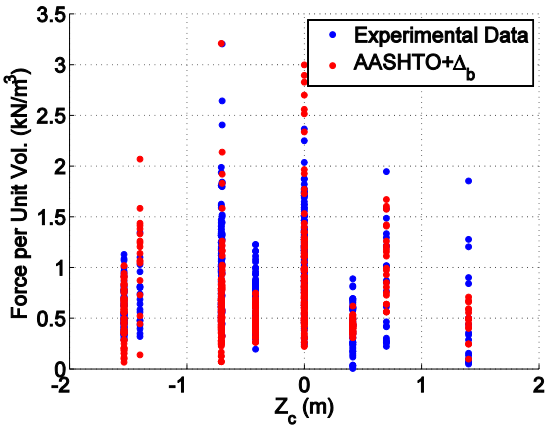

Figure 3-3. Comparison of AASHTO equation and experimental test data after adding the bias removal term.

Jin and Meng (2011) also pointed out that the AASHTO equations are conservative for submerged deck. Based on the results of their finite element simulations, they suggested a new set of equations for calculation of wave forces. The suggested equations are compared against the AASHTO (2008) plus bias removal in Figure 3-4. As shown in this figure, the mean value of error for the Jin and Meng formula is more than zero suggesting a systemic over estimation of wave loads. Therefore the new formula suggested by Jin and Meng (2011) is still conservative. Thus in this research, AASHTO (2008) equations plus bias removal function will be adopted as a simplified model to define the maximum forces on bridge decks under wave loads. It should be noted that the bias removal is developed based on the experimental test data; however, the experiments might be biased with respect to the real world.

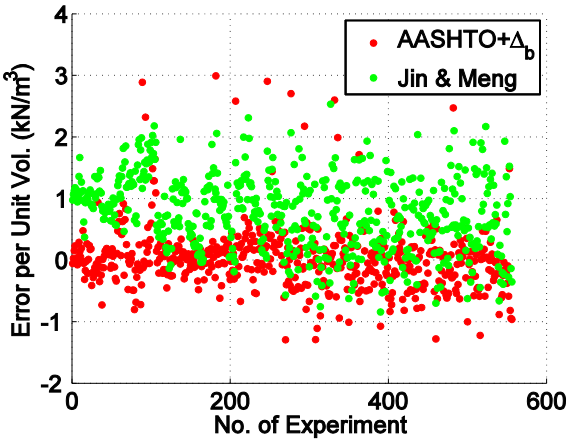

Figure 3-4. Comparison of AASHTO plus bias removal and Jin and Meng (2011) proposed formula.

Since the objective of this study is to provide the probabilistic framework for reliability assessment of coastal bridges under hurricane events, a model error term associated with the wave force equation is also developed. The distribution of the model error, ε_1, was found by using the entire experimental data set versus their corresponding theoretical value. Implementing the Kolmogorov-Smirnov test, the model error term was found to be best described by a lognormal distribution with parameters of 0 and 0.08^2 [ln (0,0.08^2)] respectively. The final probabilistic equation for estimation of the vertical component of wave forces, F_{Vt}, is presented in Equation (3-14).

$$F_{Vt} = \left(F_{V-\max} + F_s + \Delta_b\right)\varepsilon_1 \tag{3-14}$$

The horizontal component of wave forces is not biased; and therefore, no bias removal function is developed for horizontal loads.

3.2.2.3. Time History of Wave and Surge Loads for Dynamic Simulations

The time history of the wave load is required for nonlinear time history analysis of bridges. A phenomenological model is first developed for response assessment. A model for deriving a time history of the wave forces on bridge decks has not been

analyzed in great detail to date in the literature, but it has been found that the wave forces are in phase with the wave (Sheppard and Marin 2009). The method that is employed in this research to demonstrate the time history of wave forces on the bridge deck is derived from the work of Sawyer (2008) and Sheppard and Marin (2009). Sawyer demonstrates the forces caused by a wave at three different positions on the bridge deck. These positions cause a different combination of vertical forces, horizontal forces, and moments. Figure 3-5 shows one of the configurations of wave passage, and the qualitative position of forces.

As the wave passes by the bridge deck, both the magnitude and direction of the forces change with time. As the wave comes in contact with the girders of the bridge, the water traps pockets of air in between the wave and the bottom of the bridge deck. This trapped air pocket causes a sudden force taken here to be the slamming force (AASHTO 2008). This phenomenon results in a series of impact forces equal to the number of girders on the bridge (Sheppard and Marin 2009). The negative portion of the force is caused by the suction force that arises from the wave pulling down on the air pocket and the force from the water mass on top of the bridge deck. This force can be equal in magnitude to the positive quasi-static force. This occurrence of negative suction forces also occurs in the horizontal

direction, causing negative forces equal in magnitude to the positive horizontal forces. This force can be equal in magnitude to the positive quasi-static force (Cuomo et al. 2009).

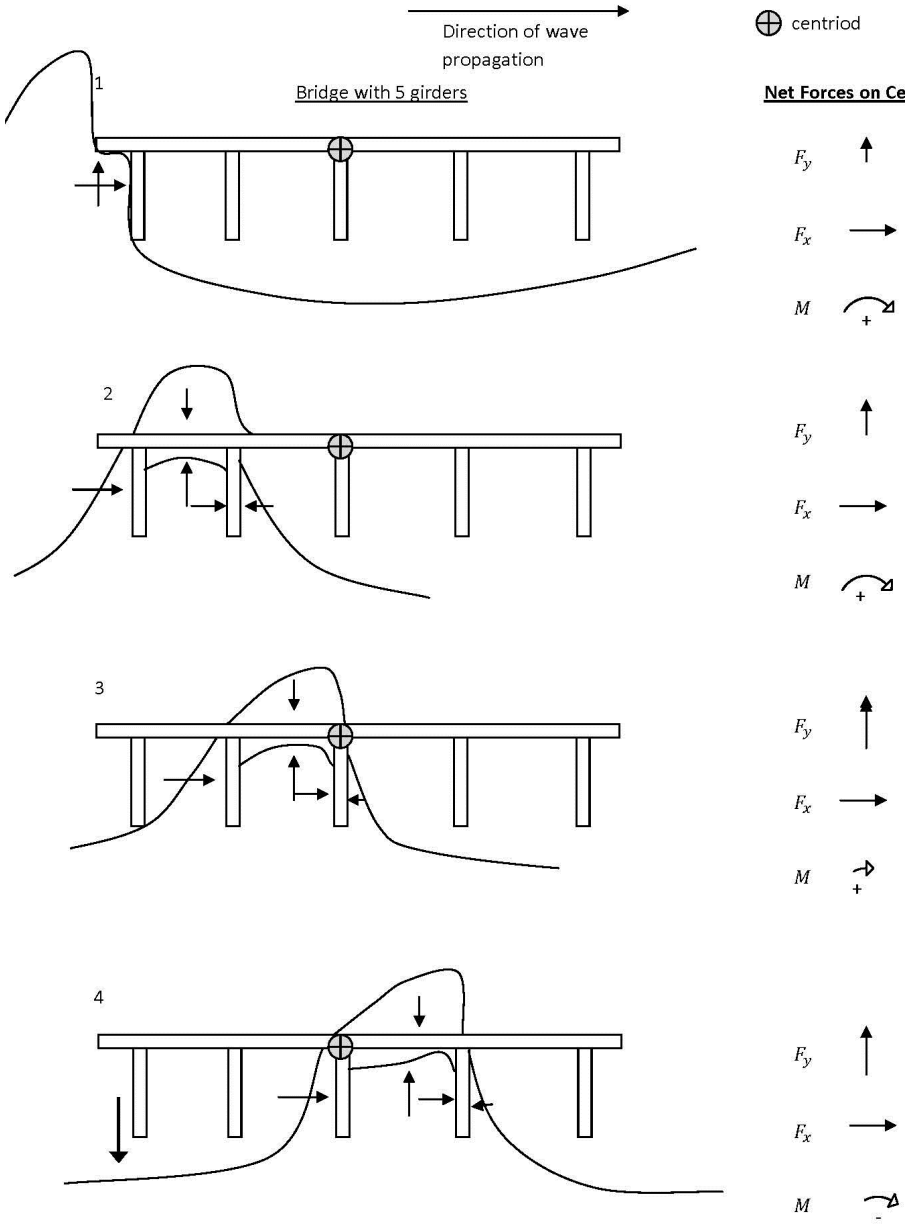

Figure 3-5. A wave passing by a bridge deck with five girders (Sawyer 2008).

The wave forces in this research have been taken as a sinusoid with a period equal to that of the wave and maximum amplitude equal to that of the maximum quasi-static load. The impact loads are then superimposed on the quasi-static forces. The impact loads were observed to have an effect on the bridge for approximately 5/8 the period of the wave, based on visual observation of results given by Sheppard and Marin (2009). Similar model is used for the horizontal wave component to distribute the maximum horizontal load over the wave period. Figure 3-6 depicts a sample of wave loads on a bridge deck with eight girders.

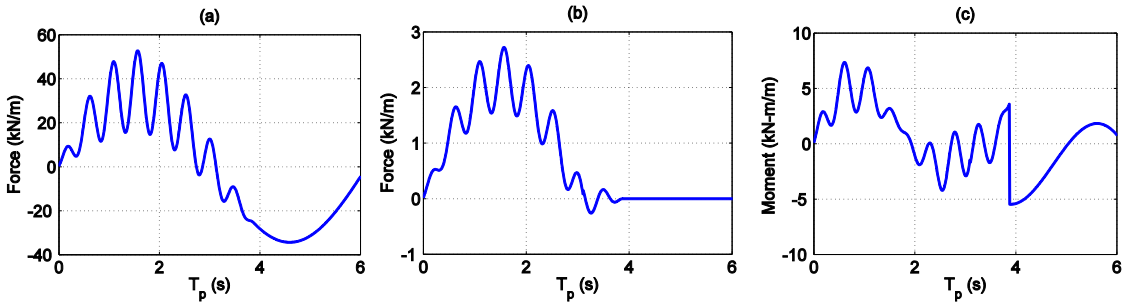

Figure 3-6. Wave load on a bridge deck with eight girders from phenomenological model: (a) vertical wave loads; (b) horizontal wave loads; and (c) moment per unit length of the span.

In addition to the vertical and horizontal forces, moment induced by wave should also be considered about the bridge deck centerline. When a wave passes over a bridge deck, the forces imparted change dramatically with time, and those forces cause moments on the bridge deck. The moment is calculated about the

center of the bridge deck at each time step using the moment arm method. The time-varying moment arm follows a linear time history, as it is assumed that the wave is moving at a constant velocity (Ataei et al. 2010).

The total vertical force for time history analysis of simply supported spans is limited to the deck uplift capacity. The reason behind this upper bound is that the vertical force does not increase after the deck has been uplifted. More details on this upper bound limit for vertical wave forces are provided in the next chapter.

3.2.3. Modified Douglass Equations for Wave Loads on Bridge Decks

3.2.3.1. Douglass Equations for Peak Wave Forces

The Douglass equations for peak vertical and lateral loads on the bridge deck are presented in Equations (3-15) and (3-16) respectively (Douglass et al. 2006).

$$F_{V-\max} = c_{v-va}\gamma_w\left(\eta_{\max} - Z_c - d_g\right)W \tag{3-15}$$

$$F_{H-\max} = \left[1 + c_r\left(N_g - 1\right)\right]c_{h-va}\gamma_w\left(\eta_{\max} - Z_c - \left(d_b + r\right)/2\right)\left(d_b + r\right) \tag{3-16}$$

where $c_{v\text{-}va}$ and $c_{h\text{-}va}$ are the empirical coefficients (recommended to set equal to 1), c_r is the reduction factor for internal girders (recommended value of 0.4), d_g is the girder height, and N_g is the number of girders.

3.2.3.2. Bias Removal

The same procedure and same experimental data set that has been employed earlier to develop the bias removal function for AASHTO (Section 3.2.2.2) are utilized to develop the bias removal function for the Douglass equations. Stepwise regression is employed to systematically find the influential wave and surge parameters in the bias removal function. Different regression models are examined. The best form of the bias removal function is found to be:

$$\begin{aligned} \frac{\Delta_{bV}}{W^2} &= -0.462 - 0.932Z_c + 0.3393H - 0.045Z_cH + 0.761Z_c^2 - 0.024H^2 \\ \frac{\Delta_{bH}}{W^2} &= -0.161 - 0.125Z_c + 0.151H - 0.011Z_cH + 0.152Z_c^2 - 0.010H^2 \end{aligned} \tag{3-17}$$

where Δ_{bV} is the bias removal for vertical force component; and Δ_{bH} is the bias removal for horizontal force component. The R^2 goodness-of-fit test values for vertical and horizontal force bias removals are 0.91 and 0.79 respectively. The peak forces from Douglass (2006) equations are divided by these two functions:

$$\begin{aligned} F_j &= \frac{F_{j-\max}}{\Delta_{bj}} \\ j &= H,V \end{aligned} \tag{3-18}$$

The estimated forces from Modified Douglass equations are in good agreement with the experimental test data. However, in this research, the Modified AASHTO wave load model is adopted for the reliability assessment off coastal bridges, since AASHTO (2008) code is commonly adopted in practice.

3.3. Summary

This chapter presented the relevant methods to calculate wave and surge loads on bridges. The most comprehensive method to estimate the wave forces is by solving the fluid domain via Navier-Stokes equations and applying the pressure filed on the structure (fluid-structure interaction). This methodology needs significant computational power and discretization of the domain through finite element or finite volume methods. Additionally, fluid-structure interaction model is not easy to build. As a result, simpler numerical model that is reduced to only a single physics domain, i.e., solids, is preferred for reliability assessment studies. Such a simplified model for coastal bridges is developed by numerically modeling the bridge structure and applying wave load models to the bridge deck that provide the same profile as the FSI wave loads. Therefore, this chapter provided the two main wave load models, AASHTO (2008) and Douglass et al. (2006), that are

available in the literature for the estimation of wave loads on coastal bridges. Additionally, methodologies for distribution of maximum wave loads over the wave period are developed and introduced in this chapter. Comparison of the proposed wave load models with the experimental test data reveals conservatism especially for the submerged deck. It is vital to remove this bias from the wave load models before adopting them for the reliability study. Therefore, bias removal functions for both wave load models are tested and presented. The Modified AASHTO wave load model that is introduced in this chapter will be used in the rest of this research for estimation of demand on coastal bridges.

Chapter 4

Finite Element Models of Coastal Bridges

This chapter introduces the numerical models that are developed to study the performance of the coastal bridges subjected to hurricane induced wave and surge loads. The developed models are vital for the rest of this research since the probabilistic studies are conducted on the outcomes of these finite element models. This chapter introduces two main models: 1) the solid domain model only that is used in conjunction with the Modified AASHTO load equations; and 2) the fluid-structure interaction model that involves both solid and fluid domain.

4.1. OpenSees Finite Element Model of Coastal Bridge

A bridge model is developed in the OpenSees software package (OpenSees 2012), which is an open source finite element package that requires computer coding for generation of the finite element model. This platform provides the freedom to automate the process for probabilistic studies by generating different input text files that follow the same structure but have different random variables. The main properties of the developed OpenSees models are presented in this section.

4.1.1. General Description

The bridge is modeled as centerline spline, as shown in Figure 4-1. The lines represent the beam-column elements and the spheres represent the nodes. Each node has an assigned mass based on the bridge properties and its tributary area.

The transverse deck elements are modeled with a high stiffness elastic material and are considered as rigid elements. The deck centerline is modeled as an elastic material, since no nonlinearity is expected in the bridge superstructure. The deck's stiffness is calculated based on the deck geometry and material properties.

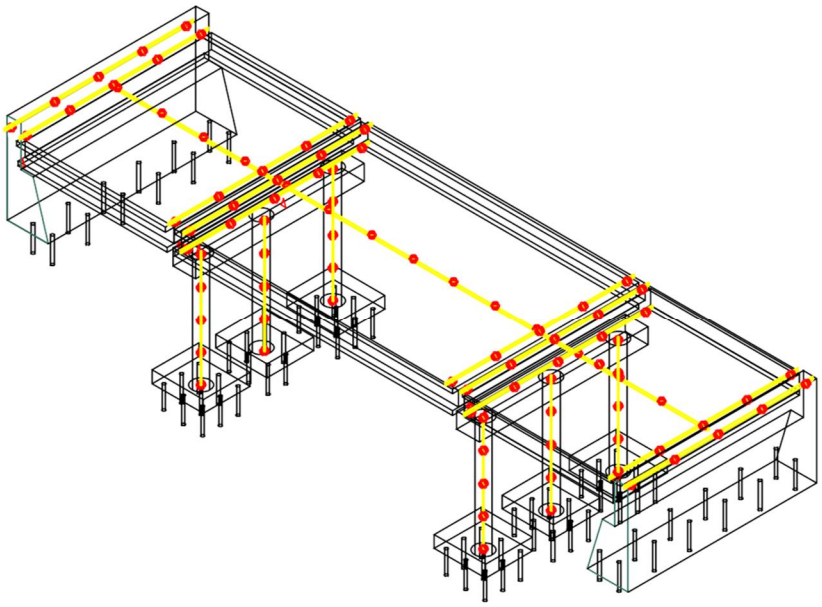

Figure 4-1. Spline bridge model.

4.1.2. Foundations

The soil behind the abutment is considered to be a compression only element (passive action only) and is represented by nonlinear zero-length elements, as recommended by Nielson (2005). The properties of the pile systems, for column foundations and also abutments, are estimated based on the API (2007) recommendations. The pile compression strength, Q_d, comprises of the end bearing capacity and skin friction, as shown in Equation (4-1), while skin friction and weight of the pile and soil plug comprise the uplift capacity.

$$Q_d = Q_f + Q_p = f_s A_{si} + qA_p \tag{4-1}$$

where Q_f is the skin friction and Q_p is the end bearing capacity. f_s is the unit skin friction capacity, A_{si} is the side surface area of the pile, q is the unit end bearing capacity and A_p is the end area of the pile. For cohesive soils, f_s is related to the undrained cohesion strength of the soil, c (API 2007):

$$f_s = \alpha c$$
$$\alpha = \begin{cases} 0.5\psi^{-0.5}, & \psi \le 1 \\ 0.5\psi^{-0.25}, & \psi > 1 \end{cases}; \quad \alpha \le 1 \tag{4-2}$$

where ψ determines the ratio of the cohesion to the effective overburden pressure, and in this study is assumed to be equal to 1. q is taken equal to $9c$ according API (2007). The pile stiffness is calculated based on the API (2007) t-z curves. The maximum capacity, Q_d, mobilizes at $0.01\,d_p$ pile movement. These properties are assigned to a nonlinear zero-length element at pile locations. Figure 4-2 shows the force-deformation for a 0.4m diameter pile with 10m length located in a cohesive soil with c equal to 30kPa.

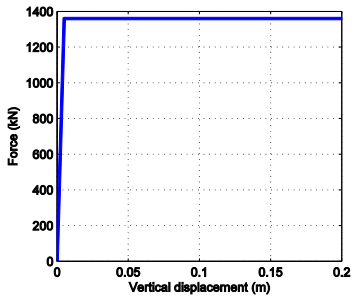

Figure 4-2. Pile force-deformation in vertical direction.

4.1.3. Nonlinear Beam-Column Elements

The columns and bent beams are modeled as nonlinear beam-column elements. These elements include a fiber section, which integrates the mechanical properties of concrete and reinforcing steel in flexure and axial modes. Figure 4-3 depicts a sample fiber section for a concrete column.

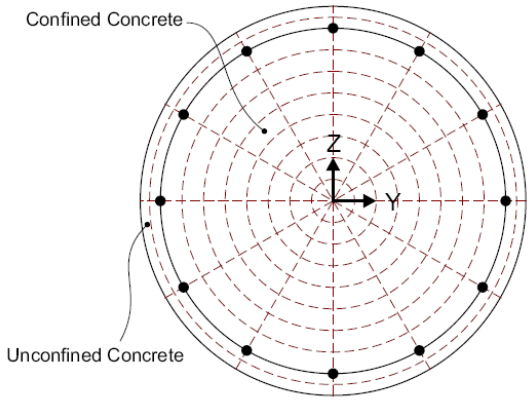

Figure 4-3. Sample fiber section for a reinforced concrete column with twelve longitudinal reinforcing rebars (OpenSees 2012).

Different properties are assigned to the confined and cover (unconfined) concrete. The compression strength of concrete from as built plans is assigned as the cover concrete median strength. Randomness associated with the mechanical properties and other parameters are defined in the next chapter. The properties of confined concrete are estimated based on Mander et al. (1988) equations. These equations take into account the distance in between the transverse reinforcements

as well as the longitudinal reinforcements. Figure 4-4 schematically shows the difference in mechanical properties of confined and unconfined concrete. The ultimate strength and crushing strain of the confined concrete is higher in comparison to the unconfined concrete. To model all of these properties, the Concrete06 (OpenSees 2012) is used in this research. This concrete material model provides nonlinear softening in compression and tension.

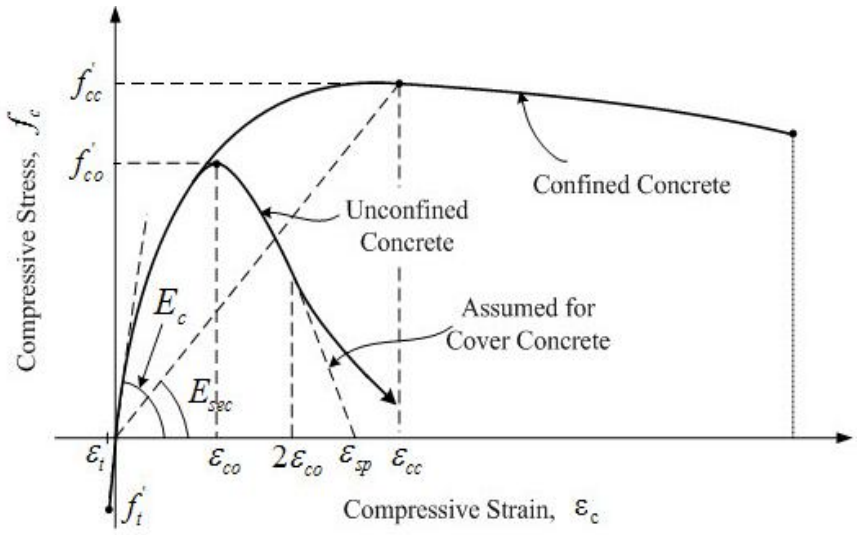

Figure 4-4. Differences in mechanical properties of confined and unconfined concrete. Adapted from Priestley et al. (1996).

The reinforcement rebars are modeled by using Reinforcing Steel material model (Mohle and Kunnath 2006). This material model is able to capture the reduction in strength and stiffness due to cyclic load and fatigue. Additionally, this material model is capable of capturing the buckling of the reinforcement, which

essentially leads to collapse. Figure 4-5 plots the response of a 0.9m circular concrete column with twelve 28mm longitudinal reinforcing steel. This is a common column for many bridges in the Houston/Galveston Bay area. This figure shows the pushover as well as cyclic loading response of the column. The hysteretic response is slightly lower than the pushover curve. This is due to the strength reduction of the reinforcing steel under the cyclic loading. This phenomenon is not captured by other nonlinear material models for reinforcements.

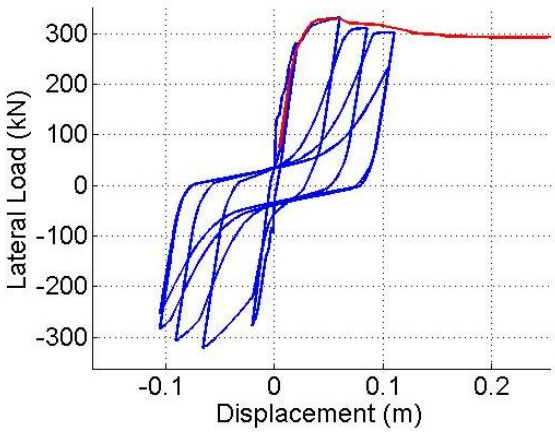

Figure 4-5. Hysteretic response of a circular column with reinforcing steel material.

4.1.4. Contact and Impact Elements

As mentioned in the introduction, bridge deck unseating is one of the predominant failure modes of coastal bridges under wave and surge loads. Deck uplift is a complicated phenomenon that is hard to capture in the finite element models

owing to the local instability of the bridge deck model. After the deck uplift, the bridge deck undergoes the rigid body motion. Consequently, the global stiffness matrix is not stable anymore. To accommodate for the deck uplift in the finite element model, contact elements are introduced between the bridge superstructure and its supports. The contact elements essentially provide an interface between the two parts of structural model, and permit the motion of one part with respect to the other in dynamic simulations. The OpenSees contact model is a node to node contact interface. Contact elements are a special type of zero-length elements that does not have tensile capacity. Also, the tangential strength of the contact elements is a function of the normal force, simply based on the friction law:

$$\begin{aligned} F_f &= \mu_j F_n \\ j &= s, d \end{aligned} \tag{4-3}$$

where F_f is the friction force, F_n is the normal force, s is the index for static, d is the index for dynamic, and μ_s and μ_d are the static and dynamic coefficients of friction, respectively. Since there is no change in the response by considering the static coefficient of friction, only the dynamic coefficient of friction is employed in this study; and for simplicity, is referred to as the coefficient of friction. It should be noted that for the stability of the numerical simulation, the gravity loads,

corresponding to the deck weight, should be applied to the bridge superstructure before performing the time history analysis. Otherwise, the bridge deck is unstable from the beginning of the simulation due to the lack of normal forces on contact elements. Another consideration is the direction of the contact elements. The direction of the contact element is from the top (slave) node to the bottom (support or master) node in order to provide the correct normal vector.

Contact elements only have three degrees of freedom (translational) at each node. However, the rest of the structure has six degrees of freedom at each node. Therefore, it is not possible to directly connect a contact node to any other structural node due to the inconsistency in degrees of freedom. To overcome this compatibility problem, two dummy nodes, one at each side of the contact element, should be introduced. These dummy nodes are restrained in all translational degrees of freedom to the contact nodes. Other elements will be connected to these dummy nodes instead of the contact nodes.

The contact algorithm in OpenSees is based on the penalty algorithm (Wriggers 2008). This means that the two end nodes of the contact can penetrate each other by a limited distance. The amount of penetration is limited by a Lagrange penalty factor that can be seen as the stiffness of the contact.

Theoretically, the normal stiffness should be infinity to prevent the nodal penetrations. However, for numerical purposes, it is not possible to use infinite stiffness. Determination of the normal and tangential stiffness for contact elements is by trial and error, and varies from one problem to the other. If the normal stiffness of the contact is significantly higher than the elements that are connected to it, which is true for the developed bridge model, the error from the nodal penetration is negligible. Based on the simulations for this research, the recommended range for normal stiffness for typical highway bridges superstructure, is in the range of 10^6kN/m to 10^7kN/m. The recommended range for tangential stiffness is one order of magnitude less than the normal stiffness.

For simply supported span bridges, impact elements are used in between the bridge decks to incorporate for pounding. However, given that the incident angle of the wave is perpendicular with respect to the bridge centerline, the response of the bridge is in the transverse direction. Therefore, the impact elements do not engage during the wave passage. Similar impact elements are utilized underneath the contact elements. The properties of these impact elements are calculated based on recommendations by DesRoches and Muthukumar (2002).

The load models for the OpenSees model has been introduced and validated in Chapter 3. However, there is no experimental test data on the bridge behavior under hurricane-induced wave and surge loads. Nevertheless, the developed structural model is established on the basis of the previous works such as Nielson (2005) and Padgett (2007), that has been validated based on experimental test data.

4.2. ADINA FSI Finite Element Model

This section describes the modeling strategy for developing FSI models of water crossing bridges under wave and surge action, which is implemented in this study using the ADINA (2012) finite element software package. The modeling strategy is validated by comparing with existing experimental test data in the literature. The main focus of the modeling is to develop an appropriate finite element model with fluid-structure interaction (FSI). This multi-physics model can provide more accurate results than the model with the structure exclusively, since it captures the interaction between fluid and solid domains; thus although it is more computationally expensive, it provides more insight on the performance of coastal

bridges under wave and surge action. The details of the developed model are presented in this section.

4.2.1. Fluid Domain

The fluid domain is simulated using the finite element method. The governing equations of fluid flow are Navier-Stokes equations, which can be interpreted as conservation of mass, momentum and energy over a control volume of fluid, as represented in Chapter 3. For modeling the turbulent flow, Reynolds-averaged Navier-Stokes equations in conjunction with the $k-\varepsilon$ turbulence flow model are employed in an arbitrary Lagrangian-Eulerian coordinate system. In order to avoid the need for re-meshing of the fluid domain, which increases the simulation time significantly, the volume of fluid (VOF) method is used to capture the interface of the free water surface. The VOF method was proposed by Hirt and Nichols (1981) to model the free boundaries in finite difference numerical simulations. However, the concept is general and has been adopted in finite element and finite volume models afterwards. In the volume of fluid method, the fraction of each fluid in any cell is calculated at each time step. This fraction introduces an extra unknown to the system of equations. The interface between the two fluids is tracked by solving

a continuity equation over the domain, which provides the extra equation in the system.

The analysis starts from the at rest situation, where the fluid particles are stationary in space. For the initial condition, the values of k, kinetic energy, and ε, rate of dissipation, are calculated based on the average velocity of the water and an initial approximation of turbulence intensity as shown below (ADINA 2010):

$$\begin{aligned} k &= 1.5(Iu)^2 \\ \varepsilon &= \frac{k^{1.5}}{0.3L_H} \end{aligned} \tag{4-4}$$

where I is the turbulence intensity, u is the average velocity at the wavemaker boundary and L_H is the hydraulic diameter of the channel. A moving wall boundary condition is adopted in the inlet as a piston wavemaker. The wavemaker motion typically follows a sinusoid (Dean and Dalrymple 1984). In this study, in order to reduce the effect of secondary waves in the model, the wavemaker motion is prescribed by (Huang and Dong 2001):

$$\begin{aligned} d_w &= d_{w0}\left[\cos\omega t + \frac{H}{4d_s n_1}\left(\frac{3}{4\sinh^2 md_s} - \frac{n_1}{2}\right)\sin 2\omega t\right] \\ d_{w0} &= \frac{Hn_1}{2\tanh md_s},\ n_1 = 0.5\left(1 + \frac{2md_s}{\sinh 2md_s}\right) \end{aligned} \tag{4-5}$$

where H is the wave height, d_s is the water depth during the storm, m is the wave number, ω is the angular frequency of the wave and t is time. This formulation takes into account the Stokes second order waves. Higher order Stokes or the Stream function can be used to approximate the water surface and corresponding boundary motion. However, Equation (4-5) provides acceptable wave profiles (i.e., without secondary waves that contaminate the original wave) in the developed numerical model, and also has been adopted in previous studies (Huang and Dong 2001). Therefore, Equation (4-5) is adopted in this study.

4.2.2. Structural Domain

The structure is modeled using solid elements with nonlinear material for concrete and steel. Mechanical properties of confined and unconfined concrete are calculated based on Mander et al (1988) as presented in Section 4.1.3. A bilinear stress-strain relationship is used as the constitutive law for the steel material. Contact surfaces are introduced between the bridge deck and its support. The contact algorithm in ADINA provides surface to surface contact interface, and automatically detect the correct normal vector. It is significantly more stable than the OpenSees node to node contact algorithm. Other structural properties such as pile properties are the same as the OpenSees model.

4.2.3. Fluid-Structure Interaction

In the fluid-structure interaction models, forces from the fluid deform the structure and the structural deformation changes the fluid domain. Therefore, the solution at each time step is iterative to achieve the balance in the fluid domain and structural displacement. The fluid-structure interaction problem is always nonlinear, due to the nonlinearity of Navier-Stokes equations. Direct coupling is used for the interaction problem, which means the fluid and structure equations are combined into one system and solved together.

4.2.4. Validation of the FSI Model

The developed model is validated by comparing the numerical results against experimental test data available in the literature. Three experimental datasets are used in this study for comparison with the numerical simulation. The first set of data is obtained from Sheppard and Marin's (2009) report to the Florida Department of Transportation. The experimental tests were conducted at 1:8 scale on flat slab and concrete girder spans. The second experiment was performed at Oregon State University (Bradner 2008) at 1:5 scale. The last experimental test data is obtained from the tests that were conducted at Texas A&M University at a

scale of 1:20 (McPherson 2008). The tested specimens in the last two experiments were girder spans. In the aforementioned references, emphasis is placed on the estimation of peak values of the vertical and horizontal forces. Only McPherson (2008) provides force time histories for some of the experimental tests. Figure 4-6 shows the water profile and pressure field and also the effective stresses on structural elements for one of the numerically simulated tests from McPherson's (2008) experiments. The wave loads induce positive moment in the span, which causes a maximum tensile and compressive stress of about 0.6MPa. Figure 4-7 depicts a comparison of the time series of the vertical wave loads on the deck from the experiment and numerical model. The span is supported by six girders, and has the total width of 0.68m. Each girder has the dimension of 70mm by 38mm. The slab thickness is 10mm. The rail height is 50mm. This model is representing the US 90 Bridge over Biloxi Bay. The water depth for this test is 0.39m and wave height is 0.14m. The peak value of the force is almost the same for both the experiment and numerical models and is equal to 523N. The maximum error is for the negative portion of the force time history, and is approximately equal to 74N (i.e. the test result is approximately 115N, where the numerical model output is 189N). However, the error is reasonably small for the rest of the time history. The mean

absolute percentage error for the entire time series is 15.6%. The negative portion of the force is caused by the suction of the air pocket that is trapped between girders and also the weight of the water on top of the bridge deck. By observing the experimental tests performed by Sheppard and Marin (2009), larger magnitude of the negative portion of force is expected during the wave passage. Sheppard and Marin's (2009) test results suggest larger negative wave forces magnitudes that can be even equal to the peak positive magnitude of the load.

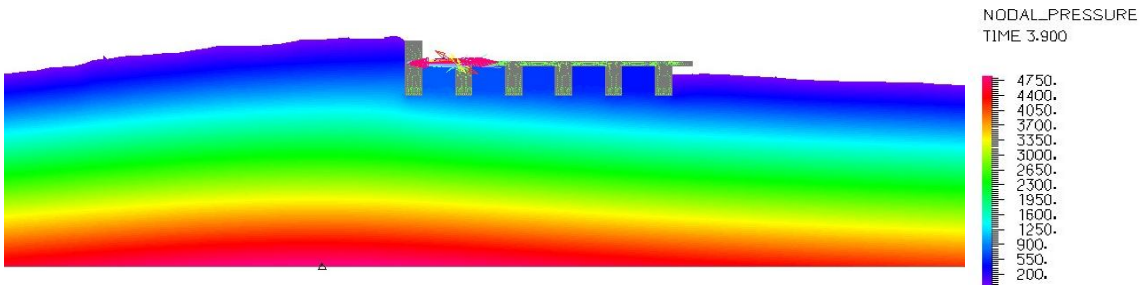

Figure 4-6. Pressure contours and effective stress vectors for the wave height of 0.14m and water depth of 0.4m experiments from McPherson (2008). (Pressure units: Pa).

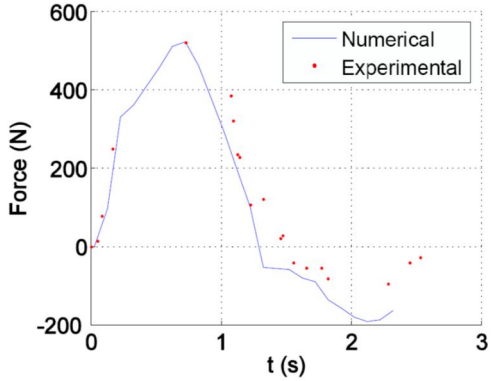

Figure 4-7. Comparison of numerical and experimental wave load time history on bridge deck for the wave height of 0.14m and water depth of 0.4m experimental test by McPherson (2008).

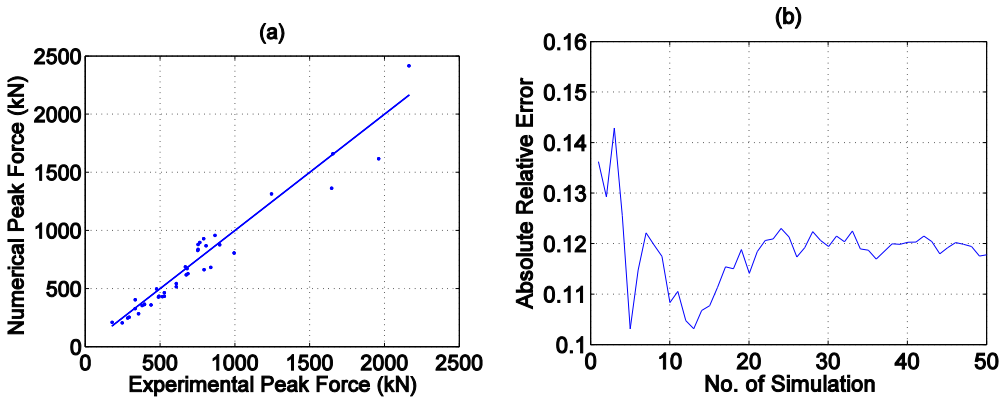

Figure 4-8. (a) Comparison of the peak forces form numerical model and experimental test data. (b) Mean value of the absolute relative error of the numerical model versus experimental tests.

A total of 50 experimental tests were simulated in the validation phase to evaluate the numerical modeling strategy. Appendix II provides these experimental test data and the result of the equivalent FSI simulations. Figure 4-8 plots a comparison of the vertical loads for these tests. This figure shows a good agreement between the results of the experiments and numerical simulations. The maximum difference incurred for one of the test of Sheppard and Marin (2009) is about 20%. The mean of the experiment and numerical model is almost the same value; i.e., the mean value of the error is zero which means the numerical model is unbiased. The mean absolute relative error of the numerical model is plotted in Figure 4-8 (b). This plot reveals that the absolute error estimate has reached a constant value after approximately 30 simulations. Therefore, a reasonable accuracy with a small error is achieved in the numerical model. After these validations, the model can be

applied confidently to study the performance of coastal bridges under storm wave and surge loads. The validated FSI model is utilized for reliability assessment, as presented in the next chapters.

4.2.5. Deterministic Response for a Case Study Bridge

This section illustrates the deterministic response of a case study bridge from Houston/Galveston Bay area. Figure 4-9 depicts the case study bridge geometry. The deck width is 11m and consists of a 0.2m thick slab with six AASHTO type III girders. The bent beam is supported by three square columns of 0.8m dimension and 5m height. The columns are reinforced with twelve 28mm diameter rebars in the longitudinal direction and a spiral with a pitch of 0.25m in the transverse direction. The columns are supported by a pile foundation consisting of a 2.6m square pile cap and eight 0.4m diameter piles of 14m length. The bridge is assumed to be located at a soft clay site which is the typical soil type in the Houston/Galveston region. This means a cohesive soil condition with undrained shear strength of 30kPa.

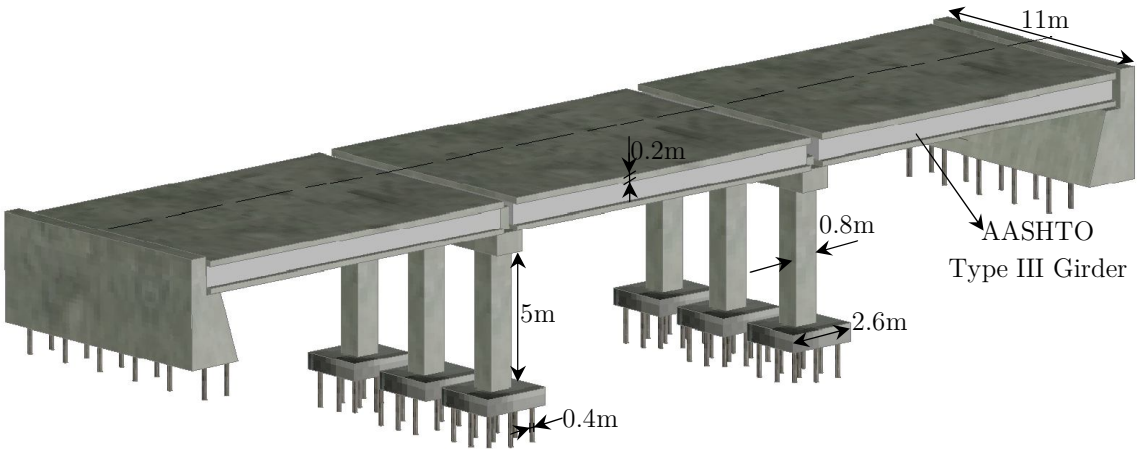

Figure 4-9. Case study bridge geometry.

The deterministic response of the developed FSI model is provided here in order to increase insight on the response of simply supported span bridges under extreme wave and surge condition. Key quantities monitored include the hydrodynamic forces on superstructure and substructure, and horizontal and vertical displacement of the superstructure. Since there is no connection between the super- and substructure, the bridge is susceptible to deck movement and unseating under extreme wave and surge loads. The hazard input parameters for the considered scenarios are presented in Table 4-1. The second and third combinations of wave and surge values are selected to produce vertical forces that are larger than the uplift capacity (i.e., weight of the deck for the case study bridge) according to AASHTO (2008). The fourth row, hazard scenario 3-L,

contains the same hazard parameters as the third one; however, the turbulence is neglected in this scenario (i.e., the fluid flow is considered to be laminar).

Table 4-1. Hazard parameters for the deterministic study.

No.	H_{max} (m)	T_p (s)	d_s (m)	Z_c (m)	
1	1.8	5.0	6.0	0	
2	3.2	6.0	6.0	0	
3	4.2	6.0	7.5	-1.5	
3-L	4.2	6.0	7.5	-1.5	(laminar flow)

Figure 4-10 depicts the vertical and horizontal displacement time history of the top waveward node of the deck for each scenario. The deck displacements for scenario 1 are small and are in the order of magnitude of 10^{-4}m. However, hazard scenarios 2 and 3 (and 3-L) lead to deck shifting and unseating. Scenarios 3 and 3-L lead to similar responses, as expected. Nevertheless, the vertical deck displacement for the laminar flow (case 3-L) is slightly less than the turbulent flow model (case 3). Therefore, it is recommended to use the turbulent flow model for higher accuracy since it is believed to provide a better representation of the problem than laminar flow model. More discussion on the flow assumption is provided in the sensitivity study in Section 5.2.2. The results indicate that the deck displacement is different for scenarios 2 and 3, underscoring the impact of surge and wave levels on bridge response with FSI. Vertical forces and

consequently vertical displacements are larger for the submerged deck (scenario 3). On the other hand, lateral forces and displacements are larger for the deck located at the waterline since the wave crest can directly impact the deck (scenario 2). Additionally, the submerged bridge deck undergoes larger moments as well as larger rotation. Due to these differences in responses, greater distortion occurs in fluid elements for scenario 3, and the simulation stops before a full wave passage. Figure 4-11 shows the displacement of the deck during wave and surge load for hazard scenarios 2 and 3 at time 1.7s. Differences in the displacement response and the rotation of the leeward part of the submerged deck are evident. After the bridge deck is shifted, the contact area between super- and substructure decreases. Thus the bridge deck has less resistance against the next wave cycle, as can be seen in Figure 4-10 (b) for scenario 2.

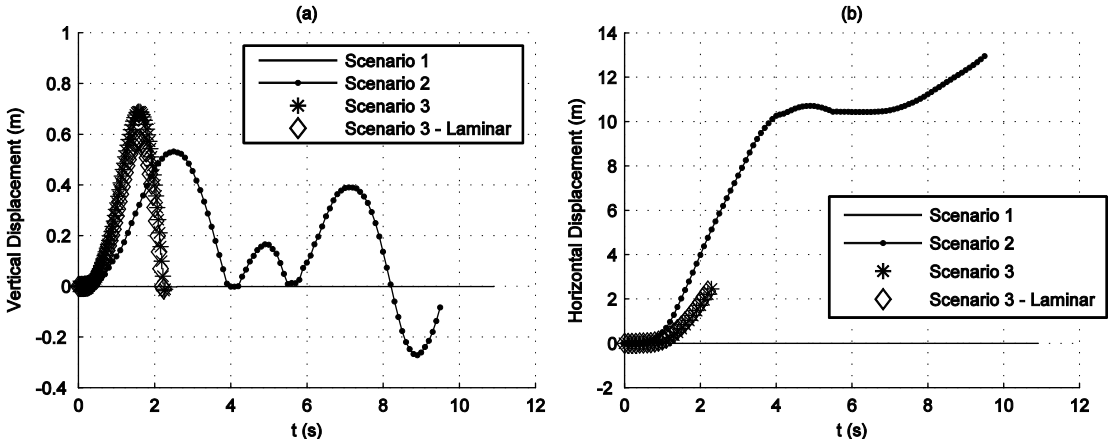

Figure 4-10. (a) Vertical and (b) horizontal deck displacements under different wave and surge load scenarios.

(a) (b)

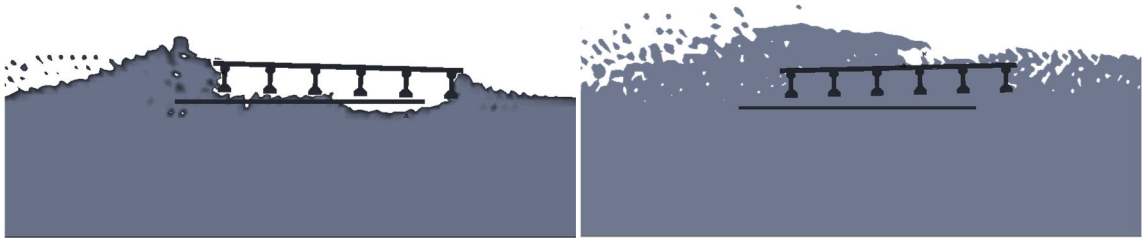

Figure 4-11. Deck displacement under wave and surge action at time 1.7s: (a) scenario 2; and (b) scenario 3.

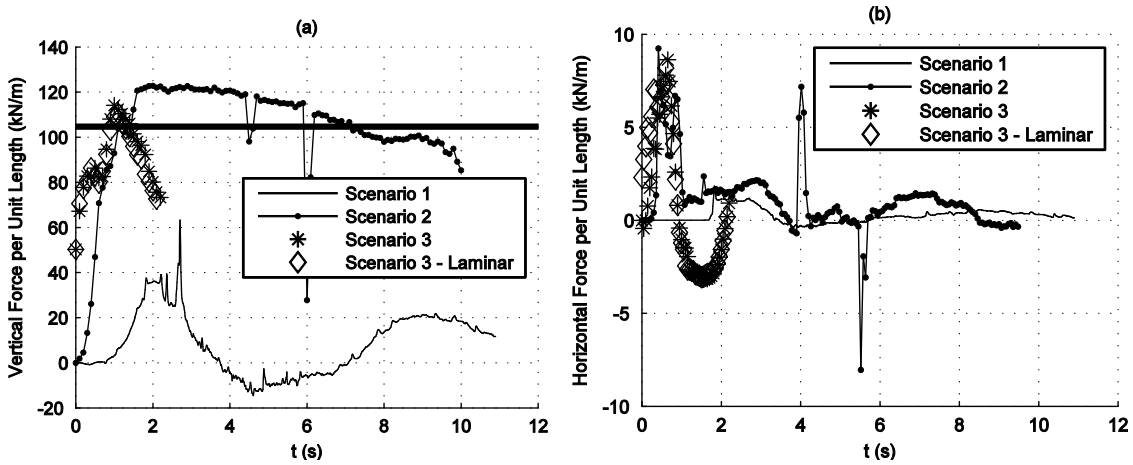

Figure 4-12. (a) Vertical and (b) horizontal forces per unit length on the superstructure. The bold line in (a) represents the weight of the bridge deck per unit length.

In addition to displacements, the total forces per unit length imposed on the bridge deck are plotted in Figure 4-12. The deck weight is shown in a bold line. Vertical forces on the bridge deck for scenario 1 follow a sinusoid pattern, similar to the trend observed in the experiment (Sheppard and Marin 2009). Nonetheless, the force pattern is not sinusoidal for scenarios that lead to the rigid body movement of the deck. It should be noted that all the experiments restrain the

deck movement; therefore, this phenomenon has not been observed (A preliminary experimental result of the unrestrained deck is presented by Cox et al. (2012) in the *ATC-SEI Advances in Hurricane Engineering Conference*, which supports the results of FSI the model). The vertical forces do not increase significantly after the deck uplift. The initial vertical forces for scenarios 3 and 3-L are greater than zero due to the buoyancy. By comparing Figure 4-10 and Figure 4-12, it can be concluded that the waveward face of the deck can be uplifted before vertical forces fully overcome the deck weight. However, significant transverse displacement occurs after the full deck uplift. Also, Figure 4-12 (b) reveals an alteration in the direction of horizontal forces on the submerged bridge deck (3 and 3-L) after deck uplift. The vertical forces are almost identical for turbulent and laminar flow. However, there is a slight difference in the horizontal forces. The maximum difference in terms of horizontal forces between turbulent and laminar flow models is 2.1%.

As mentioned in Chapter 3, wave and surge loads on the bridge substructure can be approximated based on the Morison equation (1950). The fluid domain should be solved to find the acceleration and velocity of water particles before using the Morison equation. Acceleration and velocity fields are time and

spatially varying; i.e., they are not constant along the column height. Since the water is relatively shallow, and large wave heights are expected during coastal storms, linear wave theory is not applicable to solve the fluid domain. Therefore, the stream function (Dean 1965) is employed to solve the fluid domain for the velocity and acceleration. The stream function solves the Laplace equation with a nonlinear free surface boundary condition by computing a series solution. A computer code, originally developed by Chaplin (2012) is modified to calculate the stream function and the velocity and acceleration of water particles at any given point of time and space for the given wave profile. This computer code automatically increases the stream function order to reach an accurate water surface that matches the input profile. After solving the fluid domain, forces are calculated by integrating Equation (3-5) over 50 points along the column height.

Figure 4-13 (a) compares the horizontal velocity of water particles at elevation 1.2m from the channel bottom line obtained from the stream function and the FSI model for the first hazard scenario. Also, Figure 4-13 (b) depicts the water velocity profile for hazard scenario 1 under the wave crest. This figure shows a good agreement between the theoretical (stream function) and numerical model. A similar trend was observed for other locations and other hazard scenarios.

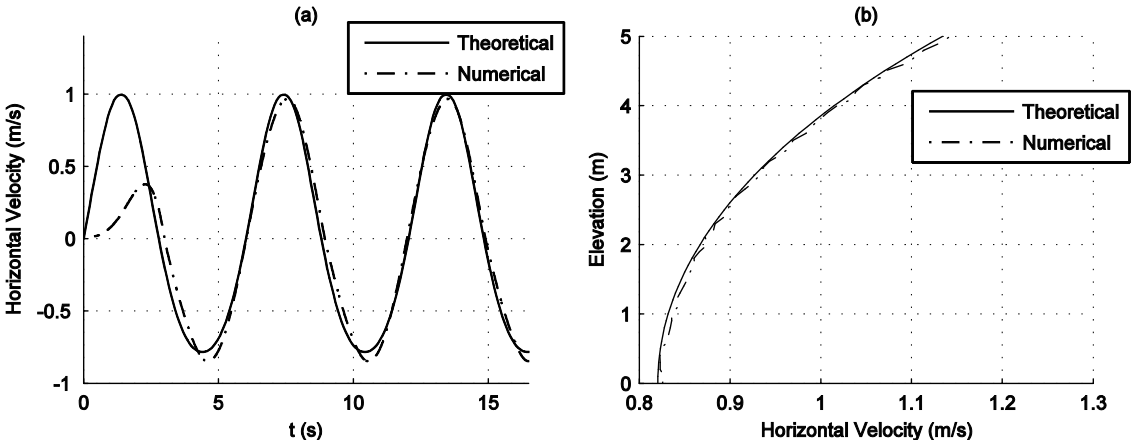

Figure 4-13. Horizontal water velocity at 1.2m elevation; and (b) horizontal water velocity profile at wave crest for scenario 1. Theoretical values are calculated from the stream function, where numerical values are the results from FSI model.

Horizontal forces on the waveward column for the first hazard scenario resulting from the numerical model and the Morison equation are shown in Figure 4-14. The C_d and C_m coefficients in the Morison equation are taken equal to 1 and 2, respectively. Although the fluid domain is in good agreement, the forces from the Morison equation are smaller than the numerical model. This is because the Morison equation does not consider wave diffraction, which is not an accurate assumption for the column width in the case study bridge. Therefore, the Morison equation does not lead to conservative results for estimation of forces on substructure. Nevertheless, the forces on the substructure are significantly smaller than the forces on superstructure, and they do not govern the behavior of the bridge response, as it is demonstrated in the sensitivity study analysis in Section

5.2.2. Therefore, no modification is proposed for the substructure forces that are calculated from the Morison equation.

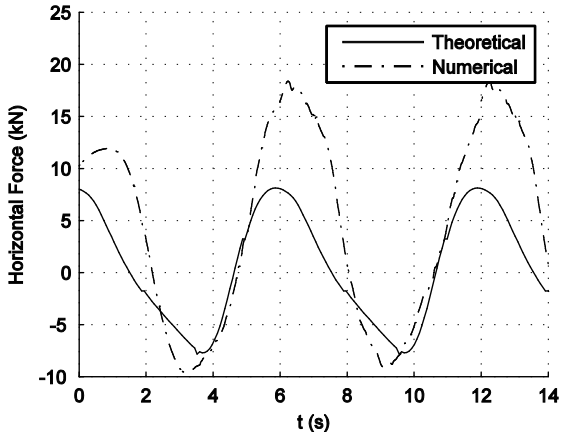

Figure 4-14. Horizontal forces on waveward column for scenario 1. Theoretical values are calculated from the Morison equation (1950), where numerical values are the results from FSI model.

4.3. Summary

This chapter introduced two different numerical models that are developed to assess the vulnerability of coastal bridges under storm wave and surge loads. The first model only includes the structural domain, and thus, is more computationally efficient. The second model includes a full fluid-structure interaction model which is verified by comparison with experimental test data from the literature. This model is computationally intense; however, it can be used for validation of the simplified models. Additionally, this model can be implemented to adjust the wave

and surge load models applied to the structure only simulations. The two developed numerical models are used in the following chapters for probabilistic study and reliability assessment of coastal bridges.

Chapter 5

Hurricane Hazard Parameters and Uncertainty Treatment

This chapter explores the hazard intensity measures that should be adopted to condition the fragility models for coastal bridges. Also, this chapter defines the random variables that should be considered in the probabilistic analysis. Appropriate probability density functions are introduced for hazard and structural random variables. The significance of different modeling parameters are identified by conducting a sensitivity study using the developed FSI model.

5.1. Determination of the Most Influential Parameters for Hurricane Hazard

The reliability assessment of coastal bridges is decoupled from the hazard probability. The coastal bridge reliability is conditioned upon the most influential hazard parameters, known as intensity measures (*IM*s), as presented in Equation (1-1), and repeated here for convenience:

$$P_F = \mathrm{P}\left[\mathrm{G}(C,D) \le 0 \mid \mathbf{IM}\right] \tag{5-1}$$

where **IM** is the vector of hazard intensity measure for the reliability problem in hand. The identification of the hazard intensity measures is the first step towards the development of fragility surfaces. The goal of this section is to define the influential hazard parameters in the response of the coastal bridges that can be employed as the intensity measures. A sample case study bridge model developed in OpenSees (2012) is used for this study.

Due to its prevalence and evidenced vulnerability, detailed three dimensional nonlinear finite element model of a representative multi span simply supported concrete girder bridge is developed in OpenSees (2012) in order to investigate the dynamic response due to hurricane induced wave and surge load

and test the validity of alternative *IM*s for predicting the structural response. The basis of this model is discussed in details in the previous chapter. A succinct overview of the model is provided herein. While one basic geometry is analyzed (Figure 5-1), three different common connection types for the bridge class are considered.

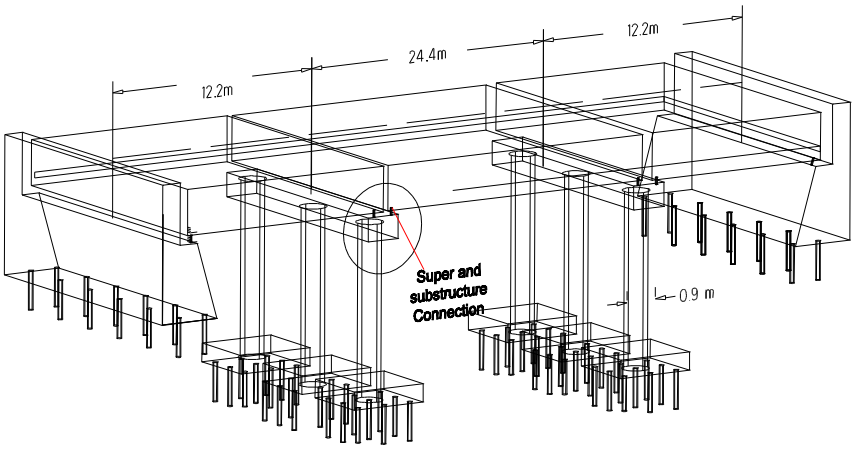

Figure 5-1. Bridge model 3D view.

The bridge model consists of three spans with varying length; the outermost spans with a length of 12.2m and the middle span length of 24.4m. The substructure consists of two bent caps, each with three circular concrete columns of 0.9m diameter. The outmost sides of the bridge are sitting on the abutments. Bridges with no and limited capacity connections between the deck and its supports are considered in this research. The latter case consists of contact

elements that are used in parallel with dowel bars. Two types of failure are considered for the dowel: 1) pullout failure, where the embedment length is less than the required development length; and 2) yield of the dowel, where the embedment length is sufficient to achieve the yield strength of the dowel. Details on the calculation of dowel and anchors properties are provided in Section 6.1.2.

Before comparing intensity measures for reliability analysis, a sample deterministic response analysis is provided to illustrate the dynamic response of the representative bridge with pullout dowel. The results shown for wave and surge loading that corresponds to typical Hurricane Katrina conditions observed in select locations (Biloxi Bay). The bridge is loaded with the Modified AASHTO loads presented in Chapter 3. The loading is sufficient to pullout the dowels, permitting the bridge deck to uplift off of its supports and displace transversely, as shown in Figure 5-2. The supposed embedment length for dowel is about 250mm, and as it is shown in Figure 5-2, after this displacement the dowel is completely pulled out and does not carry any more force.

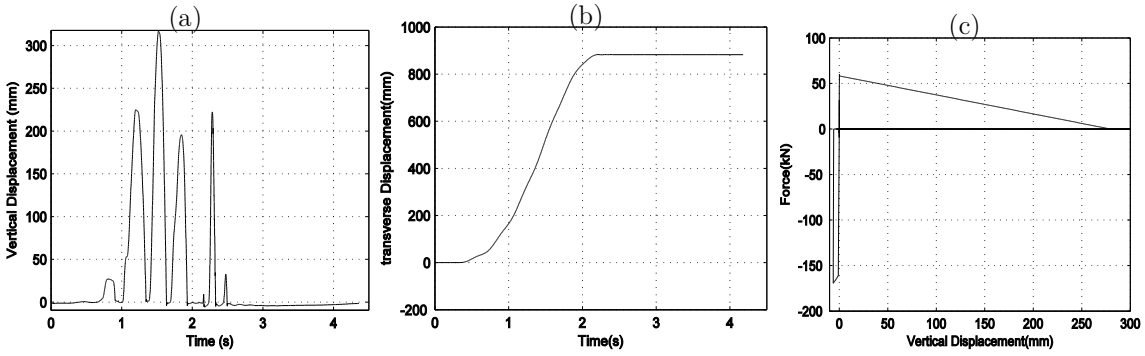

Figure 5-2. (a) Vertical; and (b) transverse deck displacement. (c) Dowel force-deformation diagram.

A suite of deck loading time histories are required to conduct the assessment of probabilistic bridge response, representative of reasonable combinations of hazard parameters exhibited in hurricane events. In this study, a set of hazard parameters from past hurricane events have been extracted from empirical data documented by NOAA (2010). A total of 30 coastal and onshore parameter records from Danny, Floyd, Katarina, Rita and Ike are considered. The hazard parameters required to estimate the wave and surge forces are wave height, length, and wave period, as well as relative surge elevation. Since wave length is not available in records, it has been estimated using proposed equation in AASHTO (2008) specification:

$$\lambda = \frac{gT_p^2}{2\pi}\sqrt{\tanh\left(\frac{4\pi^2 d_s}{T_p^2 g}\right)} \tag{5-2}$$

The relative surge elevation is varied for each of the 30 records, from $0.6H_{\max}$ to -1m, yielding a total of 300 simulations of deck loads for each bridge type. These loads are applied as input to the nonlinear finite element model in order to find the maximum demands or response of bridge components and relation to the hazard measures. Table 5-1 summarizes the range of the hazard parameters. A full description of the hazard parameters for these simulations is provided in Appendix III.

Table 5-1. Range of wave and surge parameters.

Parameter	Unit	Minimum	Maximum
Maximum wave height, $H_{\max}$	m	0.66	9.78
Wave length,	m	24.43	137.02
Wave period, T_p	s	3.8	14.1
Relative surge elevation, Z_c	m	-1.0	$0.6H_{\max}$

It should be noted that if the vertical wave force exceeds the span weight and connection resistance force, the vertical and transverse displacements will increase at a great pace, which indicates complete unseating of span. In these cases, the structure is considered to reach its collapse. These observations indicate that simply supported bridges with relatively limited super- to substructure connectivity reach their failure limit, which is deck unseating, if the hazard parameter is greater than a certain value, but remain almost intact for the values less than that. As

shown in Figure 5-3, plotting structural demands versus any of the considered wave and surge parameters alone does not predict the response of the structure due to the large variance in the prediction. Any function (such as linear, polynomial, and exponential) that is fitted to relate the deck displacement demand to any of the wave and surge parameter provides poor goodness-of-fit measures and R^2 values of 0.1 to 0.2.

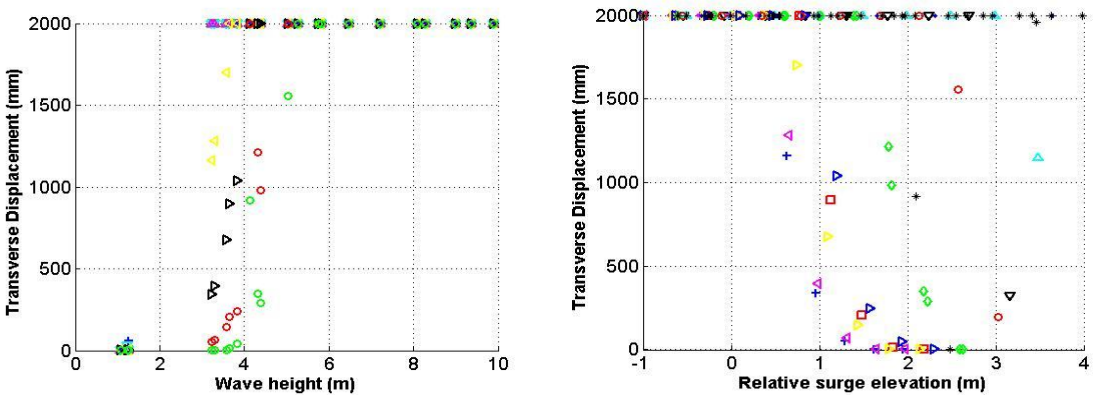

Figure 5-3. Bridge response (transverse deck displacement) versus two different hazard parameters: (a) wave height; and (b) relative surge elevation.

The above results suggest that the failure probability is conditioned on at least two or more hazard parameters; for example considering any wave parameter and the relative surge elevation. In general, the results of analysis support the intuitive fact that as relative surge elevation decreases, demand (i.e. deck displacement) increases, as shown in Figure 5-3. However, for small wave

parameters, the response is almost zero, and variation in relative surge elevation does not have any effect. The converse argument is also true. Implementing the relative surge elevation as one of the *IM*s is critical, since the responses change clearly with its alteration. In addition, the three wave parameters are related to each other, as for example in proposed equations of AASHTO (2008), and other ocean engineering literature (Le Roux 2007). Hence, it is not rational to employ all of them independently. Thus, a two parameter vector based intensity measure should be implemented in order to assess the failure probability of the structure, given relative surge elevation along with any of the wave parameters. Implementing wave length or wave period yield similar results in terms of uncertainty introduced in the assessment. Combination of wave length with relative surge elevation as the intensity measure vector gives a standard deviation of 0.36 in the representation of system probability of failure. Selection of the wave period and relative surge elevation as intensity measures generates a standard deviation of 0.41 in the estimation of the deck probability of failure. The best result is achieved by utilizing wave height and relative surge elevation as the intensity measures. The standard deviation reduces to 0.11. Additionally, "hazard computability" is also considered in the *IM* selection. Interpreting computability as

the availability of data, or level of effort requiring to generate an estimate of the hazard parameter, wave height is the most hazard computable (NOAA 2010). Wave length and in some cases wave periods are less readily available from hazard assessments or recorded data from past events. Figure 5-4 plots the response of the bridge deck versus relative surge elevation that is categorized into groups of constant wave height. A clear relationship between the hazard intensity measures and bridge demand can be observed. Therefore, relative surge elevation and maximum wave height are the two hazard parameters that are selected to condition the fragility of coastal bridges upon. These two parameters are used in the following of this research as the intensity measures.

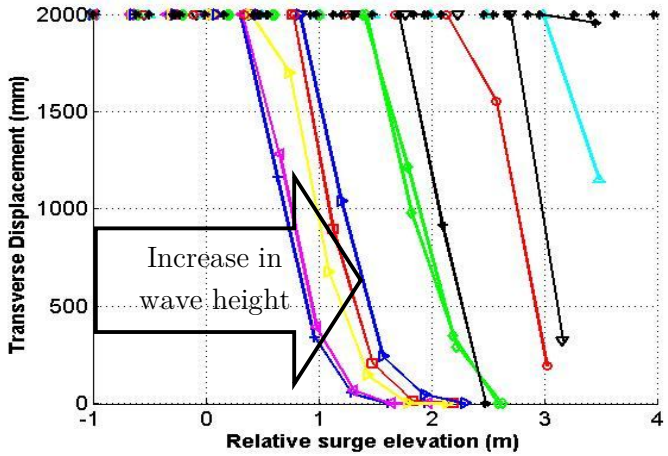

Figure 5-4. Transverse deck displacement versus relative surge elevation categorized by different wave height.

5.2. Random Variables and Uncertainty Treatment

5.2.1. Hazard Random Variables

In the reliability assessment, modeling parameters are considered as random variables and their associated uncertainties are captured by employing appropriate probability distribution functions (PDFs). Relative surge elevation and maximum wave height are defined as the intensity measures of interest for conditioning the reliability model based on the results of the previous section which suggest they offer the most efficient predictors of response. However, randomness in other hazard parameters that are not employed as intensity measures should be captured and propagated in the reliability assessment. For any given value of wave height, wave period is calculated from the joint PDF of wave height and wave period proposed by Longuett-Higgins (1983) joint probability distribution:

$$f(\xi,\varsigma) = L(\xi / \varsigma)^2 \exp\{-\frac{\xi^2}{2}[1 + (1 - \frac{1}{\varsigma})^2 \frac{1}{\nu^2}]\}$$
$$L = (1 + \frac{\nu^2}{4})\frac{1}{\sqrt{2\pi\nu}} \tag{5-3}$$

where ξ and ς are dimensionless wave height and wave period respectively, and are defined as:

$$\xi = H / \sqrt{m_0}\ ; \qquad m_0 = (H_s / 4)^2; \\ \varsigma = T_P / \overline{T} \tag{5-4}$$

where H_s is the significant wave height, m_0 is the first spectral moment, which is the area under wave spectrum, and commonly approximated by the above equation (Sorenson 1993). A wave spectrum indicates the amount of energy at different frequencies. $\overline{T}$ is the mean wave period, and ν is the bandwidth of the wave spectral density. In general, the value of ν is small during the storm surge and is taken as 0.3 according to suggested values by Massel (1996). The value of mean wave period during storms does not vary significantly. For example, Sorenson (1993) reports on the mean wave period of about 6s during storms. Therefore, fragility surfaces for each bridge are constructed with the mean wave period ranging from 5s to 7.5s, using a uniform distribution. H_s can be related to the maximum wave height (AASHTO 2008):

$$H_{\max} = 1.8 H_s \tag{5-5}$$

Wave length is related to the wave period (AASHTO 2008) as presented in Equation (5-2).

Table 5-2 summarizes all the hazard parameters and their associated distributions.

Table 5-2. Hazard parameters.

Parameter	Symbol	Distribution	Unit
Maximum wave height	$H_{\max}$	predictor (IM)	m
Relative surge elevation	Z_c	Predictor (IM)	m
Wave Period	T_p	Longuett-Higgins = 0.3, mean wave period = 5 s ~ 7.5 s uniform	s
Wave length	λ	Function of T_p	m

5.2.2. Sensitivity Study for Structural and Fluid Random Variables

Variation in hazard parameters can significantly affect the dynamic response of the bridge. However, structural and fluid modeling parameters will also contribute to uncertainty in the response of the bridge under hurricane induced wave and surge action. The significance of modeling parameters can be assessed through a sensitivity study. The results of the sensitivity study can be further employed to restrain the dimensionality of the problem only to the significant parameters for reliability analysis without sacrificing the accuracy. To assess important modeling parameters, the fluid-structure interaction model is used for the sensitivity study. A space-filling Latin-hypercube experimental design strategy is selected for the

sensitivity study, given that this design type is specifically devised for computer simulations (McKay et al. 1979). The upper and lower bounds for each parameter are selected on the basis of probability density functions that reflect the uncertainty in the FSI modeling parameters. The random variables for the sensitivity study and their limits are shown in Table 5-3.

Table 5-3. Distributions and bounds of the structural and fluid parameters for the sensitivity study.

Parameter	Symbol	Distribution	Lower limit	Upper limit	Unit
Concrete strength	f'_c	Normal	392.7	537.4	MPa
Steel strength	f_y	Lognormal	12.5	29.5	MPa
Concrete density	ρ_C	Normal	2211.3	2588.4	kg/m^3
Coefficient of friction	μ	Uniform	0	1	-
Soil shear strength	c	Lognormal	18.9	44.8	kPa
Turbulence kinetic energy	k	Uniform	0.5×the value from (4-4)	1.5×the value from (4-4)	-
Turbulence rate of dissipation	ε	Uniform	0.5×the value from (4-4)	1.5×the value from (4-4)	-

The dead weight of the bridge span is assessed considering uncertainty in the unit weight of construction materials as well as workmanship or construction errors to reflect uncertainty in as-built plans relative to field condition. The median and coefficient of variation (cov) of concrete density is provided in JCSS (2001), where for ordinary reinforced concrete, the median density is taken as 2400kg/m^3 with a cov of 0.04 following a normal distribution. For steel, these values are

7850kg/m^3 and 0.01, respectively. The girder type and height are taken as deterministic, since the predominant construction type of the Houston/Galveston area for the girders is precast. In contrast, bridge decks are cast in place; hence they have the potential for larger variability in workmanship. To account for workmanship and construction errors, a uniform distribution for deck thickness is considered with lower and upper limit of 95% and 105% of the as-built plan thickness. Other geometric parameters that are required for the force estimation are considered deterministic, as their small practical variation yields a negligible effect on the magnitude of wave forces.

Strength and stiffness of the bridge structure is governed by steel and concrete strength. Probability distributions for concrete and steel strength are selected based on Ellingwood and Huang (1985). A normal distribution is adopted for the concrete strength with a *cov* of 0.17 and a lognormal distribution is adopted for the steel strength with a *cov* of 0.11. The friction coefficient in physical problems can vary from 0 to 1. According to ACI-318 (2008) the average friction for concrete surfaces is 0.6, and the maximum friction is 1. Therefore, the upper value of 1 is reasonable for concrete surfaces. Uncertainty in soil shear strength, which governs the pile stiffness and strength as presented in previous chapter, is

selected based on Zhang (2006). To the author's knowledge, there is no published probability distribution information for the turbulence model parameters. Therefore, to account for the uncertainty associated with the turbulence parameters, a uniform distribution was assigned to k and ε. The lower and upper levels are 50% and 150% of the calculated deterministic values from Equation (4-4). Upper and lower limits for random variables are selected based on the 5^{th} and 95^{th} percentile of their probability distributions.

Table 5-4. Geometry blocking for the hurricane response sensitivity study of the case study bridge.

Geometry Block No.	Column height (m)	Column width (m)	Deck and bent cap width (m)	No. of girders
1	5	0.8	11	6
2	6.5	0.9	14	7
3	4.5	0.6	9	5

A simply supported concrete girder span bridge is selected for the sensitivity study. This is the same bridge that was utilized in Section 4.2.5 to illustrate the deterministic response of the developed FSI model. Bridge geometry governs the structural demands and the response of the bridge under wave and surge loads. Therefore, three different geometrical configurations are used in the sensitivity study, which are presented in Table 5-4. Since geometry alters the nature of the bridge, it is considered as a blocking parameter. Using blocking is one way to deal

with heterogeneity caused by geometric parameters and to set a similar population of sample space together within each block.

Table 5-5 illustrates the space-filling Latin-hypercube experimental design for each block and each hazard input. One additional parameter termed laminar flow, which as the name suggests corresponds to the non-turbulent flow condition, is considered to examine the effect of turbulence. To generalize the result of sensitivity study, the experimental design's simulations are repeated for three different hazard inputs and three different blocks in order to avoid bias. Hazard scenarios are presented in Table 5-6. Given that there are three different blocking geometries, and the analysis is performed for three different hazard inputs, a total of 126 simulations are conducted for the sensitivity study. To provide a simple representation of the parameter levels adopted in each run, all parameters in Table 5-5 are scaled to the range of -1 to 1, thus it is easier to compare the maximum and minimum. The effect of parameters on the responses of the bridge is examined through measuring the change in the variance of the responses, known as analysis of variance (ANOVA). A statistical hypothesis test is performed on each parameter for the horizontal and vertical deck displacements, total forces on the superstructure and substructure, and the lateral drift of the columns. The initial

assumption, or null hypothesis, states that the given parameter is insignificant in affecting the bridge response. The rejection of the null hypothesis suggests that the alternative hypothesis is true; i.e., the parameter is significant in affecting the measured bridge response (Hayter 2002).

Table 5-5. Design of experiment for the sensitivity study.

Run number	f'_c	f_y	ρ_C	μ	c	k^*	ε^*	Laminar flow*
1	0.230	0.846	0.384	-0.846	0.384	NA	NA	✓
2	0.846	-0.076	0.230	0.384	-0.230	-1	-0.692	x
3	0.538	-1	-0.538	-1	-0.384	-0.692	0.076	x
4	-1	-0.846	-0.076	-0.230	0.076	NA	NA	✓
5	-0.076	0.230	0.538	0.230	-1	-0.384	1	x
6	0.076	-0.692	-0.846	0.846	0.692	NA	NA	✓
7	0.384	-0.538	0.692	-0.076	1	NA	NA	✓
8	-0.538	0.538	-0.384	1	-0.69	0.076	-1	x
9	-0.230	1	-0.230	0.538	0.846	NA	NA	✓
10	-0.384	0.692	0.076	-0.692	0.538	NA	NA	✓
11	-0.692	-0.230	-1	-0.384	-0.538	0.538	0.538	x
12	1	0.384	-0.692	0.076	-0.076	0.692	-0.230	x
13	0.692	0.076	1	-0.538	-0.846	1	-0.384	x
14	-0.846	-0.384	0.846	0.692	0.230	NA	NA	✓

* ✓ denotes laminar while x denotes turbulent fluid flow. NA denotes not applicable.

Table 5-6. Hazard parameters for three different scenarios.

No.	H_{max} (m)	T_p (s)	d_s (m)	Z_c (m)
1	1.8	5.0	6.0	0
2	3.2	6.0	6.0	0
3	4.2	6.0	7.5	-1.5

The results of the analysis of variance are shown in Table 5-7, where higher p-values indicate that the null hypothesis is statistically more valid than the alternative hypothesis. A level of 5% significance is adopted as a cutoff such that a p-value less than 0.05 denotes that the parameter significantly contributes to the response.

Table 5-7. p-value results for analysis of variance (ANOVA)*.

Parameter	Transverse deck displacement	Vertical deck displacement	Forces on superstructure	Forces on substructure	Drift of columns
k	0.847	0.762	0.693	0.892	0.843
ε	0.722	0.653	0.621	0.764	0.715
Laminar flow	0.183	0.073	0.091	0.199	0.342
f'_c	0.876	0.912	0.897	0.065	**0.042**
f_y	0.978	0.965	0.943	0.764	0.594
ρ_C	**0.032**	**0.021**	**0.057**	0.321	0.234
μ	**0.009**	**0.048**	**0.011**	0.256	0.275
c	0.234	0.432	0.541	**0.022**	**0.012**
Geometry	**0.003**	**0.002**	**0.006**	**0.015**	**0.024**

* Boldface denotes a p-value less than 0.05.

There are five parameters that are important in at least one of the structure's responses under surge and wave loading. Bridge geometry, considered as the blocking parameter, is significant in all of the responses as expected. The weight of bridge deck and stiffness and strength of the structure changes with alteration in geometry. The concrete strength and density influence the displacement response of the substructure and superstructure respectively.

Concrete strength significantly contributes to the structural stiffness, thus the lateral drift of columns. Concrete density changes the deck weight; which consequently alters the resistant uplift and frictional forces, thus the movement of the deck. Soil shear strength, that affects pile stiffness, plays an important role in affecting the columns' lateral drift and subsequently the forces imposed on the substructure. Friction between super- and substructure alters the transmission of forces from the super- to substructure. However, the effect is not as significant as the impact of friction on the deck movement. The results of the sensitivity study suggest that variation in the turbulence modeling parameters k and ε do not significantly affect the bridge response. These parameters are assigned to the numerical model as initial values, and they change as the simulation progresses in time. Therefore, the initial assignment of these parameters does not play an important role in the structural response. Nevertheless, it should be noted that the initial values are important to avoid difficulties in numerical convergence. In contrast, neglecting the turbulent effects by assuming a laminar flow may alter the forces and superstructure's displacement. Although the p-value for the laminar flow assumption is not in the significant range considered in the study, it is recommended to employ turbulent flow for a higher accuracy since the ANOVA

results suggests a potential impact on vertical deck displacement and forces on the superstructure. The results of the sensitivity study provide the critical parameters that should be considered as random variables in a reliability analysis of coastal bridges. As a summary for this section, Table 5-8 provides all modeling parameters that should be considered as random variables in the probabilistic study, and their associated PDFs.

Table 5-8. Structural parameters and their distributions.

			Distribution Parameters		
Parameter	**Symbol**	**Distribution**	**1**	**2**	**Unit**
Concrete strength	f'_c	Normal	m_n^*, from as built plans	$\zeta^\dagger = 4.3$	MPa
Steel strength	f_y	Lognormal	$m_l^\ddagger$, from as built plans	$\kappa^\S = 0.08$	MPa
Soil strength	c	Lognormal	$m_l^\ddagger$, from bridge location	$\kappa^\S = 0.22$	kPa
Concrete density	ρ_C	Normal	$m_n^* = 2400$	$\zeta^\dagger = 94.12$	kg/m^3
Steel density	ρ_S	Normal	$m_n^* = 7850$	$\zeta^\dagger = 77.21$	kg/m^3
Deck thickness	d_b	Uniform	$l^\| = 95\%$	$u^\P = 105\%$	m
Coefficient of friction	μ	Uniform	$l^\| = 0$	$u^\P = 1$	-

* Median value for normal distribution.

† Standard deviation for normal distribution.

‡ Median value of the equivalent normal for lognormal distribution.

§ Standard deviation of the equivalent normal for lognormal distribution.

$^\|$ Lower bound for uniform distribution.

¶ Upper bound for uniform distribution.

5.2.3. Realization of Random Variables

A large number of simulations is required for the reliability assessment of coastal bridges over the entire range of hazard parameters. It is important to have

appropriate techniques for generating realizations of the random variables for each simulation. Different sampling techniques have been introduced in statistics in order to reduced the variance of the results, and thus, provide a higher accuracy with lower number of simulations. The sampling technique that is employed in this research is known as quasi-Monte Carlo method (Boyle et al. 1997). Quasi-Monte Carlo generates low discrepancy sequences. Different methods exist for the generation of low discrepancy sequences. One of these methods, which is employed in this study is called the Sobol sequence number generator. The basic concept is to divide the sample space to have the minimum distance (holes) between the generated points. Therefore, unlike random sampling, it is important to know the number of simulations (N_{sim}) beforehand. Quasi-Monte Carlo ensures that the ensemble of realizations is representative of the real variability in the sample space. This sampling technique offers random variable realizations which ensure that the parameters space is covered uniformly and efficiently. Therefore, quasi-Monte Carlo sampling is the main sampling technique that is adopted in this research.

5.3. Summary

This chapter defines the most important hurricane wave and surge parameters that will be implemented as intensity measures for conditioning fragility surfaces of coastal bridges. Relative surge elevation, that delineates the elevation of free water surface with respect to the bottom line of the bridge deck, and maximum wave height are the two identified intensity measures for coastal bridge subjected to hurricane induced wave and surge. These two parameters are the most influential parameters on the response of the bridge, and provide the least variance in the prediction of the probability of failure of coastal bridges under hurricane events. Additionally, the uncertainty treatment in structural and hazard parameters are prescribed through the application of appropriate probability density functions. The critical random variables for analysis of bridges under hurricane events are determined through a sensitivity study. These random variables are materials' strengths and densities, coefficient of friction between the super- and substructure, and soil shear strength. The identified random variables will be utilized in conjunction with the developed numerical models (Chapter 4) and wave and surge load models (Chapter 3) to assess the performance of water crossing bridges in the following chapters.

Chapter 6

Reliability Assessment of Coastal Bridges: Structural Modeling Strategies

This chapter utilizes the numerical models presented in Chapter 4 along with the random variables defined in Chapter 5 in order to assess the vulnerability of the existing bridge infrastructure along the Gulf Coast. First, a method is proposed for efficient vulnerability assessment of water crossing bridges that couples static structural analysis with Monte Carlo simulation, which offers a viable approach for rapid screening of existing bridges across a region. Then, the nonlinear dynamic model with the Modified AASHTO loads along with the quasi-Monte Carlo sampling technique is introduced that can be implemented for a more accurate reliability analysis. Finally, the FSI model along with the quasi-Monte Carlo

sampling is introduced that can provide the highest accuracy; however it is more computationally demanding.

6.1. Monte Carlo Based Static Model Methodology for Bridge Deck Unseating

The goal of this section is to provide an efficient methodology to estimate the probability of deck unseating that can be implemented across regional portfolios of bridges for a rapid screening of vulnerable structures. The probability of unseating is assessed by comparing the vertical resistance of the superstructure with the maximum demand of the wave forces. Hence, this method is most readily applicable to simply supported bridges lacking supplemental restraints such as restrainers or shear keys, where, according to the field observation, deck unseating is the most common mode of failure (Chen et al. 2009; Padgett et al. 2008).

Since the required computational and modeling effort to assess the analytical fragility of each individual structure is high, it is a common practice for other hazards to estimate the mean fragility for bridge classes by performing simulations on representative bridge structures for each class (Basoz and Kiremidjian 1999; Basoz and Mander 1999; Choi et al. 2004; Shinozuka et al.

2000). However, a better insight on the spatial distribution of potential damage under a given hazard in a particular area can be provided by developing fragility surfaces for each individual structure. Thus, this section proposes an efficient method for evaluating the vulnerability of each bridge structure and screening bridges susceptible to deck unseating failure mode under hurricane induced loads. Figure 6-1 depicts the schematic view of the procedure, including probabilistic estimates of the capacity and demand, which is explained in detail in the following subsections.

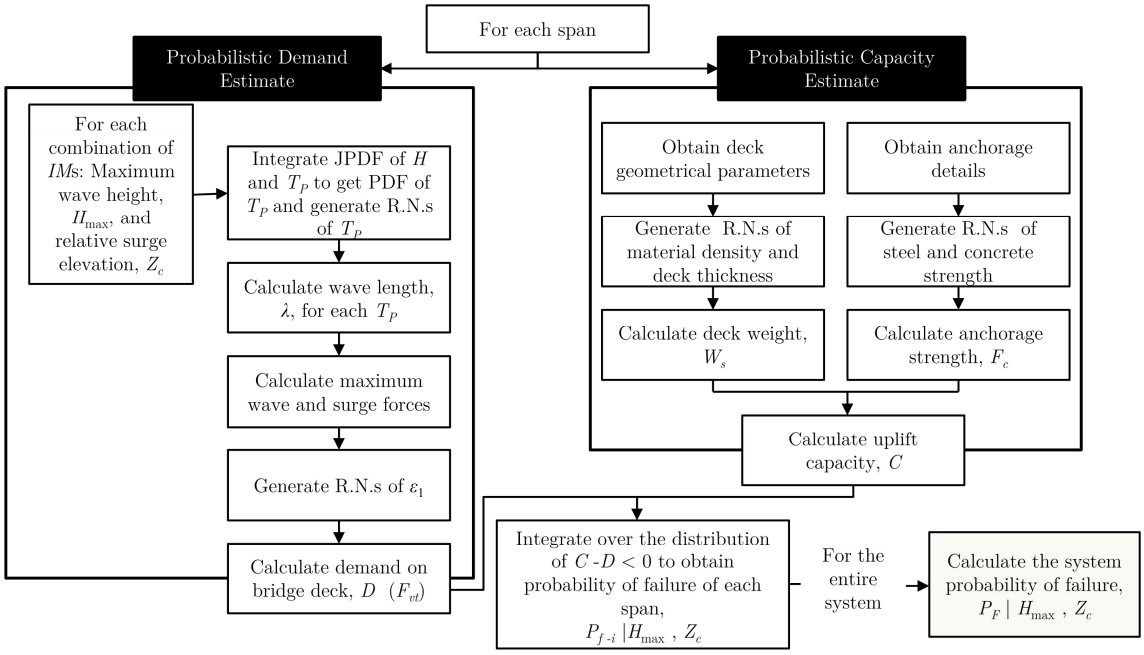

Figure 6-1. Schematic view of the proposed MCS Static Model approach (Note: R.N.= random number, PDF = probability density function, JPDF = joint PDF).

6.1.1. Probabilistic Demand Model

To assess the probability of deck displacement or unseating, the demands on the bridge deck must be characterized, including uncertainties in the realization of these demands. Adopting a reliable method to estimate wave loads on bridge decks is critical for such demand modeling of coastal bridges. The wave and surge loads that are used in this section are based on the proposed Modified AASHTO equations with bias removal presented in Section 3.2.2. The uncertainty in the random variables is shown in Table 5-2. Therefore, to calculate the probability density of maximum wave loads, for each combination of hazard intensity measures, $H_{\max}$ and Z_c, realizations of wave period is generated based on the quasi-Monte Carlo sampling using the Longuett-Higgins joint PDF, presented in Equations (5-3) and (5-4). Wave length is calculated as a function of wave period from Equation (5-2). Finally, maximum forces are calculated from Equations (3-6) to (3-14). Thus, the demand probability distribution is estimated for one intensity measure combination. This process is repeated for each combination of hazard intensity.

6.1.2. Probabilistic Capacity Model

The vertical resistance of the span to uplift consists of the dead weight of the deck as well as the connection strength between superstructure and substructure, if any exists. The uncertainties associated with material strength and material density are presented in Table 5-8. The probability density of capacity is estimated by generating realizations of random variables equal to the number of Monte Carlo simulations and calculating the corresponding capacity. The weight of each span per unit length is then calculated as follows:

$$W_s = (d_b W + A_g \times N_g)\gamma \tag{6-1}$$

where W_s is the span weight per unit length, d_b is the deck thickness, W is the deck width, A_g is the cross section area of the girders, N_g is the number of girders, and γ is the unit weight of the material.

In the cases where vertical connectivity is present, its contribution to the capacity model can be characterized by the pullout or yield strength of the dowel bars. If the anchorage between super and substructure is provided with bolts, the connection strength is estimated based on ACI 318 – Appendix D (ACI 2008). The

connection strength formula considering the uncertainty is presented in Equation (6-2):

$$F_c = n_b \times \min \begin{cases} \text{Steel strength, } N_s = A_{se} f_{ut} \\ \text{Concrete breakout, } N_{cb} = \dfrac{A_N}{A_{No}} \psi_2 \psi_3 N_b \times \varepsilon_2 \\ \text{Pullout, } N_{pn} = \psi_4 N_p \times \varepsilon_3 \end{cases} \tag{6-2}$$

where F_c is the connection strength, n_b is the total number of bolts per span, A_{se} is the area of the bolt, f_{us} is the ultimate strength of the steel, A_N is the projected area of the failure surface for the anchor, A_{No} is the projected area of the failure surface of a single anchor far from the edges, N_b is the breakout strength of an anchor far from edges, N_p is the pullout strength in tension of a single bolt, ψ_2 to ψ_4 are modification factors. Appendix IV provides the detail for calculation of anchorage strength according to ACI 318 (2008). No model error is considered for the steel strength. ε_2 and ε_3 are the model error terms for concrete breakout and pullout strength; where ε_2 has a normal distribution with the mean of 1 and *cov* of 0.23. The model error is presented by Eligehausen, et al. (2006) based on experimental test data. The concrete breakout is the most common mode of failure of the anchor bolts. The equation for pullout corresponds to the crushing of the concrete under the bolt head; pullout occurs after a significant volume of concrete

is crushed. Hence, it is unlikely to occur before the breakout. The same distribution as ε_2 is implemented for ε_3. If dowel bars connect the deck to the bent beam, their strength is estimated based on the assumption of uniform distribution of bond strength along the bar length (Zamora et al. 2003), namely nominal bond strength, which can be used in deriving the development length equation (Leet and Bernal 1997; MacGregor 1997). Based on this assumption, the dowel bar strength is estimated from Equation (6-3), which shows that the dowels are assumed to reach their yield force if the embedment length is greater or equal to the development length; otherwise, pullout governs the ultimate capacity of the dowels.

$$F_c = n_b \times \pi d_{se} l_{emb} \varphi_b \le n_b \times A_{se} f_y;$$
$$\varphi_b = \frac{f_y d_{se}}{4 l_d} \tag{6-3}$$

where φ_b is the bond strength, d_{se} is the reinforcement diameter, l_{emb} is the embedment length of the dowel, and l_d is the development length estimated based on (2008):

$$l_d = \frac{\gamma_{ld} f_y}{20\sqrt{f_c'}} d_{se} \tag{6-4}$$

where γ_{ld} is the reinforcement size modification factor and is equal to 0.8 for reinforcements No. 6 and smaller, and 1 for larger reinforcements. No model error is considered for the pullout equation, although uncertainty in model input parameters are considered. It is noted that probability density functions for the steel and concrete strengths are used to ascertain the bond strength and connection capacity. The summation of the deck weight and connection strength per unit length is the total uplift capacity of the deck per unit length, C:

$$C = F_c / L_s + W_s \tag{6-5}$$

6.1.3. Fragility Modeling

After attaining the probability distributions of capacity and demand placed upon each bridge span as explained in the previous subsections, probability of span failure can be assessed. A total of 400 sample points across the range of intensity measures are generated. The generated wave and surge profiles cover the entire reasonable range of hazard by selecting 400 points that span the range of $H_{\max}$ and Z_c from 0 to 5m and 2m to -2m, respectively. Fragility surfaces are obtained by performing 7000 Monte Carlo simulations for each combination of *IM*s per unique span of each bridge where quasi-Monte Carlo sampling technique is used for

generating the realizations of each ransom variable. The probability of failure is estimated by integrating the area under limit state function (demand minus capacity) distribution. The number of simulations was selected to achieve convergence with absolute error less than 0.01 in the failure probability estimate.

The assessment of probability of deck unseating of the whole bridge as a system is determined by combining the effect of each individual span. The bridge is modeled as a series system, where unseating of any one span constitutes system failure, and spans are considered to be independent. Hence, the probability of the deck shifting or unseating for the entire bridge with n spans, P_F, is the union of probability of failure of each individual span, $P_{f\text{-}i}$:

$$P_F = \mathrm{P}\left[\bigcup_{i=1}^{n} E_{fi}\right] = \mathrm{P}\left(\bigcap_{i=}^{n} E'_{fi}\right)' = 1 - \prod_{i=1}^{n}\left(1 - P_{f-i}\right)$$

where

$$P_{f-i} = \mathrm{P}\left[\mathrm{G}(C,D) \le 0 \mid \mathbf{IM} = \mathbf{s}\right] = \mathrm{P}\left[F_{Vt} \ge \frac{F_c}{L_s} + W_s \mid Z_c = z, H_{\max} = h\right] \tag{6-6}$$

where E_{fi} denotes the event of failure for the i^{th} span of the bridge. While the physics of the problem tend to support the independent failure assumption which is an upper bound estimate, potential sources of correlation are acknowledged and the sensitivity of the results to this assumption is examined. The probabilities of failure

for the independent (upper bound, as considered in the current methodology) and fully dependent (lower bound) cases were compared for a regional inventory of bridges described in Section 9.2. The vast majority of bridges exhibit narrow bounds with variations in unseating failure probability of less than 10%. Figure 6-2 shows example fragility surfaces for a multi span concrete slab and a multi span concrete girder bridge. The surfaces are generated without fitting any equation to the results. The MATLAB® (MathWorks 2004) built-in Delaunay function is used to generate triangulation over the probability results in order to construct the surfaces. Figure 6-2 suggests that a failure zone emerges with a dramatic transition in probability of failure. This characteristic of the fragility surface is observed for most of the Houston/Galveston Bay area bridges analyzed, and can be attributed in part to the fact that the wave loads are sensitive to the value of Z_c, since a small change in the surge elevation leads to significant alteration in the forces. Therefore, the bridge is either failed or intact across most of the hazard range when considering the deck shifting/unseating failure mode for limited connectivity bridges. The border of this "transition zone" can be approximated by a linear relationship between maximum wave height and relative surge elevation. For the presented fragility surface, the equation of this transition line is provided in Figure

6-2. Such a transition characterization provides a simple strategy for screening potentially vulnerable bridges for a given scenario event, or combination of surge and wave load parameters. Beyond this transition zone the probability of failure rapidly increases. More advanced statistical models to represent this transition zones, as well as the entire fragility surface, are presented in Section 7.3.

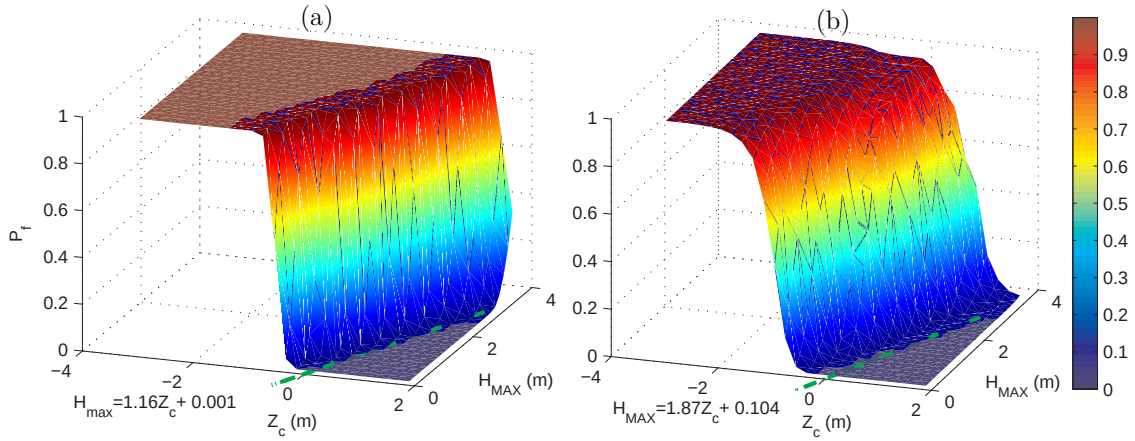

Figure 6-2. Fragility surface for a typical (a) concrete girder without anchors; and (b) slab bridge with dowel bar connections in the Houston/Galveston Bay area region and indication of transition zone.

The proposed methodology is directly applied to obtain the fragility surface for each bridge structure of in the Houston/Galveston inventory to support regional risk assessment, which is the recommended approach since the proposed method is computationally efficient and can be rapidly applied regionally. The application of this methodology to Houston/Galveston Bay area bridge inventory is

presented in Chapter 9. However, it is valuable to identify a metric that can be used to categorize bridges with similar trends in fragility and also succinctly summarize the range of fragility estimates observed in the case study region. Combining the fragility surfaces based on structural type alone does not provide a homogeneous class of bridges vulnerable to surge and wave, due to the variation in multiple critical features that affect the demand and capacity. As an example to illustrate the structural parameters that can potentially affect the fragility surface, Table 6-1 provides a sample input file for a bridge in the area. This table provides insight into the range of structural parameters affecting the fragility modeling and resulting fragility surface, that can be potentially used as a categorization metric for bridges vulnerable to deck unseating.

Table 6-1. Information extracted from as-built plans for each bridge span.

Bridge ID	Span type	Material	Width (m)	Girder area (m^2)	Girder height (m)	Haunch thickness (m)	Asphalt thickness (m)
12085097604	Slab, simply supported	Concrete	10.9	0.58	0.38	0.025	0
Span length (m)	f_y (MPa)	f'_c (MPa)	Dowel diameter (m)	Embedment length (m)	No. of dowels	Water clearance (m)	Depth (m)
15.2	413	25	0.032	0.15	4	2.7	0.9144

Bridges with same features are grouped together and their fragility surfaces are averaged. The best feature is selected based on the minimization of the

standard deviation of the resultant fragility from the output of simulation. Nevertheless, classifying the output based on any of these features alone does not provide a low variance for the combined fragility surface. However, most of these features can be united in one metric and implement to classify the bridges, which is span mass per unit length. As mentioned earlier, the defined limit state is relevant for bridges with the limited capacity connections between sub and superstructure; as a result the span mass directly affects the capacity, thus the probability of failure. Moreover, bridges with similar mass per unit length of span commonly have similar geometrical properties that influence the wave loading, such as girder height or deck width. Mean value of unit mass of span can be easily estimated from the as-built plans of the structure. Merging most of the properties of the bridge deck into this metric, three other metrics can also be considered: number of the spans, span length and water depth at the bridge location. The average surfaces for all of these classification metrics are calculated, and the results of these analyses along with the standard deviation are presented in Table 6-2. As the results in the table shows, span mass per unit length is the most appropriate measure for classifying the bridges. There is only a small improvement by using a higher level classification based upon two metrics, i.e. categorizing the bridges

based on mean mass per unit length and water depth. Hence, this study suggests classification based on the span mass per unit length is the most relevant and simple classification scheme for characterizing the unseating fragility of homogenous classes of bridges in hurricane prone regions. It is noted that the elevation of the bridge is captured in the *IM* of relative surge elevation, upon which the fragility is conditioned. Figure 6-3 shows the fragility curve for one of the bridge classes with mean span mass per unit length of 5-10 ton/m along with the corresponding 90% confidence bounds.

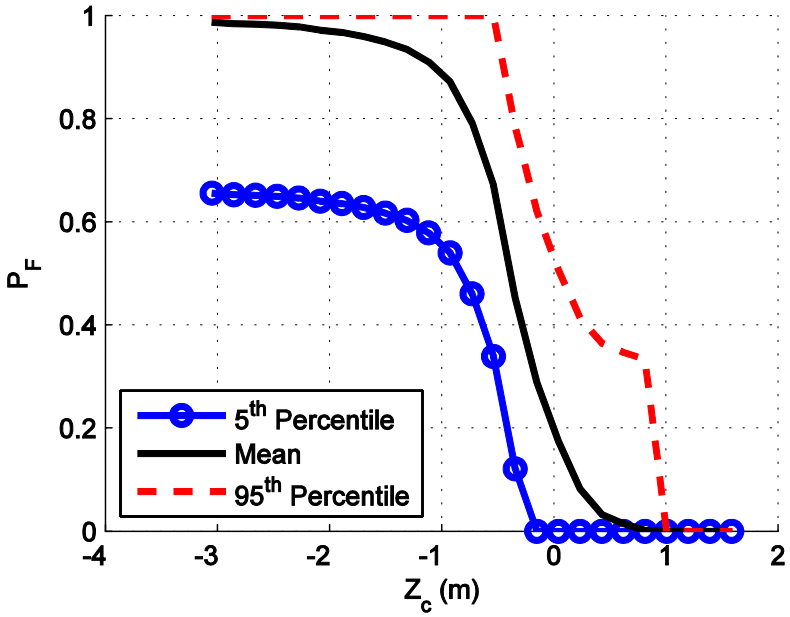

Figure 6-3. Fragility curve for the bridges with mean span mass of 5-10 ton/m at H_{max}= 2m.

Table 6-2. Bridge classification.

Classification Metric	Range	Unit	Standard deviation*
Mean span mass per unit length	0-5	ton/m	0.14
	5-10		0.17
	10-15		0.18
	15-20		0.15
	20-25		0.21
	25-30		0.17
	30-35		0.16
No. of spans	1	-	0.21
	2		0.24
	3		0.25
	4		0.27
	5		0.24
	6		0.16
	11		0.22
Span length	0-10	m	0.27
	10-20		0.28
	20-30		0.22
	30-40		0.25
	60-70		0.26
Water depth	<3	m	0.53
	3-6		0.29
	6-9		0.23

* Standard deviation of the mean fragility surface from the output of the simulation for each classification metric.

6.2. Dynamic Model Methodology for Bridge Deck Unseating

The use of nonlinear time history analysis is preferred over linear static approaches for reliability assessment of the structures since it can capture displacement based demands and account for accumulation of damage over time. The Dynamic Model employs the same random variables as the previous MCS Static Model. However,

there are two main differences: 1) one simulation is performed for almost the entire range of hazard intensity measures; 2) the modified wave loads time series are applied to the OpenSees nonlinear finite element model that is described in Chapter 4. One simulation is required for each hazard combination since the bridge deck unseating failure mode is brittle, and is either failed or survived, as shown in Section 4.2.5. Simulations results reveal that for typical simply supported bridges after the initiation of uplift, the bridge deck displacement increases at a rapid pace, as mentioned in Sections 4.2 and 5.1. For cases that the simulation results reveal that the deck displacement is greater than zero but it does not lead to failure (i.e., small displacement) a new set of Monte Carlo simulation is performed to evaluate the probability of failure (ratio of number of failed cases over the entire number of simulations). This situation denotes that the vertical wave forces are close to the deck weight. This situation occurs occasionally over the hazard range, and denotes the transition zone. A number of 300 simulations is performed over the *IM* combinations that lead to this transition zone. Typically, the probability of failure for this transition points is close to zero. The same random variables (Table 5-2 and Table 5-8) are used for the simulation. Quasi-Monte Carlo sampling technique is adopted to generate realizations of random variables.

The representative case study bridge from Houston/Galveston Bay area bridge inventory that was used in Section 5.1 is selected to demonstrate the application of Dynamic Model methodology for the fragility assessment of coastal bridges. The bridge is depicted in Figure 4-9. For the dynamic simulation, the bridge deck is considered as unseated if the transverse displacement is larger than 0.6m. This limit is also the approximate displacement upon which the leeward girder would lose support even if the deck did not displace any further. Given the abrupt nature of deck response under surge and wave loads, the outcome of the assessment is not sensitive to this imposed limit used to categorically distinguish "seated" (survived) and "unseated" (failed) cases.

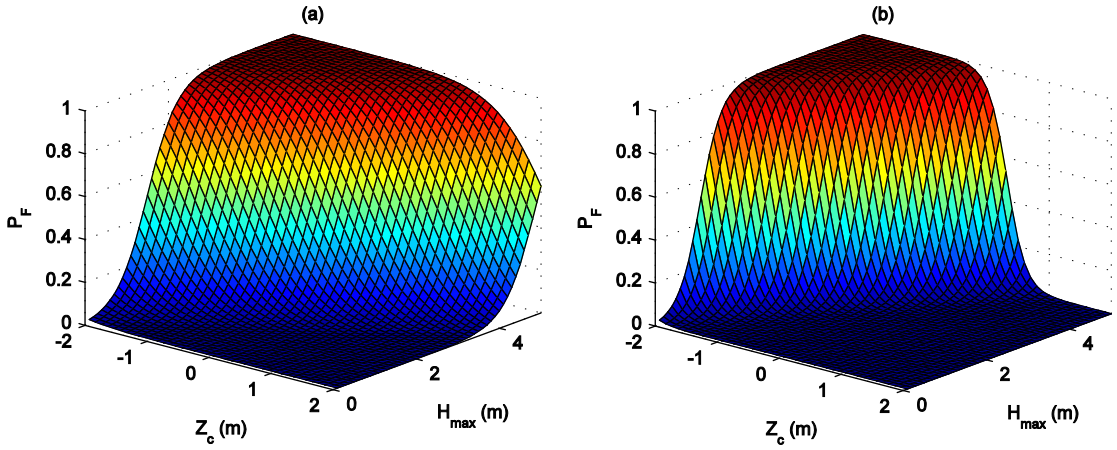

Figure 6-4. Fragility surfaces for the deck unseating: (a) MSC Static Model; and (b) Dynamic Model.

A total of 400 sample points across the range of intensity measures are generated. The generated wave and surge profiles cover the entire reasonable range of hazard by selecting 400 points that span the range of $H_{\max}$ and Z_c from 0 to 5m and 2m to -2m, respectively. Figure 6-4 depicts the comparison between the fragility surfaces constructed for the case study bridge using the Dynamic Model methodology and MCS Static Model methodology. The figure reveals that result of the Dynamic Model simulation is in agreement with the Static Model simulation. Higher accuracy of the Dynamic Model requires more computational time. Each dynamic simulation on a computer with Intel Core 2 Duo CPUs running at 2.33GHz takes about 15 minutes, where static simulation is less than a minute. Therefore, only for the deck unseating failure mode it is possible to implement the MCS Static Model with acceptable results. However, the application of the MCS Static Model is limited to simply supported bridges with no/minimal connections between the super- and substructure. The Dynamic Model or FSI Model should be employed for retrofitted bridges that can have other potential failure modes, as it would be discussed in Chapter 8 and Chapter 9. Next chapter will introduced different methods that can be used to generate a mathematical model over the data. These methods are coupled with different structural modeling methodologies

that are introduced in this chapter to construct fragility surfaces for coastal bridges. Thus, a comprehensive study on the performance of the MCS Static Model, Dynamic Model, and FSI Model methodologies are presented in Section 7.3.

6.3. FSI Model Methodology for Bridge Deck Unseating

The FSI Model methodology also implements the same random variables as the last methodology. The main advantage of this methodology is to use the fluid-structure interaction and detailed finite element modeling which can provide details on the performance of coastal bridges such as wave force variation over the time, local damages, and stress concentrations. The FSI Model can provide insight on the forces on bridge super- and substructure, as well as local and global damages and failure mechanisms.

This section constructs the fragility surface for the case study bridge from Houston/Galveston Bay area that was defined in Section 4.2.5. This bridge is used in the next chapter for all the modeling methods to provide a comprehensive comparison. As it was shown in the previous sections, the observed failure mode is abrupt; i.e., once deck movement is initiated, significant displacement occurs sufficient to result in bridge deck unseating. In total 256 samples are generated

which provide combinations of hazard and bridge model parameters for subsequent fluid-structure interaction simulation. The generated wave and surge profiles cover the entire reasonable range of hazard by selecting 256 points that span the range of $H_{\max}$ and Z_c from 0 to 5m and 2m to -2m, respectively. Quasi Monte Carlo sampling technique was used to generate realizations of random variables. The sample points are presented in Appendix V. As mentioned for the previous modeling methodologies, given the abrupt nature of deck response under surge and wave loads, the outcome of the assessment is not sensitive to this imposed limit used to categorically distinguish survived and failed cases. The result of the simulation is shown in Figure 6-5. As it can be seen the results are revealing a transition zone between the failed and survived region. The FSI Model provides the most accurate output in comparison to the MCS Static and Dynamic Model; however, it requires significantly more computational power. For example, each FSI simulation on a super computer cluster that has quad-core Intel Xeon processors running at 2.83GHz takes an average of 7 hours to complete. Each simulation of the Dynamic Model on the same machine takes less than 10 minutes to complete.

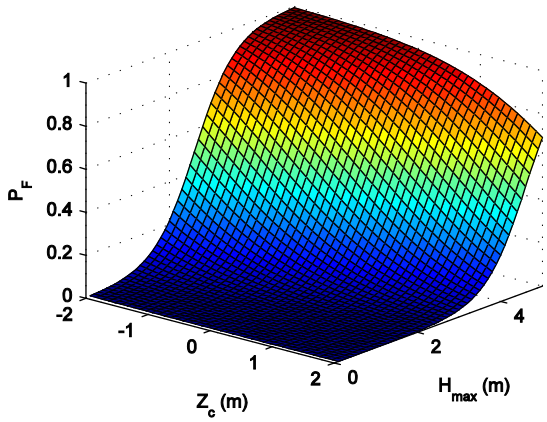

Figure 6-5. Fragility surface of the case study bridge using FSI Model methodology.

6.4. Summary

This chapter presented three distinct modeling methodologies, designated as the MCS Static Model, Dynamic Model, and FSI Model, for the reliability assessment of deck unseating mode of failure. The FSI Model is the most accurate, yet computationally intense strategy. Additionally, it requires a deep understanding of the intricacies involved in fluid-structure interaction modeling. Therefore, the MCS Static and Dynamic Models can be used instead of FSI Model for a more efficient reliability assessment of coastal bridges under hurricane events. All of these models implement quasi-Monte Carlo sampling technique to generate realizations of random variables. The results of these models reveal that deck unseating is a brittle failure mode and can be treated as a binary data of failed and survived cases for each wave and surge intensity measure combination. The application of

the developed the MCS Static Model is limited to the bridge deck unseating failure mode. However, the Dynamic and FSI Models can be used to evaluate other failure modes for retrofitted bridges as illustrated in Chapter 8 and Chapter 9.

It is possible to increase the number of Monte Carlo simulations and also realizations of hazard intensity measures to a very large number for the MCS Static Model. However, this approach is not feasible for the Dynamic and FSI Models due to the limitation on the computational power. Thus, surrogate models are required to be constructed over the result of different models. After construction, these surrogate models can provide deck unseating failure probability for the any hazard intensity measure; even if no simulation result exists. Also, the accuracy of the different structural analysis methods can be compared with each other more holistically over the large number of hazard intensity measures combinations by utilizing the developed surrogate models. Next chapter introduces appropriate surrogate models for coastal bridges reliability assessment and compare them with each other.

Chapter 7

Reliability Assessment of Coastal Bridges: Surrogate Models

In this chapter, statistical learning techniques are applied to the outcome of different structural models to develop surrogate models of bridge reliability under hurricane storm surge and wave loading and thereby derive bridge fragility surfaces. The representation of the three different structural analysis models output that have been presented in the previous chapter in a mathematical form is necessary in order to compare them together. Additionally, the developed surrogate models can be used to interpolate the probabilities of failure at any point that there is no simulation result. Different surrogate models that are appropriate for coastal bridges are presented in this chapter and their performance are compared

with each other through goodness-of-fit measures. Also, the performance and accuracy of different structural analysis methodologies are compared with each other.

7.1. Appropriate Reliability Surrogate Models for Bridge Deck Unseating

Statistical learning techniques are applied to the outcome of different structural analysis methodologies to develop surrogate models of bridge reliability under hurricane storm surge and wave loading and thereby derive bridge fragility surfaces. Although Monte Carlo simulation, as demonstrated for the MCS Static Model, offers a versatile approach for assessing the fragility, or conditional reliability, of such complex systems, the nonlinear time-varying nature of Dynamic and FSI Models renders this a computationally infeasible solution. To reduce the computational expense, surrogate models have been employed in structural reliability problems to approximate the response of structures with predictive statistical models, or to estimate the limit state function using an approximating function (Bucher and Bourgund 1990; Franchin et al. 2003; Rajashekhar and

Ellingwood 1993). For example, the structural reliability model can be presented as:

$$P_F = f(\mathbf{IM}) + e \tag{7-1}$$

where the surrogate model $f(\mathbf{IM})$ statistically predicts the reliability of the structure for a given set of intensity measures and e is the error due to the lack of fit of the surrogate model.

While surrogate modeling techniques have found recent applications for earthquake engineering (Gholizadeh and Salajegheh 2010; Seo et al. 2012), design and optimization (Gil-Martín et al. 2006; Jin et al. 2001; Simpson et al. 2001) their ability to support bridge fragility modeling under hurricane loads has yet to be considered. Typically, polynomial approximation has been employed to find the predictive models of structural behavior used in structural reliability studies; these models are known as response surfaces (Rajashekhar and Ellingwood 1993; Ren and Chen 2010). However, response surface models are generally not capable of capturing abrupt (brittle) failure modes since they provide a relationship between continuous hazard intensity measures and continuous outcome. Bridge deck unseating caused by surge and wave loading is generally characterized as such an

abrupt failure mode. Although displacement demands can be estimated for comparison to capacity limits, the behavior does not typically follow a smooth continuous form and the problem is well suited as a classification problem of "seated" and "unseated." As an alternative, logistic regression is a commonly used tool for classification of binary data (Neter et al. 1996) and has been employed in various fields for predicting the probability of failure of a system (Palei and Das 2009; Strano and Colosimo 2006). Additionally, emerging statistical learning techniques, such as support vector machines (SVMs) (Cristianini and Shawe-Taylor 2000) and random forests (Prinzie and Van den Poel 2008) are well suited for classification of categorical data. However, these tools have not been considered for the reliability assessment of structures under hurricane hazard. Given the computational complexity of bridge response assessment under surge and wave action, the above surrogate modeling techniques are compared in Section 7.2.5 for estimation of deck unseating fragility under hurricane events. Recommendations on the best surrogate modeling technique for this problem are presented on the basis of goodness-of-fit estimates.

The result of the FSI Model is first utilized with all of the proposed surrogate model techniques because it provides the most accurate output. As

mentioned earlier, since bridge deck unseating is an abrupt failure mode, typical polynomial approximations do not provide satisfactory results. Polynomial response surface models define the relationship between continuous model parameters and a continuous output. However, for brittle failure modes, a surrogate model that relates the continuous model parameters to the categorical output, or to the likelihood of occurrence of the categorical output, is required. The low performance of response surface models is confirmed for bridge deck unseating under surge and wave by testing models of various forms (e.g. linear and quadratic) which all performed relatively poorly (e.g. R^2 in the order of 0.5). Instead, this chapter focuses on testing statistical learning techniques that handle binary data effectively, comparing the classical method of logistic regression to emerging supervised statistical learning techniques, namely support vector machines (SVMs) and random forests. These three methods are nonlinear classifiers that can separate the failure responses from the survival with high accuracy. These methods have no or limited tuning parameters and are relatively easy to implement. Additionally, unlike response surface models, these classifiers do not assume the normality of the error or homoscedasticity. The case study bridge from previous chapter is used to

demonstrate the application of the statistical learning tools for evaluation of bridge reliability under wave and surge loads.

7.2. Surrogate Models Training and Validation

Part of the output result of the bridge deck unseating from FSI Model that are presented in Section 6.3 is used to train the surrogate model (training data), and the rest is used to test the performance of the trained model (validation data). In this study, 80% of the data is used for the training and the rest is used for validation. Several cross-validation techniques exist for statistical learning tools (Hastie et al. 2009). This study employs repeated random sub-sampling cross validation (Picarda and Cook 1984). In this process, the random selection of data for training and validation is repeated until the variation in the average accuracy measure is minimized (Picarda and Cook 1984).

7.2.1. Goodness-of-Fit Measures

Misclassification error is one the most common goodness-of-fit measures for classifier models. The misclassification error provides a simple measure of accuracy of the trained model; defined as the ratio of the number of incorrect classification

samples to the total number of samples in the validation data. Although this is not the definition of mean square error (MSE), for binary data, the misclassification error provides the same numeric value as MSE. Therefore, the misclassification error for SVMs and random forests models can be compared with the MSE for logistic regression model. Another metric that is widely used as a measure of goodness-of-fit in statistical learning is accuracy, which by definition is one minus misclassification error.

The confusion matrix (Hastie et al. 2009) also offers valuable insight into the performance of surrogate models as classifiers by comparing the actual versus the predicted class of data. Therefore, any off-diagonal elements represent misclassification. The confusion matrix reports the number of true positive (unseating), true negative (survival), false positive (false prediction of unseating), and false negative (false prediction of survival). Figure 7-1 shows the confusion matrix definition.

		Predicted Class	
		Survived	**Failed**
Actual Class	**Survived**	*TN* (True negative)	*FP* (False positive)
	Failed	*FN* (False negative)	*TP* (True positive)

Figure 7-1. Confusion matrix definition.

If the results are biased towards one class (for example survival), the confusion matrix is more useful than misclassification error, since it provides more details than mere proportion of incorrect guesses by suggesting the bias or tendency of the model. An additional set of measures of surrogate model performance can be derived directly from such a 2×2 confusion matrix. One of the measures is called sensitivity or true positive rate (TPR), which measures the proportion of actual positives (unseated) which are correctly identified as unseated. The false positive rate (FPR) is the proportion of survival cases that were incorrectly classified as unseated, and false negative rate (FNR) is the proportion of unseated cases that were incorrectly classified as survived. These metrics are defined as following:

$$TPR = \frac{TP}{FN + TP};\ \ FPR = \frac{FP}{TN + FP};\ \ \ FNR = \frac{FN}{FN + TP} \tag{7-2}$$

where TP is true positive, TN is true negative, FP is false positive, and FN is the false negative. Precision, P, is another measure that is defined as:

$$P = \frac{TP}{FP + TP} \tag{7-3}$$

F-measure introduced by Lewis and Gale (1994) is used here to test the accuracy of the statistical learning tools. This measure takes into account both true positive rate and precision; and is considered as a better metric for classification algorithms than accuracy:

$$F_\beta = \frac{\left(1+\beta^2\right)\times P \times TPR}{\beta^2 P + TPR} \tag{7-4}$$

where β can be any real positive value and takes into account the relative significance of TPR and P. Both P and TPR are important metrics for classification algorithms. As mentioned above, sensitivity (TPR) reveals how many of unseated cases are correctly classified, where precision shows how many of predicted unseated cases are truly unseated. Depending on the application of the surrogate model, TPR might be more important than P or vice versa. For bridge design purposes, a high value of TPR is more important than P, since conservative design is preferred. A β value more than one weights sensitivity higher than precision, where a β value of less than 1 puts more emphasis on precision than sensitivity. Unlike design, the reliability assessment should provide an unbiased representation of the vulnerability of coastal bridges. Since the goal of this research

is reliability study, F_1-*measure* (i.e., $\beta = 1$) is reported in this research for surrogate models, which gives equal significance to both precision and sensitivity.

7.2.2. Logistic Regression Surrogate Model

Logistic regression is commonly used for data classification (Neter et al. 1996) as a multivariate technique to estimate the probability that an event occurs when discrete outcomes are present. As a regression based classifier, it can be considered a classical method of statistical learning. Logistic regression is similar to the multivariate linear regression. However, it takes into account that the dependant variable, outcome of the FSI simulation, is categorical. Logistic regression can employ more than one predictor, does not require normally distributed data, and is easy to interpret (Ott and Longnecker 1993). Nonetheless, logistic regression is sensitive to outliers and should be implemented carefully when outliers present (Ott and Longnecker 1993). The general form of the logistic regression model applied to estimate the probability of failure (deck unseating) is shown below:

$$P_F = \frac{1}{1 + e^{-(\beta_0 + \beta_1 Z_c + \beta_2 H_{\max})}} \tag{7-5}$$

This form is synonymous with the concept of hurricane fragility surfaces, in which failure probability is conditioned upon hazard *IM*s. β_0, β_1, and β_2 are the regression coefficients that are obtained by maximum likelihood estimation in the logarithmic space (logit function) as shown below:

$$\ln\left(\frac{P_F}{1-P_F}\right) = \beta_0 + \beta_1 Z_c + \beta_2 H_{\max} \tag{7-6}$$

Unlike linear regression, it is not possible to find a closed-form solution for the coefficients using maximum likelihood estimation. Therefore, an iterative method is used to solve for the coefficients. The values for β_0 to β_2 for the case study bridge are 13.39, 1.79, and -4.15 respectively. As a measure of goodness-of-fit, the mean square error (MSE) for the logistic regression model is 0.09.

Another metric for goodness-of-fit is obtained through the chi-square (χ^2) hypothesis testing. χ^2-test compares the result of the null hypothesis that the bridge failure data is random, against the alternative that the data are not randomly distributed and follow the logistic regression. The result of the χ^2-test can be represented by the *p*-value. The *p*-value returns the probability of observing the null hypothesis in the data. If the *p*-value is less than a certain threshold,

typically 5%, the null hypothesis is unlikely, and thus, rejected. The p-value for χ^2 -test for the fitted logistic regression is 0.001, which is notably below typical significance levels of 5%.

Although logistic regression provides a continuous reliability assessment measure, it is possible to provide the confusion matrix for this surrogate model by introducing a threshold. The probability of failure of 0.5 is considered as the threshold limit. The confusion matrix is provided in Table 7-1. This confusion matrix reveals a good accuracy (0.92). The goodness-of-fit measures for this surrogate model are reported in Table 7-1 and are compared with the other classification models.

7.2.3. Support Vector Machines Surrogate Model

Support vector machines (SVMs) are classification algorithms first proposed by Cortes and Vapnik (1995), which are applied for bridge reliability prediction because of their exceptional performance for classification of binary data (Hastie et al. 2009). The SVM constructs a hyperplane in a multi-dimensional space with dimension equal to the number of model parameters —two in the case of $H_{\max}$ and Z_c— that can be used to demarcate the bridge as failed or survived. SVMs can

perform both linear and nonlinear classification by using different kernel functions which transform the binary data into a mapped space (feature space). In the case that the bridge unseating data does not have a simple linear hyperplane as a classification criterion, alternative kernel functions are considered such that the analysis results will have a hyperplane in the feature space, which is nonlinear in the original space. Linear, quadratic and cubic polynomials, as well as Guassian radial basis functions (RBFs) are the kernel functions used in this study to classify seated and unseated bridges. The Gaussian RBF (Buhmann 2003) constructs the inner product of two vectors support vectors in the feature space by using the Gaussian function.

As shown in Table 7-1, for the SVM with a linear kernel function, the average misclassification error is equal to 0.12. The performance of the SVM surrogate model improves by using nonlinear kernels such as higher order polynomials or Gaussian radial basis functions. RBF kernel is advantageous since the RBF kernel has fewer numerical difficulties (Hsu et al. 2010) since it is bounded, while polynomial kernels may provide values that go to infinity (Hsu et al. 2010). As the results suggest, the best model is obtained by using the Gaussian radial basis kernel function, which provides a misclassification error of 0.08.

Therefore, the SVM with radial basis kernel function provides the best performance for classification of bridge deck unseating failure mode.

The confusion matrix for the SVM with Gaussian RBF kernel is reported in Table 7-2 which shows a good accuracy. The goodness-of-fit measures for the SVM are provided in Table 7-1. Also, the value of *FP* is larger than *FN*, which means that the trained SVM is conservative for structural reliability prediction; i.e., more bridges are misclassified as unseated rather than survived.

7.2.4. Random Forests Surrogate Model

For the third classifier, random forests are tested as a surrogate model of bridge reliability because of their high performance in classification of categorical data (Hastie et al. 2009). The algorithm that was originally developed by Breiman (2001) is implemented in this study. Random forests are easy to train and implement. In contrast to the previous methods, random forests are not sensitive to outliers. For bridge deck unseating classification, random forests utilize a large number of uncorrelated trees, referred to as decision trees, to classify the categorical data based on the model parameters. Each decision tree tests the input model parameters, i.e., Z_c and $H_{\max}$, and predicts the bridge deck failure. For

instance, one decision tree can be trained to learn that if the value of wave height is more than 3m and relative surge elevation is less than -1m, then the class is failed according to the FSI output. Therefore, unlike SVMs, each decision tree is easy to interpret. The trained random forests model *decides* the bridge failure class for the given model parameters based on the majority vote:

$$P_F = \text{majority vote } \left\{ P_n \left(Z_c, H_{\max} \right) \right\}_1^{N_T} \tag{7-7}$$

where P_n is the casted vote for the n^{th} tree and N_T is the total number of trees. Total number of 500 trees is used for the random forests model. For this surrogate model, the misclassification error is equal to 0.04. This misclassification error demonstrates a significant improvement for bridge deck unseating classification. The goodness-of-fit measures for the random forests surrogate model are presented and compared with other surrogate models in Table 7-1. It can be observed that all the goodness-of-fit measures support the superiority of the random forests model, as discussed in the next subsection.

7.2.5. Comparison of the Surrogate Models

Table 7-1 summarizes the surrogate models and their goodness-of-fit. Additionally, Table 7-2 provides the confusion matrices for the proposed surrogate models. The

trained logistic regression, SVM with RBF kernel, and random forests provide acceptable classification since the misclassification error for all of them is less than 10%. The goodness-of-fit values indicate reasonable classifications with a good true positive rate and low false positive and false negative rates. As mentioned before, the misclassification of bridge reliability is conservative for all the surrogate models (i.e., survival misclassified as failed or unseated). In order to provide a visual comparison, Figure 7-2 plots the 256 categorical output data from the FSI simulations versus logistic regression, SVM with RBF kernel, and random forests models. The high accuracy of the three surrogate models can be seen in this figure. The developed surrogate models provide a high precision and sensitivity, as it can be seen by F_1-*measure* of more than 0.87 for all of them. The superiority of random forests over the other techniques can also be observed in this figure, as it has the misclassification of 0.04.

Table 7-1. Summary of the predictive models and their corresponding goodness of fit.

Predictive model		**Misclassification or MSE**	***TPR***	***FPR***	***FNR***	$\boldsymbol{F_1}$
Logistic regression		0.09	0.88	0.06	0.06	0.87
SVM	Linear	0.12	0.84	0.12	0.11	0.71
	Quadratic	0.12	0.86	0.10	0.09	0.78
	Cubic	0.10	0.89	0.07	0.06	0.87
	RBF	0.08	0.93	0.06	0.06	0.91
Random Forests		0.04	0.98	0.01	0.01	0.98

Table 7-2. Confusion matrices for logistic regression, SVM with RBF kernel, and random forests models.

		Logistic regression		SVM with RBF kernel		Random forests	
		Predicted class		Predicted class		Predicted class	
Actual class		Survived	Failed	Survived	Failed	Survived	Failed
	Survived	162	11	163	10	176	2
	Failed	10	73	5	78	1	77

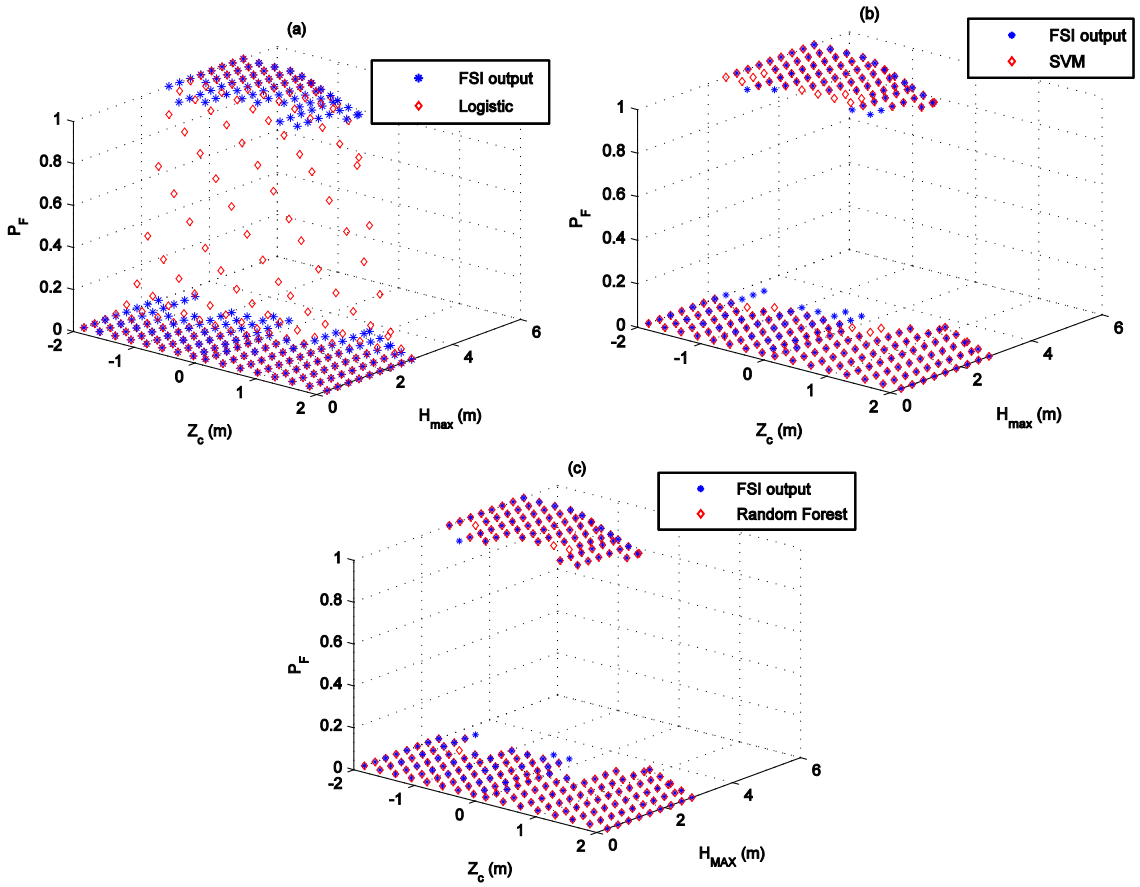

Figure 7-2. Comparison of different surrogate models for fragility assessment of deck unseating: (a) logistic regression; (b) support vector machine (SVM) with RBF kernel function; and (c) random forests.

7.3. Comparison of Static, Dynamic, and FSI Model Methodologies

Previous section defines the most appropriate surrogate models for bridge deck unseating classification. The results from the FSI Model methodology were implemented to develop these surrogate models. However, the efficiency of fragility analysis can be further improved by using more simplified structural analysis models, as long as it is capable of capturing the failure mode of interest. Fluid-structure interaction models such as the one presented in Section 4.2 have the advantage of accurate estimation of the bridge behavior and providing insight on the response of the bridge but they are computationally intense as noted in Section 6.3.

Therefore, this section constructs reliability surrogate models on the output of the MCS Static and Dynamic Models, and compares them with the reliability surrogate model constructed from the FSI Model. The same case study bridge model with the same experimental design and approach presented in Section 6.3 is utilized here; however, the output data used to derive the surrogate model is based upon Dynamic Model of the bridge structure with the Modified AASHTO loads

and the Static Model. The full set of random variables for this simulation is presented in Appendix V.

Two random forests are trained over the results of the MCS Static Model output and Dynamic Model output, respectively. The resultant random forests are designated as S-RF and D-RF, respectively. Since all random forests algorithms are already constructed based on the training data, predicted failure probabilities can be directly estimated for any $H_{\max}$ and Z_c. A sample size of 10,000 points over the hazard intensity measures is generated and used to identify the misclassification error for the other models versus FSI. The trained random forests are compared with the FSI-RF in Figure 7-3. The S-RF and D-RF are in agreement with the FSI-RF. The misclassification errors for these two random forests with respect to FSI-RF are 0.19 and 0.13, respectively. Since the random forests surrogate model has high accuracy (the surrogate model error is around 0.01), the misclassification error is due to the reduction in the structural analysis and load modeling accuracy from the FSI Model to the Dynamic and Static Models. Confusion matrices are shown in Table 7-3. As it can be concluded, the results of the MCS Static and Dynamic Models are conservative; (i.e., more false negatives are reported than false positives). Therefore, these models can be utilized for a fast screening of the

susceptible bridges structures under hurricane events. The F_1-measures for the S-RF and D-RF models compared to FSI-RF are 0.65 and 0.75 respectively. This result shows that the higher accuracy is achieved by using more advanced models. However, fast screening of vulnerable coastal bridges, especially for real time application, is more practical with the MCS Static and Dynamic Models.

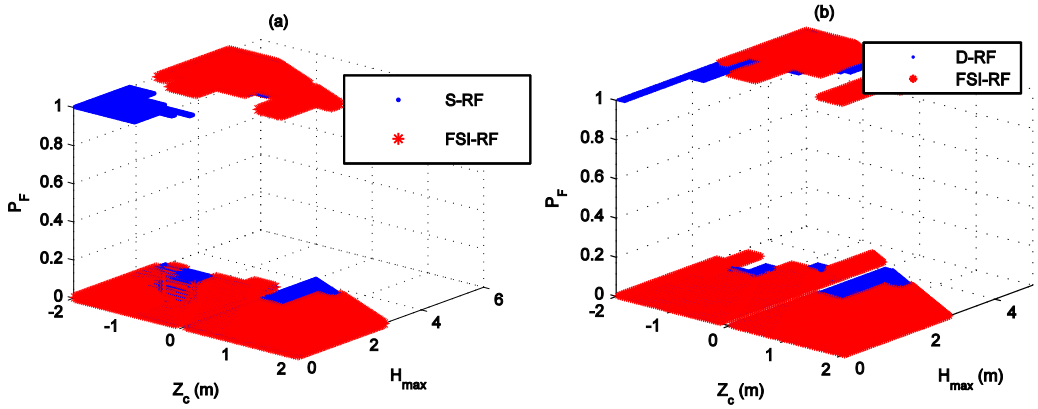

Figure 7-3. Comparison of two random forests models trained over different analysis output data: (a) FSI Model versus Static Model; (b) FSI Model versus Dynamic Model.

Table 7-3. Confusion matrices for three random forests models trained over FSI, Static and Dynamic Models output.

		Predicted class (Static)		Predicted class (Dynamic)	
		Survived	Failed	Survived	Failed
Actual class (FSI)	Survived	6484	1599	7119	964
	Failed	398	1519	197	1720

7.4. Summary

This chapter and Chapter 6 present the core contribution of this research for the development of fragility models for coastal bridges subjected to hurricane induced wave and surge loads. The results of the structural analysis models presented in Chapter 5 reveal that deck unseating is a brittle failure mode. Therefore, the output becomes a categorical data; i.e., failed (unseated) or survived (seated). A continuous model over the entire range of hazard intensity measures is required to be constructed on this categorical data that can provide failure probabilities for any realization of hazard parameter (that may not be simulated). Surrogate models that relate continuous input to categorical output are required. Therefore traditional response surface models are not appropriate. Three statistical learning methods —logistic regression, support vector machines, and random forests— are applied to the result of the analysis of bridge deck unseating. These methods are nonlinear classifiers that can provide high accuracy classification for binary data. Logistic regression, support vector machines with the Gaussian radial basis function kernel, and random forests provide a high quality approximation of the bridge deck unseating failure mode. Nonetheless, the performance of the random forests is found to be superior for classification of the bridge deck unseating.

Random forests surrogate models are trained over the results of Static, Dynamic, and FSI Models and compared to each other, where the output of FSI Model is considered as the most accurate and the basis for comparison. The result of the Dynamic Model is in good agreement with the FSI Model, and therefore, can be used for a more computationally efficient reliability assessment. The error increases as the modeling accuracy decreases; i.e., Static Model has higher error than Dynamic Model. However, the Static Model can provide an effective means to rapidly screen a large bridge inventory as will be demonstrated in Chapter 9.

Chapter 8

Retrofit Measures for Coastal Bridges and Definition of New Capacity Limit State Functions

This chapter introduces potential retrofit measures for coastal bridges to prevent the deck unseating failure mode. Providing strong connections between the bridge super- and substructure is one of the recommended methods for retrofitting coastal bridges (Padgett et al. 2008; Padgett et al. 2009; Sawyer 2008). Other retrofit measures, such as shear keys and restrainer cables that traditionally have been used for seismic hazard mitigation of highway bridges, can also be used for coastal bridges to prevent deck unseating. All of these measures can potentially transfer large forces from the bridge deck to substructure. Therefore, the capacity limit

state is not simply a deck displacement value, as considered in the fragility analysis in prior chapters of this dissertation. The transferred forces may introduce damages to the substructure which have not been explored in past research. This chapter introduces the potential retrofit measures to prevent deck unseating failure mode. Also, new capacity limit state functions for retrofitted bridges are defined. Chapter 9 will apply the approach to derive capacity limit state functions to evaluate the viability of the prospective retrofits to improve the reliability of coastal bridges in the Houston/Galveston area inventory.

8.1. Retrofit Measures for Coastal Bridges

Increasing the bridge deck elevation is one of the proposed methods for retrofitting or design of new bridges. However, this option is more applicable for the design of the new water crossing bridges. Okeil and Cai (2008) suggest that the best solution to prevent extensive damages to coastal bridges is to build the new structures above the highest storm surge level. The damaged I-10 Twin Span Bridge over Lake Pontchartrain has been replaced with a higher elevation bridge. Figure 8-1 shows the damaged bridge after Hurricane Katrina and the newly constructed

bridge. The new Twin Span has a clearance of more than 9m, where the old bridge clearance was only 3m (DOTD 2010).

Figure 8-1. (a) The damaged I-10 Twin Span Bridge over Lake Pontchartrain. More than 300 westbound spans and 170 eastbound spans were shifted or unseated during Hurricane Katrina. (b) The new high elevation Twin Span Bridge (DOTD 2010).

Another method for retrofitting is to implement high strength connections between the bridge super- and substructure. The US-11 Bridge crossing Lake Pontchartrain was an integral cast in place structure. This bridge is located in the proximity of the I-10 Twin Span Bridge. However, US-11 Bridge sustained minimal non-structural damages to the guardrails. Figure 8-2 shows the US-11 Bridge after Hurricane Katrina.

Figure 8-2. US-11 Bridge over Lake Pontchartrain. This bridge is located in the proximity of I-10 Twin Span. However, unlike I-10 Twin Span, it sustained almost no damage during Hurricane Katrina due to the integral structure (NIST 2006).

Addition of shear keys to prevent transverse displacement of the bridge deck is another method for retrofitting. The coastal bridges with shear keys during Hurricane Katrina sustained no or minimal damages (Mosqueda et al. 2007; Padgett et al. 2008). An example is Norfolk Southern Railroad Bridge which is also located over Lake Pontchartrain close to the I-10 Twin Span. The railroad tracks were stripped from the bridge during Hurricane Katrina; nevertheless, the structure remained intact. Another bridge with shear keys that survived Hurricane Katrina is CSX Railroad Bridge over Biloxi Bay. This bridge did not sustain any damage during Katrina landfall. However, US-90 Bridge over Biloxi Bay, which is located in the same area, was heavily damaged and the majority of its spans were

unseated. Figure 8-3 shows Norfolk Southern Railroad Bridge and CSX Railroad Bridge.

Figure 8-3. (a) Norfolk Southern Railroad Bridge over Lake Pontchartrain lost its railroad tracks during Hurricane Katrina. (b) CSX Railroad Bridge over Biloxi Bay remained intact after Hurricane Katrina (NIST 2006).

Restrainer cables that are traditionally implemented for seismic hazard mitigation can also be used for retrofitting of coastal bridges. Figure 8-4 shows the application of high strength steel restrainer cables in central and southern US area. These cables are used in the seismically active regions to prevent deck unseating. Cables are typically anchored to the girders and wrap around the bent beam. Another configuration is to connect to adjacent spans to each other. These cables are typically implemented to prevent the longitudinal motion of the bridge deck. However, in this study, they are implemented to prevent the transverse movement of the deck.

Figure 8-4. High strength steel restrainer cables to prevent deck unseating.

High strength connections between the deck and its support, shear keys, and restrainer cables are investigated in this research as potential retrofit measures to mitigation the probability of deck unseating. All these retrofit measures can transfer large forces from the superstructure to substructure that potentially leads to different damage states and failure modes. Therefore a fragility analysis for retrofitted bridges should consider alternative failure modes and the structural capacity of additional components besides those that simply restrain the deck.

8.2. New Capacity Limit State Functions

Other modes of failure besides unseating are possible for bridges with strong connections between the bridge deck and bent beam as provided by several of the

retrofit measures described. Large forces can transfer from the super- to substructure by implementing strong connections, potentially resulting in permanent damage to costly substructure components and impairing the functionality of the bridge. For reliability analysis of this type of structure, a quantitative definition of capacity limit states is essential to consider alternative modes of failure beyond simply the deck unseating failure mode. The definition of limit states at the system level is not trivial, particularly since the response of more than one component may contribute to the global performance or failure mode.

In past reliability assessments of bridges under different loading types, component damage states were defined based on anticipated physical and/or visible damage (FEMA 2003; Nielson and DesRoches 2007; Padgett 2007) and system level damage expressed in terms of anticipated closure, repair time, repair cost, or qualitative descriptions of joint component damage (Nielson and DesRoches 2007; Padgett 2007; Padgett and Desroches 2007). While several of these methods provide a valuable link between practice and theory, they often require subjective mapping between component and system performance given the likelihood of insufficient empirical data to inform such mapping (e.g. bridge component damages that lead to system closure). Furthermore the outcomes may

be region specific due to the variation in owner experience, construction practices, material and labor availability, stakeholder risk preferences, among others. An alternative approach to define system level performance can be classified as "prescriptive," where global limit states are defined on the basis of the physical ability of the structure to serve its purpose (e.g. carry load). These performance outcomes can be used in subsequent consequence modeling and decision support, such as closure decisions or retrofit assessment based on structural safety. While drift limits have been widely prescribed for buildings under lateral loads that correspond to global performance objectives [see e.g. (ATC-40 1997; FEMA 1997)], analogous models are lacking for bridges, particularly considering failure modes anticipated for bridges under surge and wave loads with a range of connection types.

This section presents an approach for probabilistic capacity assessment of bridge systems, in which global performance measures that have a direct impact on post-event functionality, such as system strength and stiffness loss, are related to local damages induced by hazard loading. Such a method is required for reliability assessment of the retrofitted coastal bridges that can suffer from multi-components damages. To overcome traditional limitations of scarce empirical data or subjective

mapping of component to system damage state definitions adopted in bridge system reliability assessment, nonlinear dynamic analyses are exploited to enable statistical analysis of system behavior as a function of joint component demands for use in a global performance assessment. The systematic methodology defines limit state capacities and their associated uncertainty in achieving system level performance objectives, thereby enabling reliability analysis of retrofitted coastal bridges subjected to hurricane events. Nevertheless, the proposed method is general and can be applied to various structural systems subjected to a range of extreme events, thereby addressing a current gap in bridge system reliability assessment regarding the mapping of local responses to global system performance under natural hazards.

The following subsections detail the general methodology for assessing bridge system limit state capacities, the approach adopted to simulate bridge response under hurricane induced loads, and the application of the proposed approach for case study bridges. Results of the case study provide insight for future applications regarding illustration of the proposed method for global performance assessment, viable model form for the capacity estimation, the role of uncertainty

treatment, and significant local demand quantities of interest for bridge system reliability assessment under hurricane induced surge and wave.

8.2.1. Methodology for the Assessment of Limit State Capacities

As a first step toward assessing quantitative capacity limit states that correspond to global structural performance, global damage states are defined based on the post event load-deformation response of the structural system. The primary function of a structure is to maintain its serviceability by sustaining its strength, stiffness and integrity under imposed loads. Any considerable alteration in the structural strength or stiffness can be noted as a "damage state," since the structure is diverging from its original status, and partially or completely losing its design functionality (Holmes 2000). This global change of strength and stiffness can also be related to other metrics such as casualty, downtime or repair cost (Holmes 2000), although this is not a trivial task. Given the key role of a bridge in carrying traffic loads, one damage state can be defined based on the degradation of vertical load carrying capacity. Reduction in the lateral stiffness or load carrying capacity also endangers the structure by reducing its capability to sustain future events that impose lateral loads, and possibly jeopardize the stability by increasing the second order effects on compressive components. Hence, damage states herein are defined

based on loss of vertical or lateral load carrying capacity, and reduction of lateral stiffness.

Table 8-1. Definition of the global damage states.

Global performance measure	**Global damage state, *DS***	**Prescriptive limit for *DS***	**Capacity function***
Change in stiffness (δK)	Major (DS_1)	$lim_1 = 0.4$	$\delta K = f_1(EDP_1, EDP_2, ..., EDP_n) + e_1$
Change in lateral strength (δR_H)	Extensive (DS_2)	$lim_2 = 0.15$	$\delta R_H = f_2(EDP_1, EDP_2, ..., EDP_n) + e_2$
Change in vertical strength (δR_V)	Extensive (DS_3)	$lim_3 = 0.15$	$\delta R_V = f_3(EDP_1, EDP_2, ..., EDP_n) + e_3$
Collapse	Collapse (DS_4)	--	--

* EDP: Engineering Demand Parameter

The global damage states are identified by comparing the load-deflection behavior of the intact and damaged structure, performing pushover and pushdown analyses. Different levels of reduction in the stiffness and strength capacity may delineate different damage states. Table 8-1 summarizes the global damage state definitions adopted in this research. However, it is acknowledged that different prescriptive limits may be deemed critical, and the approach proposed herein can be adopted to derive the corresponding limit state capacity functions. In this study, a reduction of 40% in the stiffness (δK) is considered as the major damage state, indicating significant change in the structure. The change in structural stiffness has been used in building reliability assessment as a performance metric

that indicates structural damage (Ellingwood and Kinali 2010; Frangopol et al. 2007). Additionally, this level of stiffness reduction is adopted since it may result in initiation of yielding of abutments and columns reinforcements in the case study bridge, which may require repair. Furthermore, for the case study bridge evaluated, a 40% reduction in stiffness occurs prior to significant reduction in strength, which is considered at the extensive damage state. Structural performance can also be measured by overall strength. Mackie and Stojadinović (2005) suggested that, on average, 10% to 20% reduction in lateral and vertical load carrying capacity may result in 50% to 75% reduction in traffic capacity. Therefore, a reduction of 15% in the maximum vertical or horizontal load carrying capacity (δR_V or δR_H) of the structure is considered extensive damage herein. This level of strength reduction corresponds to significant damage to the structural components, degradation of materials strength, and the potential for a significant reduction in functionality or traffic capacity of the bridge. Furthermore, for the case study bridge configurations analyzed, beyond a 15% to 20% reduction in strength the structure experiences a rapid decrease in strength leading to structural instability.

The global damage state definitions can be used in a reliability assessment of bridge failure conditioned on hazard intensity measures (**IM**), as shown below:

$$\mathrm{P}\left[DS_j \mid \mathbf{IM} \right] = \mathrm{P}\left[\delta G_k = f_j\left(\mathbf{EDP}(\mathbf{IM})\right) + e_j \geq lim_j \right] \tag{8-1}$$

where G_j is the global performance measure (stiffness, force, etc.), defined as a function, $f_j(\bullet)$, of engineering demand parameters, *EDP*s; lim_j, is the prescribed limit for the global measure used to define the j^{th} damage state, DS_j. The term e_j includes model error and uncertainty introduced by propagating structural random variables. In theory, one can directly assess the limit state probability by performing Monte Carlo simulation, or other simulation based strategies, where the results of the global pushover before and after the extreme event are compared for each simulation. However, such strategies are computationally expensive to achieve a statistically significant number of samples, particularly across the full *IM* space. Instead, mathematical models may be estimated for the decoupled demand and capacity (e.g. **EDP** and lim_j respectively), mitigating the need for additional nonlinear dynamic analyses and enabling structural reliability analysis through a range of numerical or analytical approaches. In addition to its efficiency and insights gained into the performance assessment, such decoupling of demand and capacity models can also further support performance based design or retrofit. This section provides an approach to assess the governing equations for limit state capacities and associated uncertainty (i.e., the $f_j(\bullet)$ and e_j) that correspond to

global performance metrics; the method is applied to a retrofitted case study bridge with four different configurations.

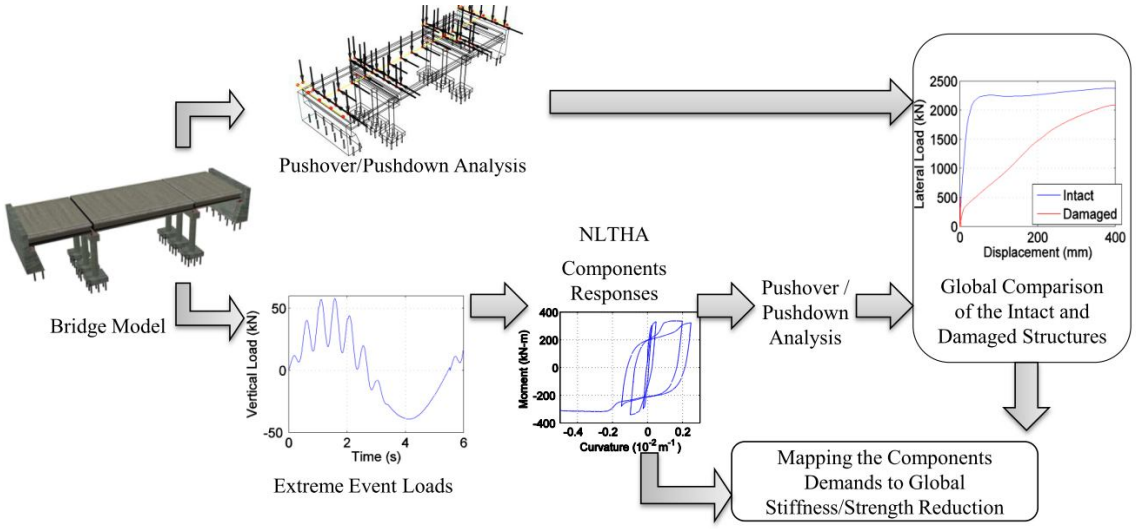

Figure 8-5. Procedure to define the limit state capacities by comparing the global force-deformation behavior of the structure before and after the extreme event. Pushover and pushdown patterns are schematically presented in the figure. Note that they are applied separately. (NLTHA: nonlinear time history analysis.)

The proposed procedure for defining limit state capacities is schematically shown in Figure 8-5. First, a separate pushover and pushdown analysis of the intact bridge is conducted to characterize the original global performance. The load pattern consists of a uniformly distributed load over the bridge deck in the vertical and transverse directions for pushdown and pushover analysis, respectively. This load pattern is consistent with the primary point of application of peak surge and wave loads on the bridge and induces a similar mode shape to that excited by

typical hurricane induced loads. Then the bridge models are subjected to a suite of extreme event loads (i.e. surge and wave load time histories) via nonlinear dynamic analysis and responses of key components are monitored. After each extreme event scenario, the stiffness and strength of the damaged structure is obtained, and the result is compared with the original pushover curve of the intact structure. Through this procedure, the different limits prescribed, such as 40% reduction of stiffness, are mapped to the peak structural demands experienced by different components including uncertainty quantification through a statistical analysis of the response data. This mapping provides limit state capacity models in which global performance is expressed as a function of local response quantities as shown below:

$$\begin{aligned} &\delta G_j = f_j(EDP_C, EDP_A, EDP_P, ...) \\ &\Rightarrow DS_j \equiv \left[\mathrm{f}_j(EDP_C, EDP_A, EDP_P, ...) + e_j \geq lim_j \right] \end{aligned} \tag{8-2}$$

where $f_j(\bullet)$s are functions that relate the extreme event engineering demand parameters of columns (EDP_C), abutments (EDP_A), piles (EDP_P), and other components to the global stiffness and strength degradation. The limit state capacities, as a combination of demands of different components, are then defined by setting $f_j(\bullet)$ equal to the prescribed value of stiffness and strength reduction at

the global level. These models therefore provide a functional form of the global limit state capacities that can be used for the reliability assessment through integration with probabilistic demand models.

As an additional advantage, characterizing the limit state capacity function as presented in Equation (8-2) avoids the need to make assumptions of component to system logical assembly. The general form of system reliability, without any assumption on the system level assembly, is presented in Lupoi et al. (2004). However, for practical applications, simplifications are typically introduced at the system level. For example, previous studies range from either evaluating the system level performance on the basis of a single vulnerable component (Karim and Yamazaki 2001; Lee et al. 2010); to assessing the reliability of the system through a combination of component failures, often abstracted as series (Nielson 2005; Padgett and Desroches 2007). Acknowledging the correlation in between components demands, series assumption provides an upper bound for system failure probability (Pan et al. 2007). Also, such conceptualizations are most effective when the components have binary stages, for example failed or not, or discrete failure states, and hence, the system can be represented as a Boolean combination of its individual components. This Boolean representation is less

appealing for intermediate physical states of many structures (e.g. stiffness loss) since distinction between the failed and non-failed states of components may not uniquely map to global performance limits. The system can reach the given global damage state by infinite different combinations of demands on components. However, application of Equation (8-2) eliminates the uncertainties associated with system level assembly, since it is constructed as a representation of the physical combination of components that lead to loss of system performance. Moreover, Equation (7-2) is not conditioned on hazard parameters, and may be used for other types of hazards with similar load patterns that induce like modes of response.

It should be noted that the global limit states might not be appropriate for large structures, structures that are considerably unsymmetrical, and when the effect of phase lag is significant. Local failures and partial collapses are likely in these structures, without a major strength/stiffness reduction at global level. Therefore, these conditions might require a separate definition of damage at the structural subassembly level. However, the procedure described in Figure 8-5 may be adapted for each structural subassembly. The models adopted in the following sections exploit the symmetry of the structure and the equality of wave loads on bridge spans. For long structures, the spatial distribution of the wave is not equal

across the entire length of the structure; hence the effect of each component (i.e. columns of the first bent, second bent, left abutment, right abutment, etc.) should be investigated separately.

8.2.2. Retrofitted Case Study Bridges

For the case study, the most typical water crossing bridge structure of the greater Houston area is selected: a three span simply supported box beam bridge. The overall geometry is consistent for the examples, and is depicted in Figure 8-6. The deck width is 10.7m and all of the spans have a length of 12.2m. The deck thickness is 0.16m and the girders' height is 0.38m. The outermost spans of the bridge are supported by seat-type abutments with twelve piles having 0.4m diameter and a length of 10m. The substructure consists of two bent caps, each supported by three 5.2m tall circular columns of 0.91m diameter. The column reinforcement includes twelve 28mm longitudinal bars and spiral transverse reinforcement with a pitch of 0.25m. Each column is supported by a square foundation with 2.6m×2.6m dimension. The pile cap is supported by eight piles of 0.4m diameter and a length of 14m, except for the model that investigates the effect of pile uplift.

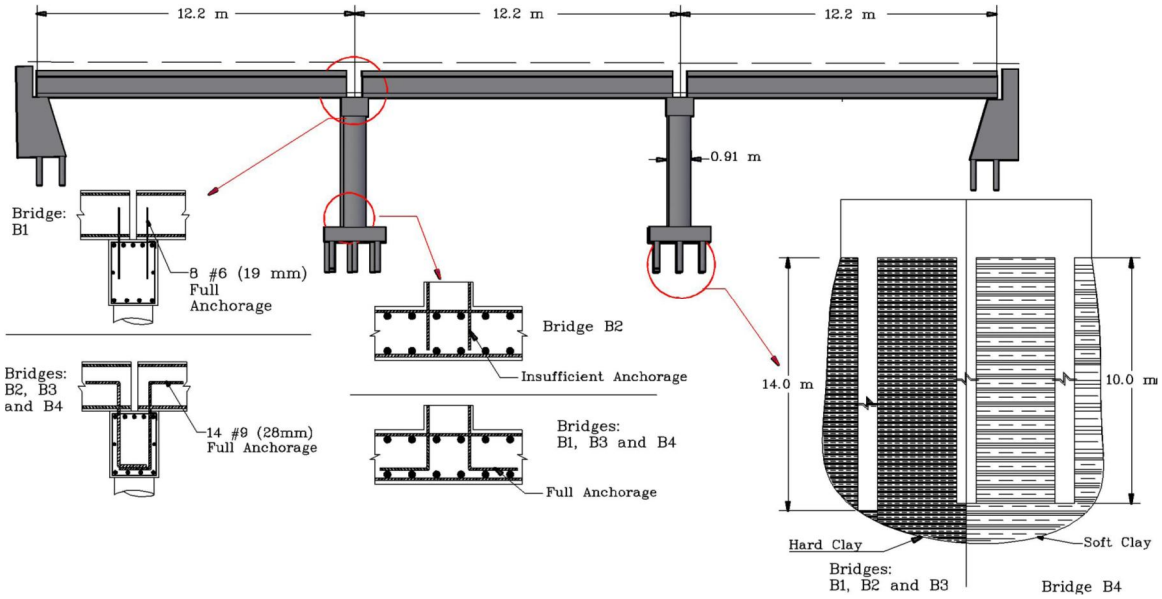

Figure 8-6. Case study bridge configurations.

The bridge is retrofitted by using different connections between the super- and substructure. Also, the effect of columns' foundation connection is investigated. Three different connection configurations for the retrofitted case study bridge are considered in this research, as shown in Figure 8-6. The first bridge model designated as B1 contains super-to-substructure connections consisting of eight dowels of 19mm diameter at each side of the span with full embedment length; hence, the dowels yield and fracture is the governing mode of failure of the connection dowels. The summation of fracture forces of all of these dowels is equal to 1860kN. The effect of connection strength at the foundation level is investigated by assigning low strength properties to the column-to-pile cap

connections, referred to as bridge B2. The median pullout capacity of the reinforcement for B2 is 1260kN. For the next two case study bridges, the strength of super-to-substructure and column-to-pile cap connections exceed the capacity of the structural components and are sufficient to transfer the deck loads to the foundations. Two different pile foundations are assumed for the case study bridge. The bridge models B1 to B3 share the pile foundation properties that were introduced earlier, located at hard clay with median undrained cohesion strength of 100kPa. The last bridge model, designated as B4, has foundations supported by eight piles of the length of 10m. This bridge is located on relatively soft clay with median undrained cohesion strength of 30kPa. These two undrained shear strengths render foundation uplift capacities of 7130kN and 1610kN respectively. The pushover curve of bridges B3 and B4 is shown in Figure 8-7.

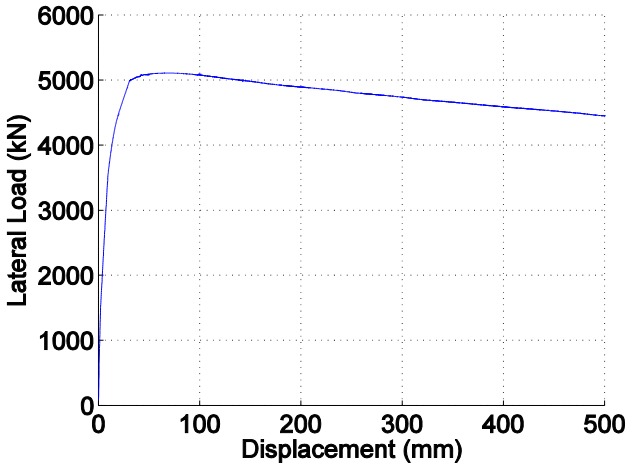

Figure 8-7. Pushover curve of case study bridges B3 and B4.

8.2.3. Hazard Combinations for Numerical Simulations

Uncertainty in material strength, density and structural properties is considered in the development of probabilistic capacity models according to Table 5-8. Randomness in wave and surge parameters is captured according to Table 5-2. Ten different wave heights from the range of 0.3m to 3m, and ten different relative surge elevations, from the range of -3m to 2.4m were selected for the analysis. The maximum value of wave height is governed by water depth. Loading cycles were considered blocking parameters and set equal to either one or two. However, higher numbers of loading cycles have been examined to verify the independence of the global limit state capacities from the number of loading cycles. In order to produce larger demands on the structure an artificial increase of the magnitude of wave loads were included as another loading variable. This scaling factor was selected equal to either one or two. Given that there are two wave and surge parameters, each with ten levels, two different numbers of load cycles, and two different values for scaling of wave load magnitude, a full factorial design leads to 400 simulations. Different configurations of the case study bridge are simulated under each combination using nonlinear dynamic analysis with the Newmark method for time

marching as described in Section 4.1. Subsequently, the pushover/pushdown is performed using a displacement control approach.

The results for B1 and B2 are only briefly discussed here, since the simulation results show a negligible change at global level performance metrics associated with the failure modes of these bridges before collapse. For B1, the substructure remains elastic until deck unseating, which is considered as one of the collapse modes. Intermediate levels of damage could be defined based on the residual deck displacement prior to unseating, although this is not considered as a part of the case study given the system damage state definitions formerly presented. For B2, the analysis under increased hazard intensity reveals failure at the column base by pullout of the rebar and instability of the structure. Hence, the governing component is either the pile cap to column or piles to pile cap connection. No intermediate damage state is considered herein for this case as it reflects a relatively brittle failure mode. The results for bridges B3 and B4 are discussed in depth in the following subsections, as these configurations exhibit intermediate global damage.

8.2.4. Stiffness Degradation

For bridge B3 retrofitted with high-strength connections, sufficient connections exist to transfer deck loads to the substructure and stiffness degradation occurs due to column degradation or yielding of abutments. Following the method outlined in Section 8.2.1, a model is developed to relate the global stiffness degradation to component response quantities, specifically column and abutment demands in the case of B3. The foundations mechanical properties for B3 are sufficiently large to not yield before columns failure. The stiffness degradation (as well as strength degradation) reduces more significantly at higher lateral displacement, attributed to the geometric nonlinearity and second order effects. The results of the 400 simulations were divided into two model regions based on the global response exhibited for bridge B3. The governing DS_1 capacity function was derived from the 283 simulations in the region of less than 60% reduction in lateral stiffness. A different form of regression model is required for higher levels of stiffness reduction. Linear, quadratic and power models were tested as potential regression models. Independent variables considered include peak abutment displacement and various column demand parameters.

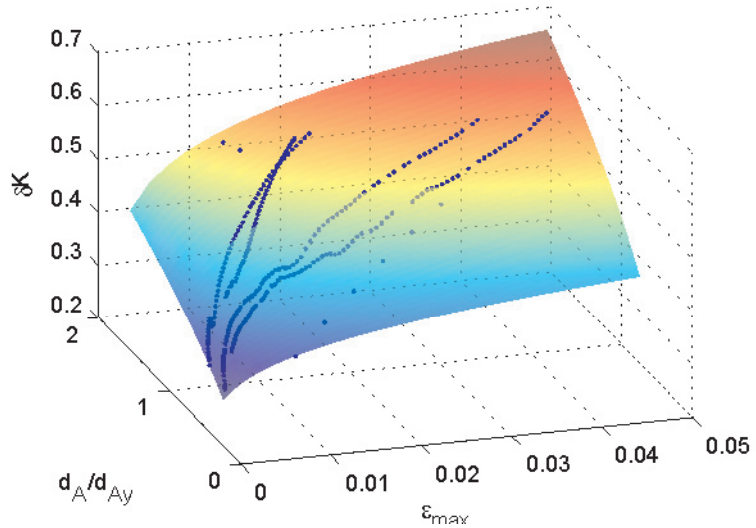

Figure 8-8. Lateral stiffness reduction versus peak maximum axial strain and peak maximum abutment displacement ratio. Lateral stiffness degrades with either increase in maximum strain or abutment displacement.

Figure 8-8 plots the results of the simulations and the regression model adopted. As this figure shows, lateral stiffness degrades with either increase in maximum axial strain or abutment displacement. Equation (8-3) provides the form of the model for the region of interest (i.e., δK <0.6):

$$\delta K = 0.842\varepsilon_{\max}^{0.150}(d_A / d_{Ay})^{0.421} \tag{8-3}$$

where d_A is the peak lateral displacement of abutment, d_{Ay} is the yield displacement of abutment, and $\varepsilon_{\max}$ the maximum axial strain of the columns. The coefficients of the model are specific to the bridge B3 analyzed herein and represent a characteristic equation for the structure, although this model form is appropriate

for other high capacity connection bridges susceptible to stiffness degradation. The R^2 of the proposed model for B3 is 0.884. It is noted that the peak total displacement ratio, defined as the ratio of total elongation of column over its length, provides a similar goodness of fit and may also be a valid demand parameter for DS_1. Furthermore, the definition of DS_1 adopted herein is shown as at least 40% reduction of stiffness in Equation (8-3):

$$DS_1 \equiv [0.842\varepsilon_{\max}^{0.150}(d_A / d_{Ay})^{0.421} \geq 0.4] \tag{8-4}$$

This model characterizes the onset of major damage, i.e. δK of 40%, and provides a median value of the capacity limit state for DS_1. From the simulations, the uncertainty in the capacity limit for DS_1 is characterized by finding the associated probability distribution. Additional simulations are conducted to increase the confidence in distribution testing and uncertainty quantification. Six sets of additional 300 simulations, each with constant hazard parameters, were performed, varying the structural properties according to the probability distributions that are presented in Table 5-8, in order to find the probability distribution of $\varepsilon_{\max}$ and d_A/d_{Ay} at the prescribed global limit. The capacity model for stiffness reduction can be characterized by a joint lognormal distribution of

$\varepsilon_{\max}$ and d_A/d_{Ay}, and the homoscedasticity assumption is found to be reasonably valid across the full range of parameters considered with a peak change in dispersion of 12%. At the prescribed limit of 40% stiffness reduction, the simulation results reveal marginal lognormal distributions of $\varepsilon_{\max}$ and d_A/d_{Ay} with the overall logarithmic standard deviations of 0.20 and 0.31, respectively. The dispersions from the regression model are 0.17 and 0.26 for $\varepsilon_{\max}$ and d_A/d_{Ay}, respectively. The dispersions introduced by the structural random variables exclusively are 0.19 and 0.29 for $\varepsilon_{\max}$ and d_A/d_{Ay} respectively. The correlation between $\varepsilon_{\max}$ and d_A/d_{Ay} is found to be reasonably consistent across the parameter space, with an average correlation coefficient in the logarithmic space of 0.724. Therefore, $\ln(\delta K)$ is a sum of two correlated normal random variables and has a bivariate normal distribution with *cov* of 0.144. If other prescriptive limits of stiffness reduction are of interest, Equation (8-3) can be similarly applied.

8.2.5. Lateral Strength Degradation

The lateral strength reduction of bridge B3 is governed by damage to the columns. The wave loads cause damage to the column both due to excessive vertical loads as

well as lateral. Wave and surge loads do not follow the same pattern by increasing the hazard intensity.

A mathematical model is established to relate the global performance measure of strength reduction to the peak column demands in order to estimate a limit state capacity model for the case of 15% strength reduction, which is adopted as DS_2. Different *EDP*s have been tested to identify the most appropriate one to define the structural capacity in terms of correlation to global strength reduction and reduction of error in capacity limit state function. Maximum column curvature, peak average strain of the column section, maximum strain, peak lateral drift, peak average axial strain and peak total displacement ratio, defined as the ratio of the total displacement (lateral and vertical) over the height of the column, were examined. All of the tested parameters are the peak values recorded during the time history analysis. The condition of no degradation at zero demand was imposed as a constraint when testing different model forms and demand parameters. The results suggest that the power model has the best goodness of fit and that the maximum axial strain of the section provides a good predictor of strength reduction. This model form agrees with intuition since the degradation model of the materials constitutive laws is also governed by a power model, which

is a function of maximum strain and number of cycles (energy). Number of loading cycles can be considered to be embedded into the maximum strain, since the degraded material undergoes more strain with repeated cycling.

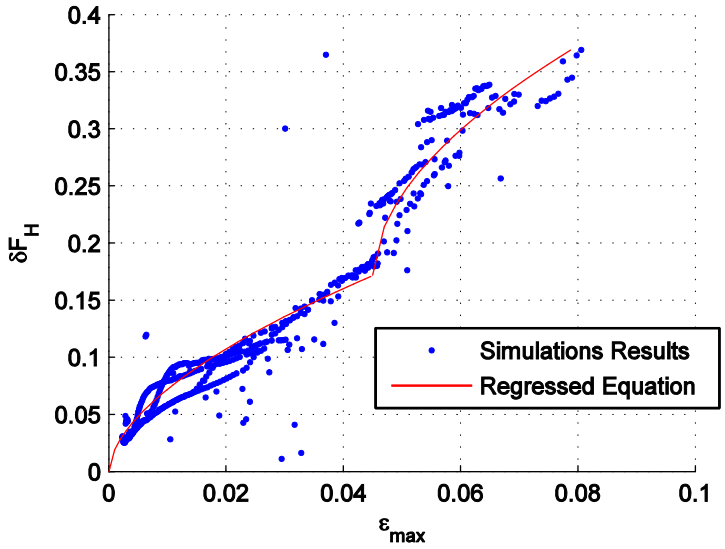

Figure 8-9. Lateral strength reduction versus peak maximum axial strain. The plot shows the results of the simulation and the regressed (bilinear in the logarithmic space) equation over the data.

Figure 8-9 presents the results of simulations in terms of maximum axial strain from the wave load simulations versus strength degradation found from the pushover analysis. This figure suggests more degradation at higher strain levels, which can be mainly attributed to the larger residual displacements after the end of the time history simulation, thus a larger P-Δ effect in the subsequent pushover. Therefore, the reduction of lateral load carrying capacity is greater at higher strain

values. The results were divided into two regions based on strength degradation: under 17% reduction and more than 17% reduction. The regression equation based on the maximum strain for the region of interest (i.e., $\delta R_H < 0.17$) is shown below for the global strength reduction:

$$\delta R_H = 1.032\varepsilon_{\max}^{0.578} \tag{8-5}$$

where δR_H is the degradation of the lateral strength. As previously noted, DS_2 is assumed to correspond to a 15% reduction in strength, and hence an estimate of the maximum strain capacity can be derived from the limit state capacity equation as shown below:

$$DS_2 \equiv [1.032\varepsilon_{\max}^{0.578} \geq 0.15 \Rightarrow \varepsilon_{\max} \geq 0.036] \tag{8-6}$$

Equation (8-6) provides the median value of the distribution for the maximum strain capacity limit for DS_2. The goodness-of-fit test at this level reveals a lognormal distribution for $\varepsilon_{\max}$ with logarithmic standard deviation equal to 0.20. Similar to the previous subsection, any other value of lateral strength reduction can be chosen as a damage state, and the homoscedasticity is reasonable across a range of strength reductions if other prescriptive limits are imposed.

8.2.6. Vertical Strength Reduction

The vertical strength of the structure reduces mainly when the pile uplift capacity is less than the tensile capacity of the columns, describing bridge model B4. The vertical uplift capacity is governed by the soil properties and the soil/pile interface. The strength reduction can be directly associated with the uplift of the piles during the wave and surge loading. Column degradation can also cause a reduction in the gravitational capacity of the bridge; however lateral strength reduction dominates when the bridge has strong foundation (e.g. B3). Piles lose their end bearing capacity after uplift. There is an additional reduction of strength due to the cyclic effect of loading, which causes a degradation of skin friction. The cyclic behavior of piles under axial load is not adequately characterized in the literature, as noted in Lo et al. (2010). The skin friction degradation is assumed herein to be a linear function of the maximum displacement, as it shown in the t-z curves presented by Kraft et al. (1981). The ultimate reduction of the skin friction is assumed to be equal to 15% at the displacement of $5u^*$, where u^* corresponds to the displacement that mobilizes the maximum skin friction strength. Improved models can be easily adopted in the future as they become available.

As the intensity of wave and surge loads increase on the bridge deck, by either increasing the wave height or decreasing the relative surge elevation, the vertical strength degradation increases. However, there is no major reduction in the vertical stiffness of the structure.

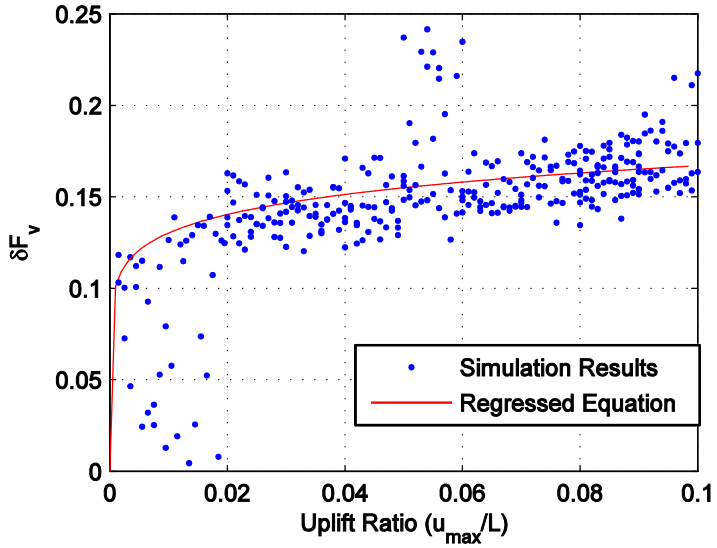

Figure 8-10. Vertical strength reduction versus peak uplift ratio. The plot shows the results of the simulation and the regressed equation over the data.

Since the gravitational load carrying capacity is mainly affected by the pile uplift for B4, the maximum pile uplift ratio, i.e. the amount of uplift over pile length, is selected and tested as the *EDP* correlated to the vertical load carrying capacity degradation. Figure 8-10 plots the results of simulations in terms of maximum pile uplift ratio from the wave load simulations versus strength

degradation found from the pushover analysis. Equation (8-7) shows the regressed model over the data, which has a R^2 goodness of fit of 0.86:

$$\delta F_V = 0.216\left(\frac{u_{\max}}{L_p}\right)^{0.110} \tag{8-7}$$

where $u_{\max}$, is the peak uplift during the time history analysis and L_p is the length of piles. The definition adopted for DS_3, of at least 15% reduction of vertical strength, leads to Equation (8-8):

$$DS_3 \equiv \left[0.216\left(\frac{u_{\max}}{L_p}\right)^{0.110} \geq 0.15\right] \Rightarrow \frac{u_{\max}}{L_p} \geq 0.0363 \tag{8-8}$$

Equation (8-8) reveals that 0.036 is the estimate of the median value capacity of $u_{\max}/L_p$ for DS_3. Similar to the prior sections, an additional set of simulations at this level of capacity is performed to evaluate the associated probability distribution of $u_{\max}/L_p$. A lognormal distribution is found to provide the best goodness of fit with the overall logarithmic standard deviation of 0.25, which corresponds to a *cov* of 0.25 at the prescribed strength reduction limit. The logarithmic standard deviation, considering only the structural parameter randomness is equal to 0.23. The dispersion is approximately constant over the range of stiffness reductions.

8.2.7. Illustration of Probabilistic Capacity Limit State Functions

The previous case studies revealed potential failure modes of bridges under hurricane induced wave and surge loads, and the contributing components for each mode. In particular, probabilistic capacity models were developed that indicate the functional form of component demands that contribute to system loss of strength and stiffness. Bridges B3 and B4 are of particular interest since intermediate levels of damage can be defined for them. The cumulative distribution functions of the capacity models associated with damage states DS_1 to DS_3 are plotted in Figure 8-11 for these two bridges. These fragility surfaces or curves indicate the probability of meeting or exceeding a damage state, given level of demand on key structural components that contribute to the failure mode of interest. For bridge B3, DS_1, corresponds to 40% lateral stiffness reduction as a function of the peak abutment displacement ratio, d_A/d_{Ay}, and maximum axial strain of columns, $\varepsilon_{\max}$. Figure 8-11(a) indicates the combinations of abutment displacement ratio and maximum axial strain of columns that lead to similar damage state exceedance probabilities. For example, a combination of d_A/d_{Ay} of 1 and $\varepsilon_{\max}$ of 0.5%, and a combination of d_A/d_{Ay} of 0.6 and $\varepsilon_{\max}$ of 2% both result in approximately 60% probability of DS_1. Damage state DS_2 for bridge B3 corresponds to 15%

degradation of lateral strength, with a median value of $\varepsilon_{\max}$ of 0.036 and *cov* of 0.19. Figure 8-11(b) reveals that for an event resulting in 4% axial strain on the columns, there is 71% probability of lateral strength reduction of at least 15% for the bridge system. Finally, vertical strength reduction for bridge B4 was found to be a function of pile uplift ratio, $u_{\max}/L_p$. The capacity estimate associated with 15% reduction of vertical strength follows a lognormal distribution with median value of $u_{\max}/L_p$ of 0.036 and *cov* of 0.23. Figure 8-11(c) illustrates approximately 66% probability of global damage DS_3 for a pile uplift ratio of 4%.

The probabilistic models for bridge capacity developed herein can be used for system reliability assessment of bridges under hurricane attacks, or to produce system fragility curves with damage probability conditioned upon hazard intensity. The capacity estimates derived relate local demand parameters to global system performance limits. Demands can subsequently be estimated by statistically analyzing the results of the nonlinear time history simulations to develop probabilistic models of demand on components found to contribute to the realization of loss of system performance at the bridge level. The derivation of probabilistic estimates of demand as a function of hazard intensity for retrofitted bridges is the scope of the next chapter.

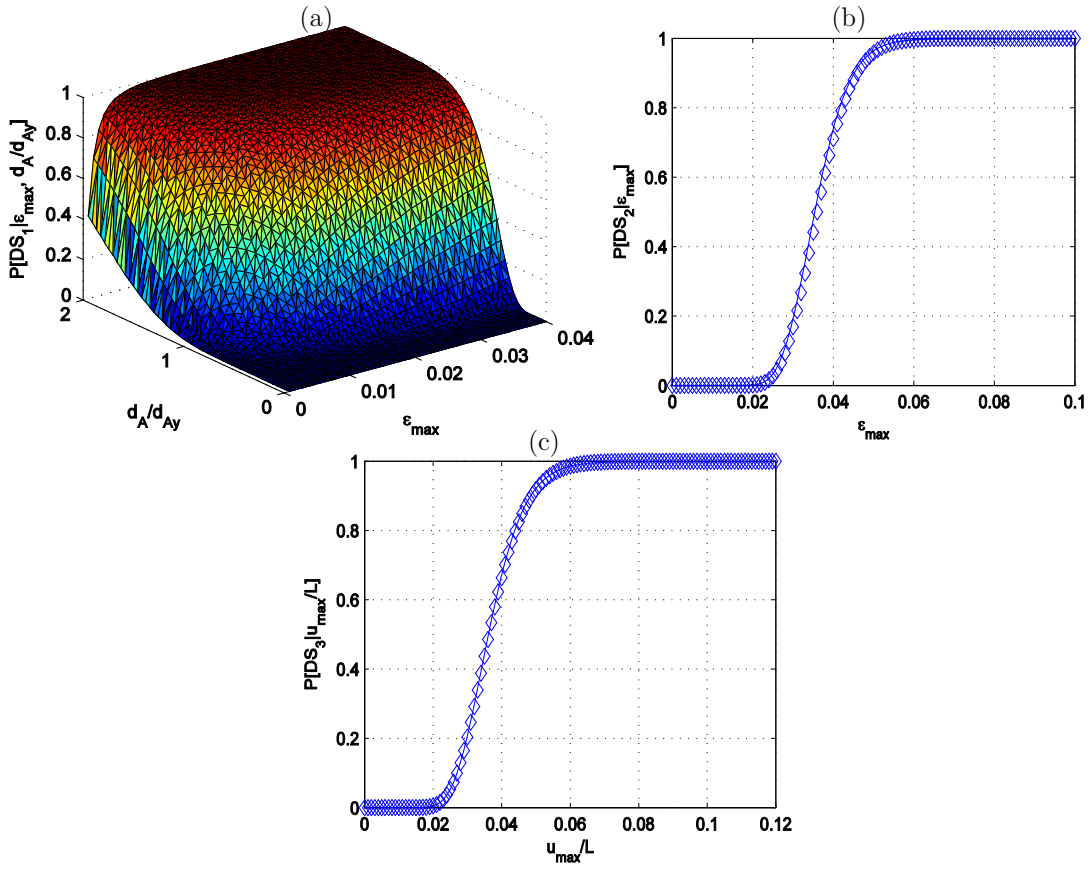

Figure 8-11. Capacity estimates presented as conditional probability of global system damage given level of component demand. (a) DS_1: lateral stiffness reduction of 40% as a function of abutment displacement and column axial strain for bridge B3, (b) DS_2: lateral strength reduction of 15% as a function of column axial strain for bridge B3, and (c) DS_3: vertical strength reduction of 15% as a function of pile uplift ratio for bridge B4.

8.3. Summary

Some potential bridge retrofits engage multiple potentially vulnerable components in system-level response to mitigate the effects of storm surge and wave loading. Therefore, new capacity limit state functions are developed for potential failure modes other than deck unseating for bridges subjected to coastal storms. A new

systematic method to evaluate the limit state capacity functions based on the post-event global performance of the bridge structure is introduced. This method averts the traditional challenge of system abstraction for reliability assessment while also providing identification of the components that contribute most to different system failure modes. The proposed capacity limit states are not only applicable to hurricane events, but also can be implemented for other hazards that invoke the similar responses in the structure. The application of this new prospective on deriving capacity limit state functions for reliability assessment will be illustrated in the next chapter for retrofitted bridges.

Chapter 9

Application of the Proposed Methods to the Houston/Galveston Bay Area

The developed reliability assessment methodologies for as-built and retrofitted bridges described in the previous chapters are applied to the Houston/Galveston Bay area bridge inventory to illustrate their application for regional risk assessment of existing inventory and determination of critical structures in lifeline routes. First, a brief overview of the existing bridge inventory is presented. The main characteristics and typical bridge types are discussed. After that, the MCS Static Model methodology is applied to the entire inventory to identify the vulnerable bridges under different hazard scenarios. Three different hazard scenarios are selected to demonstrate the potential susceptibility of the existing

bridge inventory under the coastal storms. The outcome of this study is of interest to public officials, to identify critical structures along lifeline routes and plan for risk mitigation strategies. Finally, three suggested retrofit measures, namely strong connections, shear keys, and restrainer cables are applied to two vulnerable bridges from the case study area and the reliability of the retrofitted bridges is assessed. This study will provide insight into the viability of using alternative retrofits to reduce the fragility of bridge.

9.1. Houston/Galveston Coastal Bridge Inventory

Determining the capacity of a bridge deck and the demand placed upon it during a hurricane event requires a significant amount of site specific data that must be obtained through inspection files and bridge plans. From the National Bridge Inventory (NBI 2010) data of state owned and operated bridges, approximately 200 structures are located in the Galveston Bay area, of which 136 bridges are considered in this investigation after eliminating tunnels, culverts and movable structures (Arnold 2011). Bridge inspection files and as-built plans were obtained from the Houston office of Texas department of transportation (TxDOT) and were mined for pertinent data. For each bridge, the following attributes were identified:

material and type of bridge, number and length of spans, width of bridge, connection details such as dowel bars or anchor bolts, girder type and size, height above water for each span, and depth of water under each span.

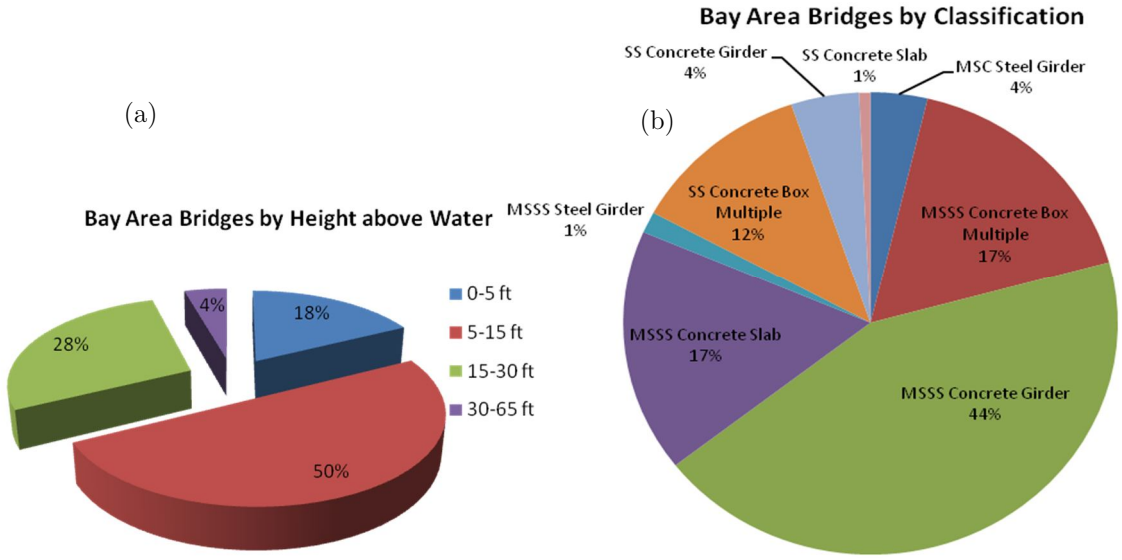

Figure 9-1. (a) Bridges water clearance; (b) classification of the bridges in the case study area. SS: Single span, MSSS: Multi Span Simply Supported, MSC: Multi Span Continuous.

A database of the critical bridge specific details has been created to be used for fragility modeling. As an example of the inventory analysis, Figure 9-1 shows the elevation above the mean water level of bridges in the area as well as classification of the bridge structure. As illustrated in this figure, the majority of bridges have relatively low water clearance. Additionally, multiple span simply supported (MSSS) concrete bridges comprise the majority of the bridge

infrastructure of this region, which have suffered significant damage in past events. Less than 30% of them have even limited capacity connections between super and substructure, rendering the inventory more vulnerable to deck unseating due to wave and surge loads. Figure 9-2 provides a visual representation of the water crossing bridges with their age. The majority of inventory was built before 1975. A comprehensive study on the bridges in the area can be found in Arnold (2011).

Three different hurricane scenarios are used to generate the wave and surge estimates at location of each bridge. The wave and surge data is provided by the computational hydraulic group (CHG 2011) using the coupled ADCIRC (2010) and SWAN (2010) models. A review of these models is provided in Chapter 2. The first simulated scenario is Hurricane Ike. The second scenario has 30% stronger wind than Hurricane Ike and is referred to as 145 Ike. The last scenario is 145 Ike Point 8, where the landfall location is shifted to the south. The last scenario is the worst case scenario for Galveston Bay area and generates the maximum surge due to the landfall location. These scenarios are presented in Figure 9-3. It should be noted that no error is considered in the hazard model wave and surge values. Therefore, the following results are provided assuming that the wave and surge values for each scenario is accurate.

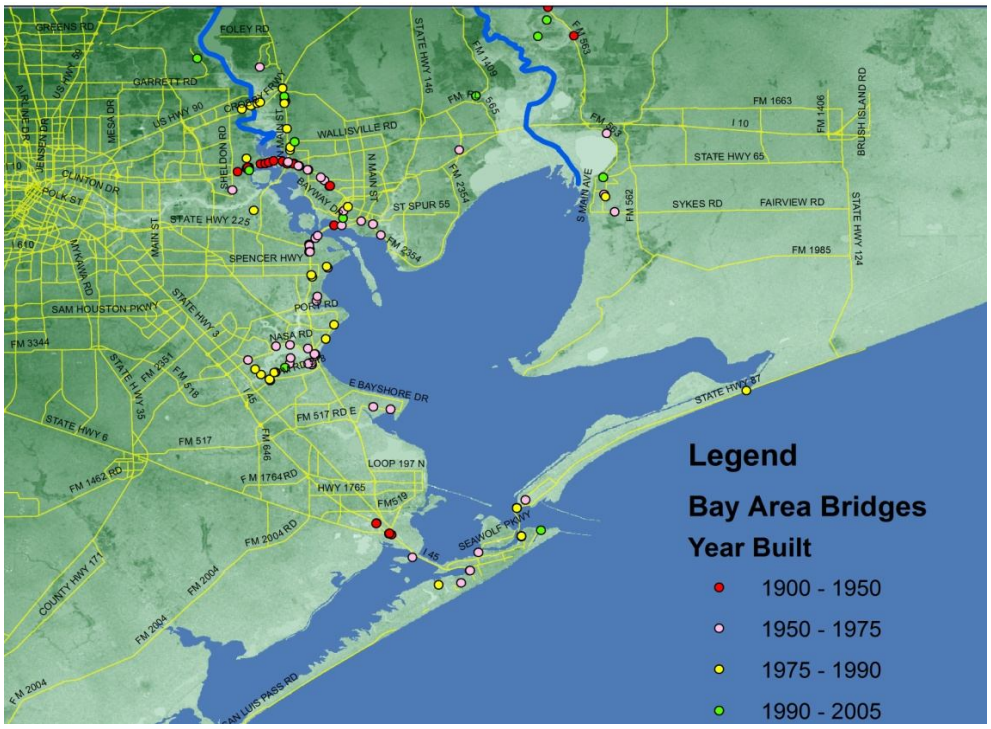

Figure 9-2. The Houston/Galveston Bay area bridge inventory.

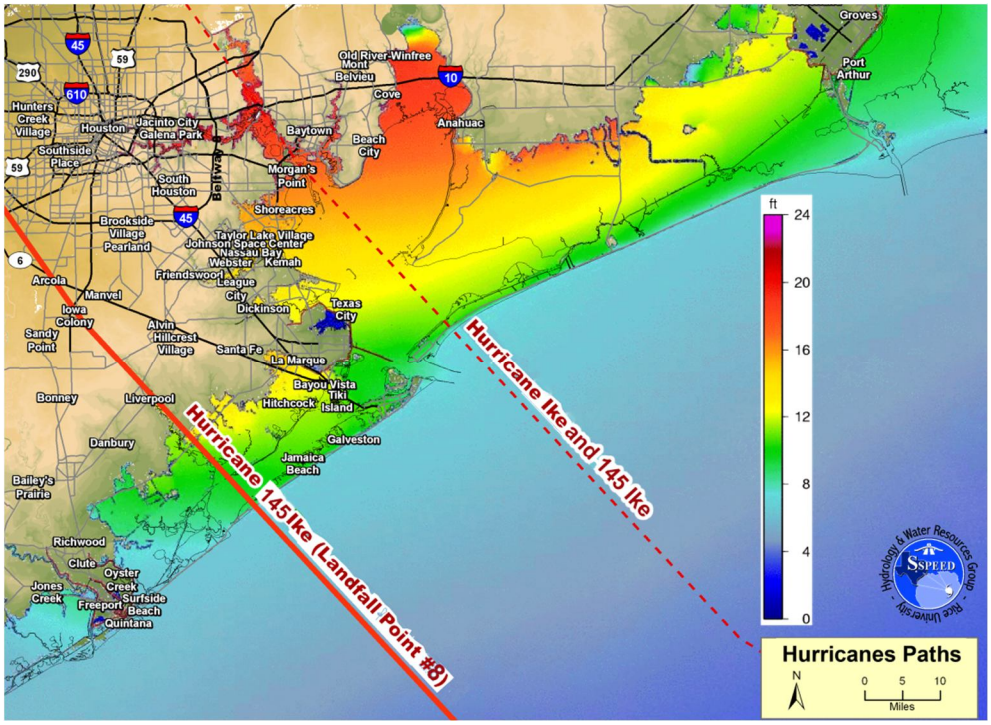

Figure 9-3. The path of the hurricane scenario events for the case study area [photo credit: Bedient research group (2012)].

9.2. Risk Assessment for Scenario Hurricane Events

9.2.1. Bridge Deck Inundation

The Inundation of bridge decks is assessed as a simple indicator of temporary functional inhibition, while the deck unseating affects the long term inaccessibility of the transportation network. According to the values of relative surge elevations at bridge locations, 28 bridges are inundated in Ike (Figure 9-4), where 82 bridges are inundated in 145 Ike. While the inundation can provide insight regarding temporary functionality inhibition, these types of inundation maps have unfortunately historically been considered as the basis of transportation infrastructure hurricane risk assessments along the Gulf Coast. Comparing this figure with Figure 9-5 reveals that all of the bridges with high probability of failure were inundated during Hurricane Ike. However, integrating the bridge fragilities is critical for assessing long term consequences from bridge failure potential for a more holistic regional risk assessment of infrastructure performance. The Full set inundation maps for different hurricane scenarios are presented in Arnold (2011).

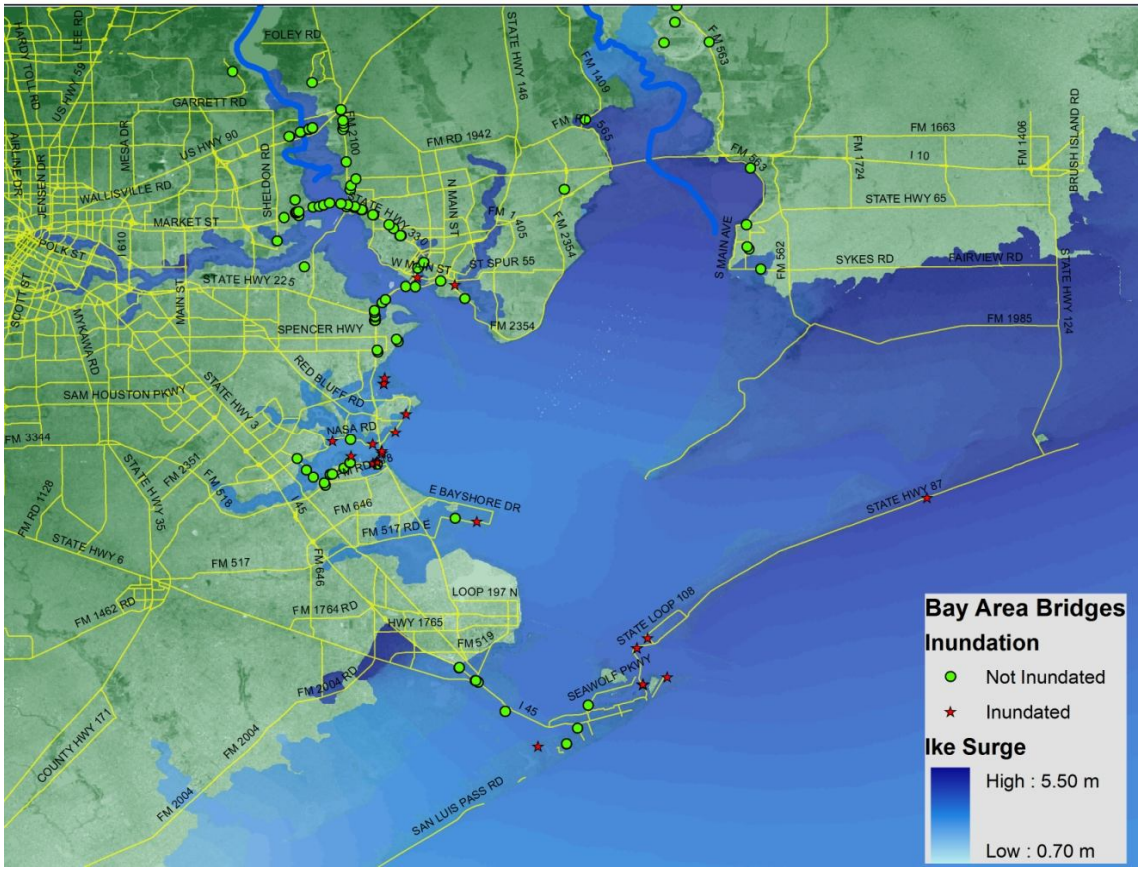

Figure 9-4. Inundation map for the Hurricane Ike scenario.

9.2.2. Bridge Deck Unseating

The probability of failure for bridges in the case study area is assessed based on the regional bridge database and probabilistic reliability modeling approach presented in Section 6.1 for the wave and surge estimates for each scenario event. The reliability approach is based on the Static Modeling methodology which utilizes Monte Carlo simulation as described in Section 6.1. This method is viable for rapid screening of the vulnerable bridges as illustrated herein. Figure 9-5 illustrates the

probability of unseating failure of the Houston Bay area bridges for the Hurricane Ike scenario given the observed *IM*s at each location. Most of the bridges in the area have a very low probability of failure, as expected based on the empirical data from the event. Only three bridges have a probability of failure above 0.75. Among them is the unseated bridge during Hurricane Ike, Rollover Pass Bridge, with the probability of failure of 1. Although full validation of a statistical model is not possible with the limited data, this simple illustration provides a basic validity check of the approach.

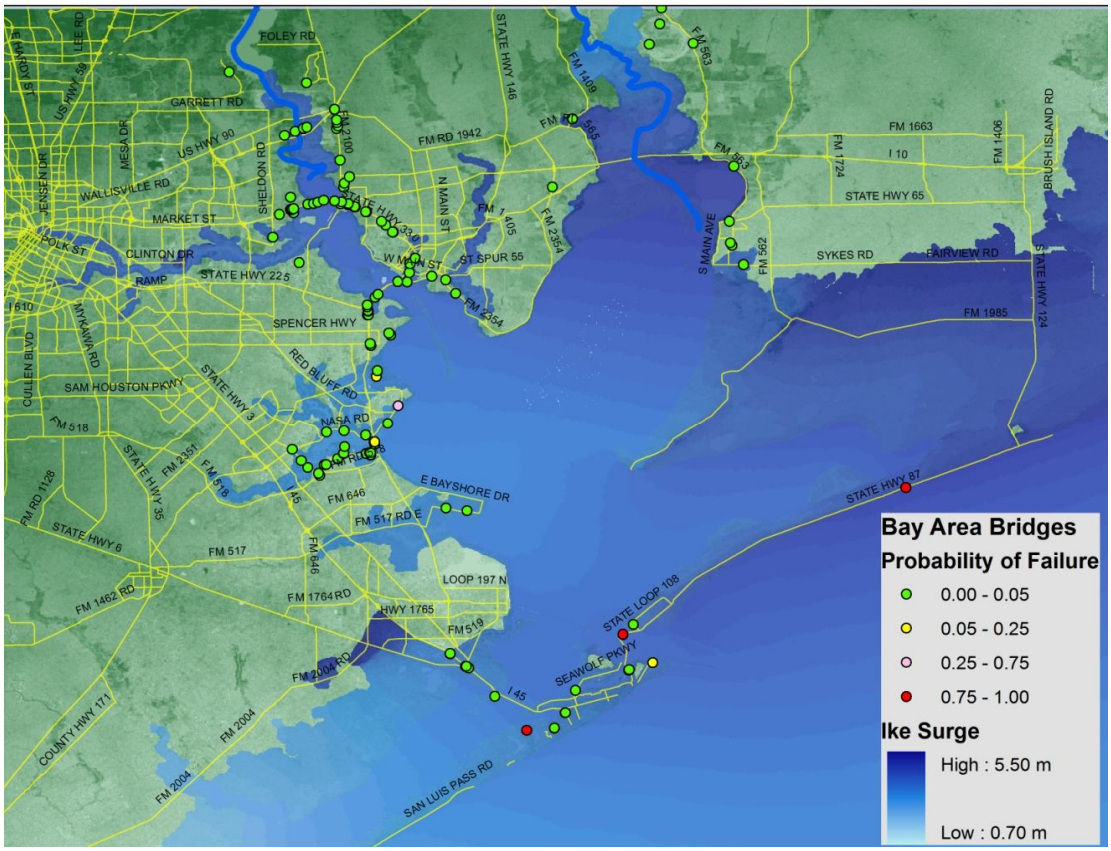

Figure 9-5. Probability of failure of bridges in Houston/Galveston for the Ike scenario.

Figure 9-6 shows the probability of failure of bridges for 145 Ike while Figure 9-7 shows the probability of failure of bridges in the case study area for 145 Ike Point 8. The potential for the deck unseating of bridges in the area increases as the strength of wave and surge increases, either by changing the landfall location or increasing the wind speed. These example risk assessments demonstrate the insights into the regional distribution of damage that can be obtained by coupling the fragility curves derived for the analyzed bridges with any given scenario or probabilistic hazard estimates.

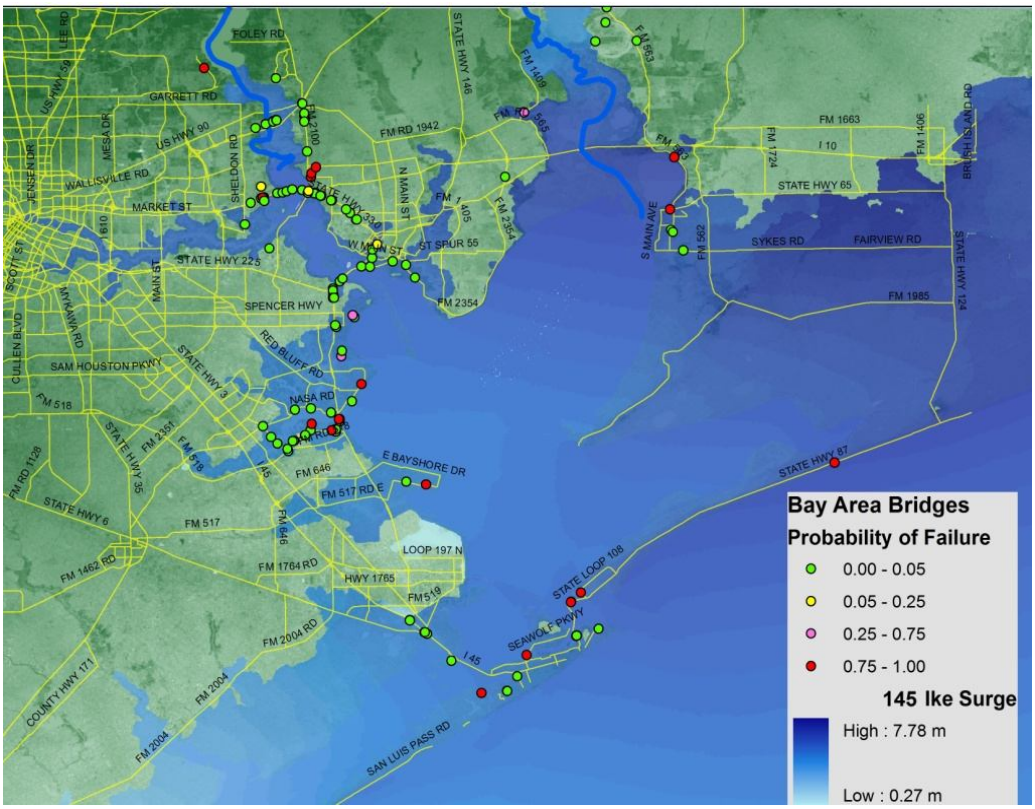

Figure 9-6. Probability of failure of bridges in Houston/Galveston bay area for the 145 Ike scenario.

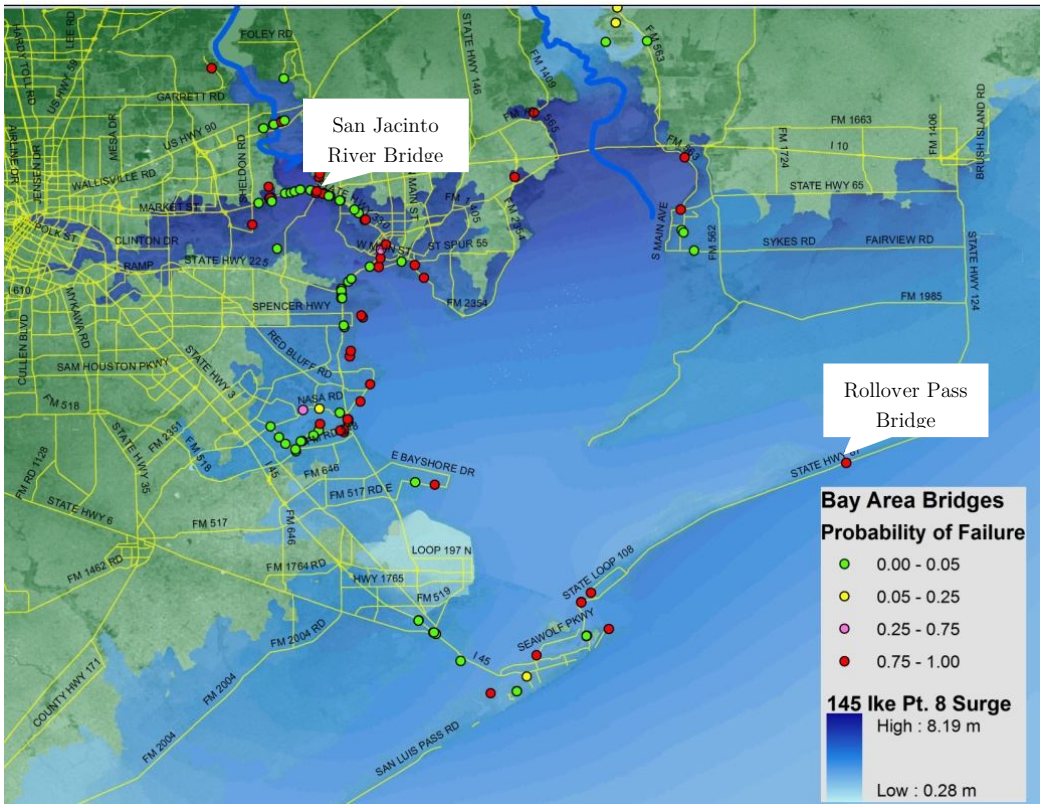

Figure 9-7. Probability of failure of bridges in Houston/Galveston bay area for the 145 Ike Point 8 scenario.

9.3. Retrofit Measures for Vulnerable Coastal Bridges

A reliability study is performed for two distinct bridges that are selected from the inventory to investigate the effect of different retrofit measures on the response of coastal bridges under hurricane induced wave and surge loads. These bridges are susceptible to bridge deck unseating under wave and surge conditions from hurricane events as shown in Figure 9-7. The first bridge is the Rollover Pass Bridge. This bridge is a concrete box beam simply supported span bridge with

22.1m width. Each span is supported by a bent beam of 0.7m dimension. The bent is supported by twelve driven square piles of 0.4m dimension. Approximately, 10m of the piles are in the ground. The soil type in this bridge location is clay. Figure 9-8 shows this bridge after Hurricane Ike. Figure 9-9 plots the Rollover Pass Bridge cross section.

Figure 9-8. Rollover Pass Bridge after Hurricane Ike.

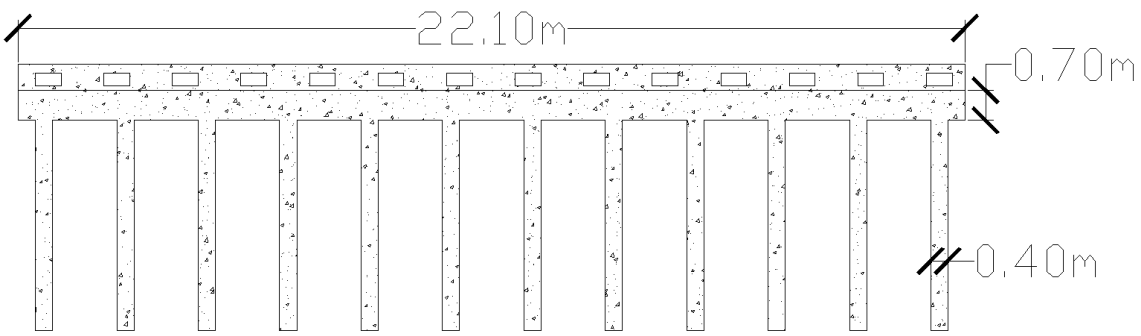

Figure 9-9. Rollover Pass Bridge.

The second bridge is San Jacinto River Bridge (Figure 9-10) which has a concrete girder simply supported span structure. Each span is supported on a square bent beam of 1m dimension. Three circular concrete columns of 0.9m diameter and about 5.5m height support the bent beam. The bridge is located on a soft clay site. Four square piles of 0.53m dimension and 16.2m long support each column's foundation. Figure 9-11 depicts the cross section of San Jacinto Bridge.

Figure 9-10. San Jacinto River Bridge (retrieved from maps.google.com).

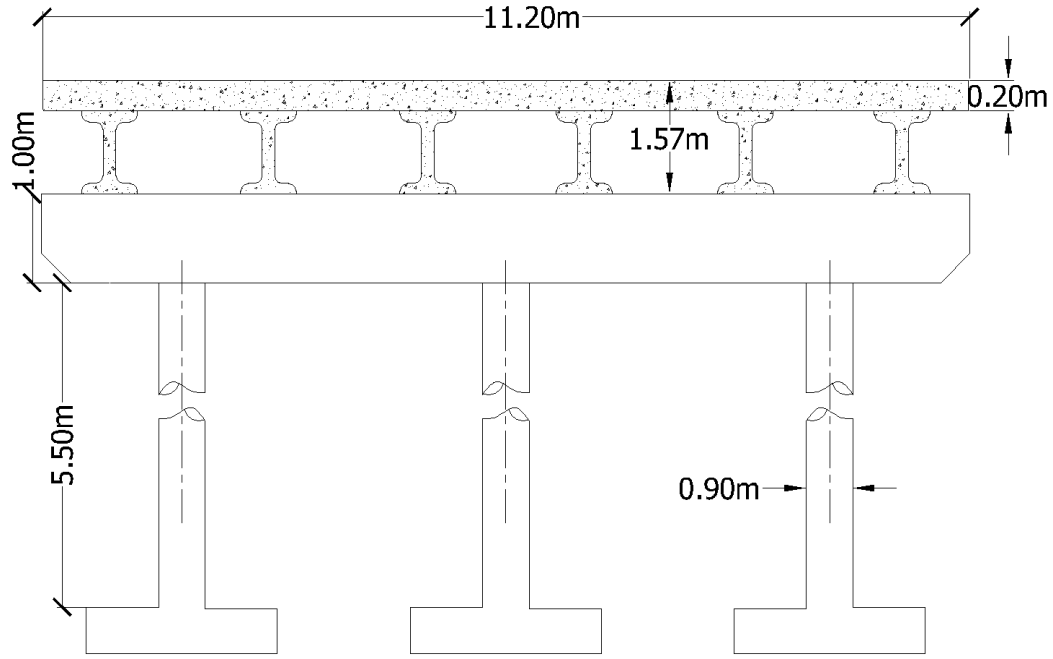

Figure 9-11. San Jacinto River Bridge.

Reliability assessment is conducted for these bridges for both as-built and retrofitted cases. A total of 256 points are generated over the range of -2m to 2m for relative surge elevation and 0m to 5m for wave height. Quasi-Monte Carlo sampling technique is used to generate realizations of random variables that are presented in Table 5-2 and Table 5-8. FSI Model is utilized to capture the details of bridges' responses. RF-FSI (random forests combined with FSI Model) that described in Chapter 7 is used for as-built bridges. New damage states that are described in Chapter 8 are used herein to evaluate the reliability of the retrofitted bridges.

9.3.1. As-Built Case Study Bridge Failure Modes

9.3.1.1. Rollover Pass Bridge

The deck width of this bridge is large, and it consists of eighteen box beam girders. The girders are placed next to each other and the gap in between is filled with a cast in place concrete. According to the as-built plans, there is no detail (such as roughening the surfaces or addition of rebars) to improve the bond between the cast in place concrete and the box beams sides. Therefore, the girders can be separated under extreme wave forces and unseat from the bent beam. The results of the 256 simulations with fully connected girders do not lead to any failure or unseating. The wave cannot overcome the entire deck weight. However, if the girders are modeled separately with contact element in between, their separation and unseating can be detected. This was the real failure mechanism that occurred in the field (Stearns and Padgett 2010). The bridge deck is reconstructed to the same condition after Hurricane Ike; thus, it is susceptible to the same mode of failure in the future events. Figure 9-12 depicts the separation of the girder under the wave forces. The results of 256 simulations are used to train a random forests model. The RF-FSI for this bridge is plotted in Figure 9-13 which demonstrates the potential vulnerability of the girder unseating of the bridge deck.

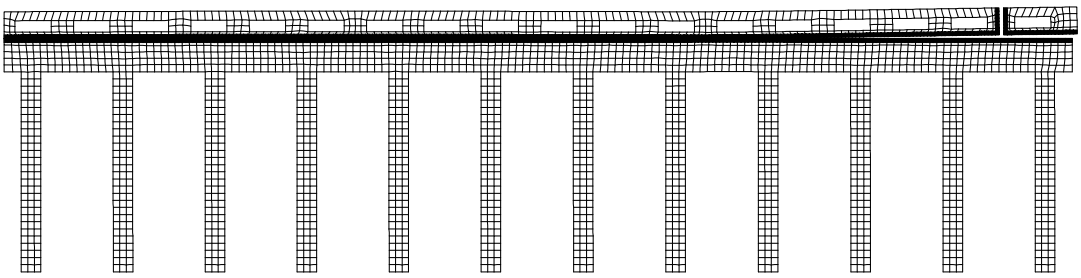

Figure 9-12. Separation and girder unseating of Rollover Pass Bridge under wave and surge action.

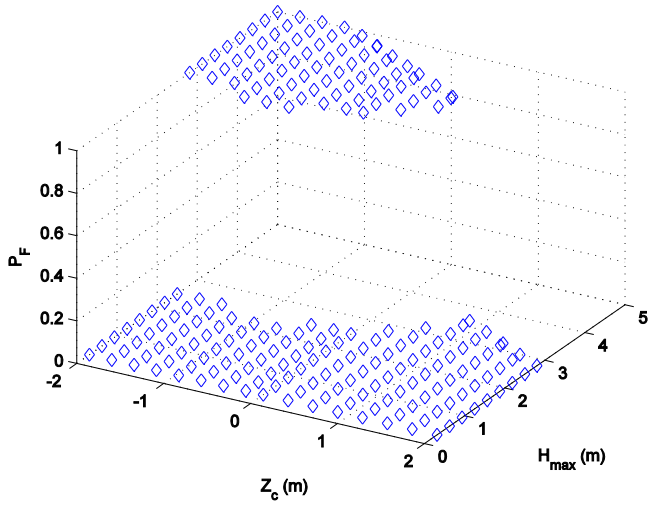

Figure 9-13. RF-FSI fragility for as-built Rollover Pass Bridge.

9.3.1.2. San Jacinto River Bridge

San Jacinto River Bridge demonstrates the deck unseating failure mode under extreme wave and surge events. The bridge deck movement is similar to the movement that was illustrated in the deterministic response of a case study bridge in Section 4.2.5. The only difference is that San Jacinto River Bridge has TxDOT 54 girders, which are similar to AASHTO type IV girders. Therefore, the deck is

heavier and thus, the bridge is less fragile than the case study bridge presented in Sections 4.2.5 and 6.3. Similar to Rollover Pass Bridge, the results of 256 simulations are used to train a random forests model. The RF-FSI for San Jacinto Bridge is plotted in Figure 9-14. The effect of retrofit measures is investigated in the next section.

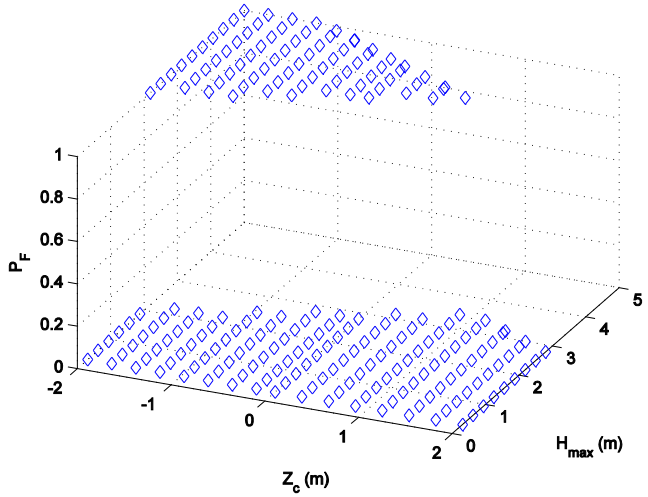

Figure 9-14. RF-FSI fragility for as-built San Jacinto River Bridge.

9.3.2. Bridges Retrofitted with Shear Keys

Shear keys are added to restrain the bridge deck movement in transverse direction. Shear keys are designed based on shear friction criteria as follows (Priestley et al. 1996):

$$V_{sk} = \phi_s \mu A_s f_y \tag{9-1}$$

where φ_s is the shear reduction factor, μ is the coefficient of friction and is equal to 1.4 for normal cracks, and A_s is the total area of reinforcement (Priestley et al. 1996). The shear keys are designed for a fraction of substructure yield strength. The strength reduction factor is omitted in the reliability analysis.

9.3.2.1. San Jacinto River Bridge

Shear keys of 0.38 m height are added to the bent beam to prevent bridge deck unseating. None of the simulations led to deck unseating. Figure 9-15 shows the response for the worst scenario with relative surge elevation of -1.5 m, wave height of 4.6 m and wave period of 6.2 s. For the unretrofitted case study bridge, the deck is uplifted from its support, and undergoes large displacement; eventually unseated from the bent beam. Large vertical displacement is also observed for the bridge deck with shear key. However, the transverse displacement is limited by the existence of the shear keys. It should be noted that this is the most extreme deck movement for the bridge retrofitted with shear keys, and the other simulations have a smaller vertical displacement. Therefore, the developed numerical model demonstrates the effectiveness of shear keys on restraining the transverse displacement of the deck, as has been observed in the field for other bridges. Figure 9-16 plots the vertical and transverse displacement of the top waveward node of

the deck. This plot shows that the maximum vertical deck displacement of the retrofitted is more than the as-built bridge; however, the transverse displacement is limited to the gap between the shear key and the outermost girder (0.3m). Therefore, the implemented shear keys prevent the deck unseating.

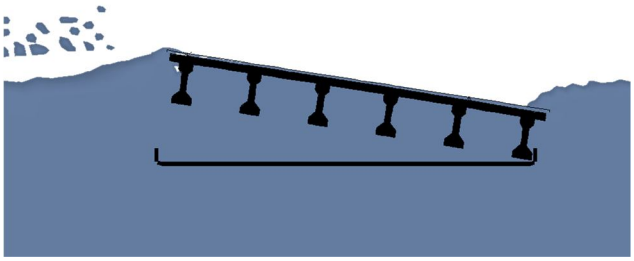

Figure 9-15. Displacement of the bridge deck with shear keys under extreme wave and surge condition. Superstructure domain is depicted only.

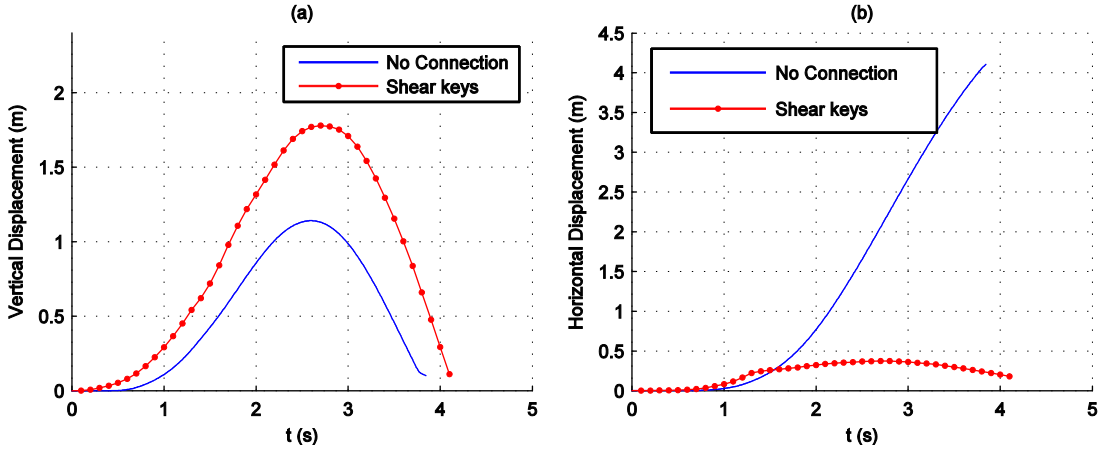

Figure 9-16. Comparison of: (a) vertical; and (b) horizontal deck displacements for the bridge without and with shear keys.

For the bridge with shear keys the deck slams back after the wave passage, which generates high contact stresses on the bent beam. The plot of the normal

stress is shown in Figure 9-17. The maximum stress is approximately 12MPa, which is lower than the crushing strength of the concrete (25MPa). However, it can cause spalling of the concrete and tensile cracking; which can be considered as minor damages. The tensile strength of the concrete is about 3MPa. Also, stress concentration can occur at the edge of shear key as depicted in Figure 9-18. The stress concentration causes tensile cracking in the shear key, which can be considered as a minor damage. No significant demands exist on the rest of the bridge structure. Therefore, addition of shear keys prevents deck unseating effectively without increasing the other components' potential of damage.

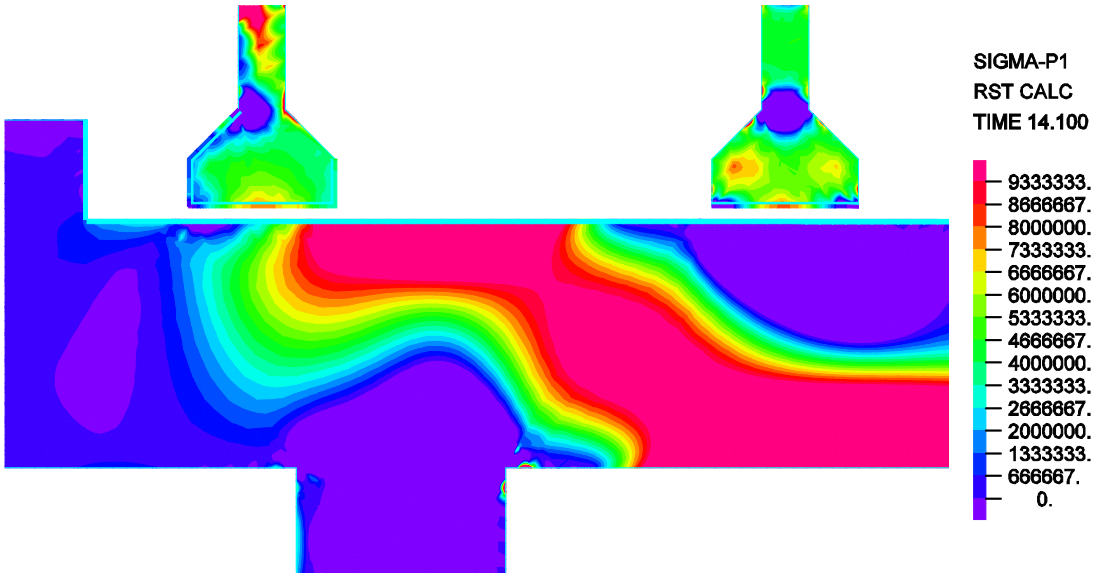

Figure 9-17. Large stresses on girder and bent cap at the moment of impact (stress unit is Pa).

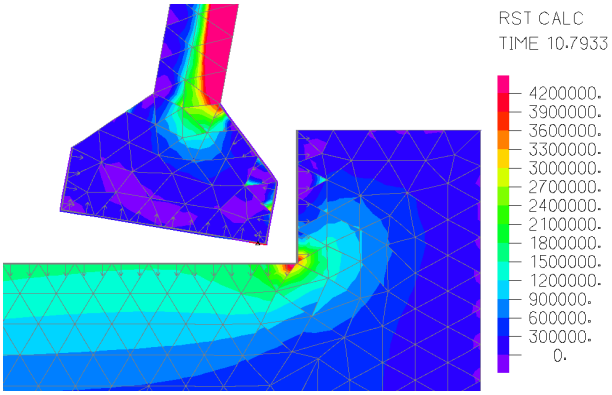

Figure 9-18. Stress concentration near the shear key before concrete tensile cracking (stress unit is Pa).

The probability of failure is zero for all damage states that are defined in the previous chapter for the bridge retrofitted with shear keys. These damage states are 40% reduction in lateral stiffness, 15% reduction in lateral strength and 15% reduction in vertical strength. The fragility of the retrofitted San Jacinto Bridge for these damage states can be mathematically presented as follows:

$$\begin{aligned} \mathrm{P}\left[DS_1 \mid \mathbf{IM}\right] &= \mathrm{P}\left[\delta K \geq 0.4 \mid \mathbf{IM}\right] = 0;\ \forall \mathbf{IM} \\ \mathrm{P}\left[DS_2 \mid \mathbf{IM}\right] &= \mathrm{P}\left[\delta R_H \geq 0.15 \mid \mathbf{IM}\right] = 0;\ \forall \mathbf{IM} \\ \mathrm{P}\left[DS_3 \mid \mathbf{IM}\right] &= \mathrm{P}\left[\delta R_V \geq 0.15 \mid \mathbf{IM}\right] = 0;\ \forall \mathbf{IM} \end{aligned} \tag{9-2}$$

9.3.2.2. Rollover Pass Bridge

The response of Rollover Pass Bridge can also be controlled efficiently through the addition of shear keys. Shear keys prevent the girder separation and falling. Results of numerical simulation of Rollover Pass Bridge retrofitted with shear keys do not

reveal any damage, as the structure essentially remains in the elastic region. Therefore, the results suggest that the addition of shear keys can effectively prevent structural damage to the Rollover Pass Bridge as shown in Figure 9-19. The mathematical representation of fragility for different damage states is shown in Equation (9-3).

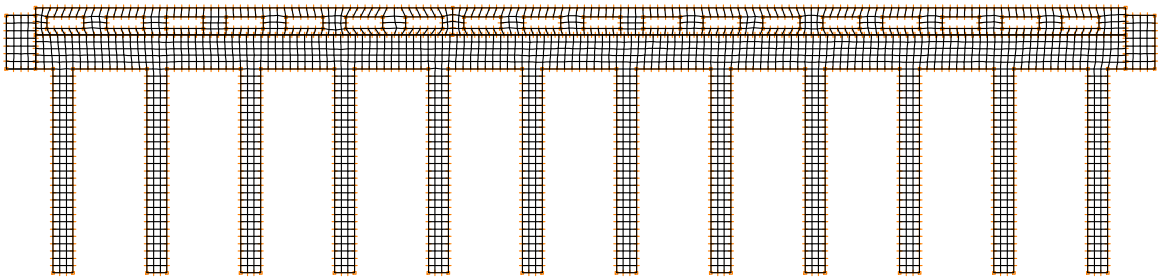

Figure 9-19. Rollover Pass Bridge with shear keys indicating no sign of damage under wave and surge action.

$$\begin{aligned} \mathrm{P}\left[DS_1 \mid \mathbf{IM} \right] &= \mathrm{P}\left[\delta K \geq 0.4 \mid \mathbf{IM} \right] = 0;\ \forall \mathbf{IM} \\ \mathrm{P}\left[DS_2 \mid \mathbf{IM} \right] &= \mathrm{P}\left[\delta R_H \geq 0.15 \mid \mathbf{IM} \right] = 0;\ \forall \mathbf{IM} \\ \mathrm{P}\left[DS_3 \mid \mathbf{IM} \right] &= \mathrm{P}\left[\delta R_V \geq 0.15 \mid \mathbf{IM} \right] = 0;\ \forall \mathbf{IM} \end{aligned} \tag{9-3}$$

9.3.3. Bridges Retrofitted with High Strength Connections

High strength connections that can essentially prevent the relative movement of the deck with respect to its support are considered for this section. These connections are assumed to be stronger than the bridge substructure, similar to those that was implemented in the case study bridges in Section 8.2. The high

strength connections provide a force transmission path between the super- and substructure. However, the simulation results for both Rollover Pass Bridge and San Jacinto River Bridge demonstrate no damage with high strength connections between the bridge deck and its substructure. For both bridges, this can be displayed as Equation (9-4):

$$\begin{aligned} \mathrm{P}\left[DS_1 \mid \mathbf{IM}\right] &= \mathrm{P}\left[\delta K \geq 0.4 \mid \mathbf{IM}\right] = 0;\ \forall \mathbf{IM} \\ \mathrm{P}\left[DS_2 \mid \mathbf{IM}\right] &= \mathrm{P}\left[\delta R_H \geq 0.15 \mid \mathbf{IM}\right] = 0;\ \forall \mathbf{IM} \\ \mathrm{P}\left[DS_3 \mid \mathbf{IM}\right] &= \mathrm{P}\left[\delta R_V \geq 0.15 \mid \mathbf{IM}\right] = 0;\ \forall \mathbf{IM} \end{aligned} \tag{9-4}$$

The pile uplift capacity is less than the column strength. Therefore, one failure mode is possible, which is the pile uplift for San Jacinto River Bridge. The assumed median soil cohesion strength for this bridge based on the as-built map is 30kPa. As presented in Equation (8-3), the probability of the third damage state, which corresponds to the pile uplift, for this bridge is zero. However, hypothetically and only for illustration purpose, assuming that San Jacinto River Bridge is located in a weak clay soil, with the median undrained cohesion strength of 18kPa, the pile uplift is possible. A probabilistic demand model is developed over the result of the pile uplift ratio for this bridge using the response surface model.

Figure 9-20 shows the pile uplift for this hypothetical bridge model. The best form of regression is power with R^2 of 0.86:

$$\ln\left(\frac{u_{\max}}{L_p}\right) = -16.8 + 1.01(6.5 - Z_c) + 0.87H_{\max} \tag{9-5}$$

The above equation represents the median of a lognormal distribution with the logarithmic standard deviation of 0.51. The substructure of this bridge is similar to the case study bridge in Section 8.2. Thus, the same damage state definitions can be implemented here. Given DS_3 defined in Equation (8-8), a closed form solution can be obtained as shown below:

$$\mathrm{P}\left[DS_3\right] = P\left[\frac{u_{\max}}{L_p} \geq 0.036 \mid \mathbf{IM}\right] = \Phi\left(\frac{-\ln\left(0.036\right) + \left(-16.8 + 1.01\left(6.5 - Z_c\right) + 0.87H_{\max}\right)}{\sqrt{0.51^2 + 0.23^2}}\right) \tag{9-6}$$

where Φ is the standard normal cumulative distribution function. This fragility can be visually presented as shown in Figure 9-21. The probability of failure is close to zero for the most of the hazard range. This figure suggests that even in a poor soil condition, the chance for the pile uplift is small.

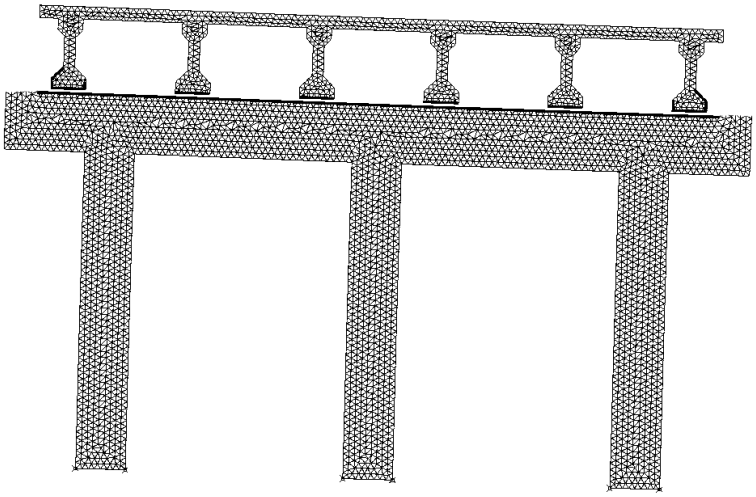

Figure 9-20. Pile uplift for San Jacinto River Bridge retrofitted with high strength connections between super- and substructure.

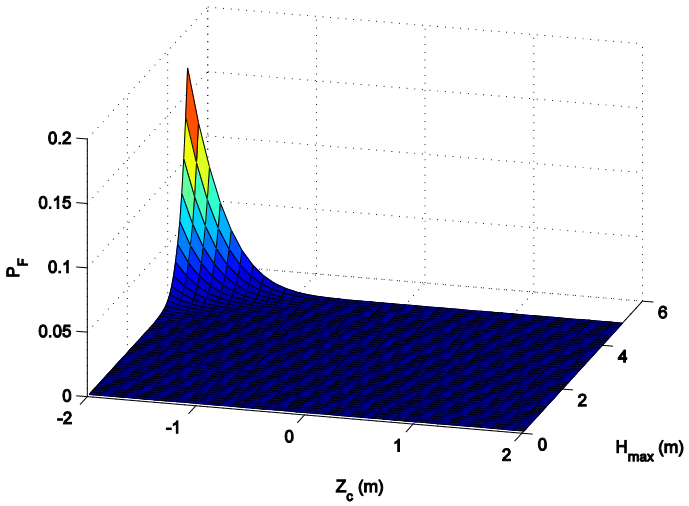

Figure 9-21. Fragility surface for pile uplift of San Jacinto River Bridge.

9.3.4. Bridge Retrofitted with Restrainer Cables

Restrainer cables connect the girders to the sides of the bent beam. The restrainer cables are made of high strength steel with median yield strength of 1210MPa

(Caltrans 2002). The slack is considered for these cables as a uniform variable between 0 to 9mm (Padgett 2007). For the 256 simulations, the strength and slack of the cables are added as the two new random variables to Table 5-8. Quasi-Monte Carlo sampling technique is used to generate realizations of them along with other random variables. Two cables are added at each side of the deck, connecting the outermost girders to the bent cap. Each cable is designed to have an area which is able to carry half of the deck weight (Padgett 2007). In addition, it is assumed that the cables connection points are strong enough to bear the forces and transfer them to other components without stress concentration. This assumption is in the numerical model by using elastic material near the cable connection zones.

9.3.4.1. San Jacinto River Bridge

The reliability analysis of the retrofitted bridge with the restrainer cables demonstrates no damage in any structural components over the range of hazard intensity. Figure 9-22 shows the magnified displacement of the bridge deck under the wave and surge load. For this bridge, the fragility can be displayed as follows:

$$\begin{aligned} \mathrm{P}\left[DS_1 \mid \mathbf{IM}\right] &= \mathrm{P}\left[\delta K \geq 0.4 \mid \mathbf{IM}\right] = 0;\ \forall \mathbf{IM} \\ \mathrm{P}\left[DS_2 \mid \mathbf{IM}\right] &= \mathrm{P}\left[\delta R_H \geq 0.15 \mid \mathbf{IM}\right] = 0;\ \forall \mathbf{IM} \\ \mathrm{P}\left[DS_3 \mid \mathbf{IM}\right] &= \mathrm{P}\left[\delta R_V \geq 0.15 \mid \mathbf{IM}\right] = 0;\ \forall \mathbf{IM} \end{aligned} \tag{9-7}$$

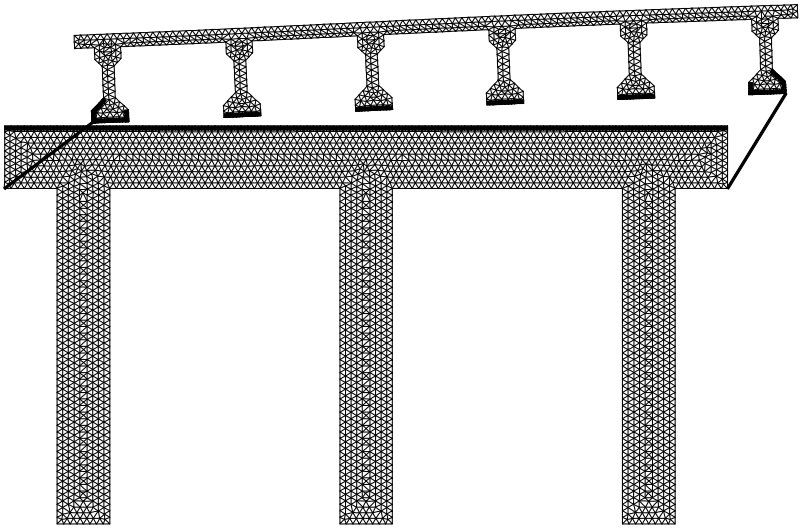

Figure 9-22. Magnified displacement of the bridge deck restrained by restrainer cables (magnification factor = 25).

9.3.4.2. Rollover Pass Bridge

The reliability analysis of the retrofitted Rollover Pass Bridge is significantly different from the San Jacinto River Bridge. The restrainer cables are found to be less effective in preventing the separation of girders. There is a slight chance for separation and unseating even with the existence of the cables. There is no other damage observed in the other components. The fragility response of the Rollover Pass Bridge with restrainer cable is plotted in Figure 9-23. The result shows a reduction in the fragility with respect to the unretrofitted bridge. The result shows a 21% reduction in the bridge vulnerability; i.e., in cmparison th the as-built bridge, the deck unseating occurs on the 21% smaller region of hazard intensity

measure. Though restrainer cables are not ineffective for this bridge, their performance is significantly lower comparing to shear keys.

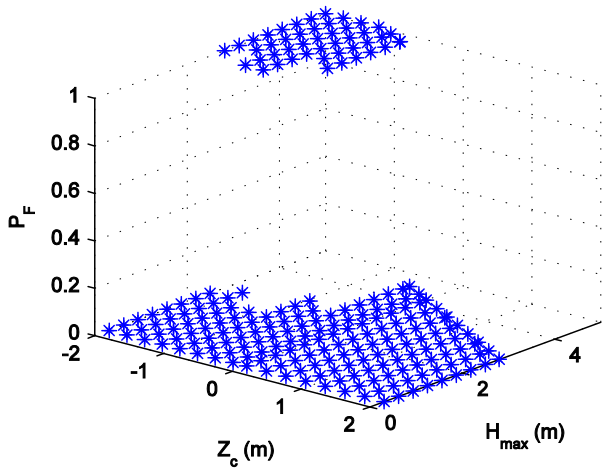

Figure 9-23. RF-FSI of the Rollover Pass Bridge retrofitted with restrainer cables.

9.4. Summary

This chapter demonstrates the application of the developed reliability methodologies by applying them to the Houston/Galveston Bay area bridge inventory. The Static Model Methodology for deck unseating is employed for fast screening of the vulnerable structures under hurricane scenario events, since simply supported bridges comprises the majority of the inventory. The result of this study reveals the potentially vulnerable bridges in the area. The results reveal that many of the bridges are susceptible to the deck unseating failure mode under hurricane induced wave and surge loads. Two vulnerable structures from the area

are selected to investigate the effect of different retrofit measures. The impact of shear keys, high strength connections, and restrainer cables on the fragility of these bridges are examined. Shear keys are determined as the most effective measure for prevention of deck unseating. The addition of shear keys restrains the bridge deck movement and does not transfer large forces to substructure. The probability of all damage states presented in Chapter 7 such as lateral strength reduction or vertical strength reduction is approximately zero. However, minor damages such as cover concrete spalling or concrete tensile cracking is expected. Implementing high strength connections can also effectively prevent deck unseating failure mode. However, there is a small chance for pile uplift for bridges located in the weak soil. Restrainer cables are also effective in preventing the deck unseating. However, if the bridge deck is consists of separated girders that are not appropriately tied together, as it is the case for Rollover Pass Bridge, the restrainer cannot prevent the girder separation and unsetting over the entire range of the hazard intensity.

In sum, application of full strength connections may lead to damages to pile system. Restrainer cables may not be as effective as shear keys for bridges with (separate) pre-cast girders. Also, their implementation is harder than shear keys and requires preparation for anchorage. Implementation of shear keys is easy and

cost effective. Therefore, this study suggest the use of shear keys since they can effectively prevent the deck unseating for different simply supported span bridges without causing any main damage to other structural components.

Chapter 10

Conclusions and Future Work

10.1. Summary and Conclusions

The potential vulnerability of the coastal bridges to hurricane induced wave and surge loads has been ignored until the recent hurricane events such as Hurricane Katrina, Hurricane Ivan, and Hurricane Ike to name a few. These hurricane events demonstrated the susceptibility of the bridge inventory along the US Gulf Coast to damage hampering emergency response and long term recovery. The lack of appropriate detailing to sustain wave and surge loads leaves the transportation network particularly vulnerable to coastal storm damages.

The main goal of this research was to construct a systematic methodology to quantify the structural vulnerability of bridges under coastal storms, offering a

probabilistic framework, input tools, and application illustrations. This work is timely as many states along the Gulf Coast are beginning to evaluate the performance of coastal structures under severe wave and surge action. Unfortunately, to date, very few studies have assessed the response of the coastal bridges under hurricane wave and surge loads. This research was aimed to cover this gap by providing a reliability assessment framework for coastal bridges.

The main results and contributions of this research can be summarized as follows:

- A simplified wave load model is constructed by coupling the existing methods for the estimation of peak wave forces on bridge decks and the results of the past experimental test data. A bias removal function is derived for both AASHTO wave load model and Douglass wave load model. Additionally, the uncertainty in the AASHTO wave load model is captured by introducing a model error term. Furthermore, a phenomenological model for deriving the time history of the wave forces is developed in this research.
- Recommendations on finite element modeling of coastal bridges are provided as part of this research. In particular, appropriate modeling techniques to capture deck uplift and unseating, which is the predominant mode of failure

of coastal bridges, are presented. Furthermore, a high fidelity fluid-structure interaction model (FSI) is developed and validated through comparison with the experimental test data. The FSI model takes into account the significant intricacies, such as turbulence, wave diffraction, and air entrapment, as well as material and geometric nonlinearities in structure.

- The most influential wave and surge parameters on the response of the coastal bridges are identified to be the maximum wave height and relative surge elevation. The reliability assessment of coastal bridges is conditioned upon these two parameters, referred to as hurricane intensity measures.
- A thorough sensitivity study reveals the random variables that significantly contribute to the response of the coastal bridges. Main structural parameters include material strength and density, bridge geometry, and soil strength. Appropriate probability density functions are assigned to each of these random variables.
- A Static Model that implements Monte Carlo simulation is developed for the reliability evaluation of the bridge deck unseating failure mode. The developed model is computationally efficient and can be applied to large bridge inventories for rapid screening of vulnerable structures. Additionally,

the application of the developed structural finite element models with the Modified AASHTO loads as well as the FSI Model for the reliability analysis of coastal bridges is demonstrated.

- The computational expenses for structural reliability assessment can be significantly reduced, while capturing uncertainties in the problem, by utilizing appropriate statistical models over the results of numerical simulations. Statistical learning tools such as logistic regression, random forests and support vector machines are used to develop fragility surfaces for coastal bridges vulnerable to storms. The performance of each of these techniques is evaluated and compared. The random forests models are found to have the best performance for the bridge deck unseating failure mode.
- Potential retrofit measures to prevent bridge deck unseating are introduced. These bridge retrofits engage multiple potentially vulnerable components in system-level response to mitigate the effects of storm surge and wave loading. In this work, a new systematic method to evaluate the limit state capacity functions based on the post-event global performance of the bridge structure is developed. This method averts the traditional challenge of system abstraction for reliability assessment while also providing

identification of the components that contribute most to different system failure modes. The proposed capacity limit states are not only applicable to hurricane events, but also can be implemented for other hazards that invoke the similar responses in the structure. Moreover, this new conceptualization of the capacity limit state function can be utilized for any natural or man-made hazard, and any structural system.

- The developed methodologies are applied to the Houston/Galveston Bay area bridges to determine the potentially vulnerable structures along the lifeline routes. The vulnerable structures for three different hurricane scenarios are identified. The results show that in a potential hurricane event with 30% stronger wind speed than Hurricane Ike (named as 145 Ike), 19 bridges are highly vulnerable to the deck unseating failure mode. This number increases to 52 for the worst case hurricane scenario, which has the same wind intensity as 145 Ike but the landfall location is shifted to the south of Galveston bay.
- Different retrofit measures, including high strength connections, restrainer cables, and shear keys are applied to two potentially vulnerable bridges from the case study area. The result of this study suggest that shear keys

are the most effective retrofit measures to prevent deck unseating failure mode without increasing the vulnerability of other structural components of coastal bridges.

In summary, the results of this research can lead to a more resilient bridge infrastructure system and safer coastal communities. The outcome of this study is of interest to public officials, to identify critical structures along lifeline routes and plan for risk mitigation strategies. This research can be used to address key stakeholder interests such as pre-event planning and risk mitigation, lifeline evaluation, emergency route identification, retrofit selection and prioritization.

10.2. Recommendations for Future Work

This research initiates the reliability assessment of bridges under different wave and surge loads. Many areas in this work can be extended in future research:

- Probabilistic hazard models for hurricane wave and surge should be developed. A risk assessment framework can be established by integrating the reliability framework presented in this research with the probabilistic hazard model. These hazard models could take into account the effect of climate change that can potentially increase the intensity and frequency of

coastal storms. Also, the impact of sea rise could be considered in a time varying hazard model.

- Other potential failure modes especially in the foundation piling system and abutments should be investigated. There is a potential for scour of bridge foundation under the high water velocity due to hurricane. To perform this research, more advanced models for pile systems including soil-structure interaction are required.
- Some major damages to bridge piers due to the barges impact have been reported in the reconnaissance reports. The impact of floating debris and barges on the response and fragility of the coastal bridges could be examined in future research. Additionally, minor damage states for phenomena such as concrete spalling and tensile cracking could be developed.
- This research considers the as-built condition for coastal bridges. A reasonable follow up of this work is to investigate the effect of aging and deterioration, specifically subsidence and soil erosion.
- More experimental and numerical research on the evaluation of wave and surge loads on coastal bridges is required. The outcome of this research

could be used to develop more accurate wave load models and also to improve the phenomenological wave load model. An additional point of interest is to evaluate the forces from tsunamis.

- Innovative retrofit measures and new materials, such as shape memory alloys, can be implemented to mitigate the hurricane hazard. These mitigation strategies can be compared with the traditional ones that are presented in this research. Also, a cost-benefit analysis for different retrofit measures could be performed as a part of the future research.
- Many of the proposed methodologies seem to be applicable to similar structures such as jetties. Work could examine the reliability of these structures under hurricane events.
- The proposed reliability methods could be coupled with the hurricane wave and surge prediction for a real time risk assessment. This can be extremely beneficial for emergency and recovery activates in hurricane prone areas. The real time assessment can range from simplified inundation maps to a full structural risk assessment.

References

AASHTO. (2008). *Guide Specifications for Bridges Vulnerable to Coastal Storms*, American Association of State Highway and Transportation Officials (AASHTO).

ACI. (2008). *318 - Building code requirement for structural concrete*, American Concrete Institute (ACI).

ADCIRC. (2010). "Coastal Circulation and Storm Surge Model." http://www.adcirc.org.

ADINA. (2010). "ADINA-F Theory and Modeling Guide." Watertown, MA.

ADINA. (2012). "Automatic Dynamic Incremental Nonlinear Analysis." www.adina.com.

API. (2007). *API Recommended Practice for Planning, Designing and Constructing Fixed Offshore Platform*, API Publishing Services, Washington D.C.

Arnold, C. D. (2011). "Multi-Failure Mode Risk Assessment of the Houston/Galveston Bridge System to Hurricane Threats," Master's Thesis, Rice University, Houston, TX.

Ataei, N., Stearns, M. C., and Padgett, J. E. (2010). "Response Sensitivity for Probabilistic Damage Assessment of Coastal Bridges under Surge and Wave Loading." *Transportation Research Record*, 2202 (3), 93-101.

ATC-40. (1997). *Seismic evaluation and retrofit of concrete buildings*, Applied Technology Council, Redwood City, Palo Alto, California.

Basoz, N., and Kiremidjian, A. S. "Development of Empirical Fragility Curves for Bridges." *5th US Conference on Lifeline Earthquake Engineering*, Seattle, WA, USA.

Basoz, N., and Mander, J. (1999). "Enhancement of the Highway Transportation Module in HAZUS." National Institute of Building Sciences, Washington DC.

Bedient, P. B. (2012). "Bedient Research Group." http://bedient.rice.edu/.

Boyle, P., Broadie, M., and Glasserman, P. (1997). "Monte Carlo methods for security pricing." *Journal of Economic Dynamics and Control*, 21(8-9), 1267-1321.

Bradner, C. (2008). "Large-Scale Laboratory Observations of Wave Forces on a Highway Bridge Superstructure," Master's Thesis, Oregon State University, Corvallis, Oregon.

Breiman, L. (2001). "Random Forests." *Machine Learning*, 45(1), 5-32.

Bucher, C. G., and Bourgund, U. (1990). "A fast and efficient response surface approach for structural reliability problems." *Structural Safety*, 7(1), 57-66.

Buhmann, M. D. (2003). *Radial Basis Functions: Theory and Implementations*, Cambridge University Press, London.

Caltrans. (2002). "Seismic Retrofit Program."

Chaplin, J. R. (2012). "Professor John Chaplin Webpage."

Chen, Q., Wang, L., and Xhao, H. (2009). "Hydrodynamic investigation of coastal bridge collapse during Hurricane Katrina." *Journal of Hydraulic Engineering*, 135(3), 175-186.

Chen, Q., Wang, L., Zhao, H., and Douglass, S. L. (2007). "Prediction of storm surges and wind waves on coastal highways in hurricane-prone areas." *Journal of Coastal Research*, 23(5), 1304-1317.

CHG. (2011). "Computational Hydraulics Group." http://users.ices.utexas.edu/~clint/chg_website/index.html.

Choi, E., DesRoches, R., and Nielson, B. (2004). "Seismic fragility of typical bridges in moderate seismic zones." *Engineering Structures*, 26(2), 187-199.

CMI. (2012). " Clay Mathematics Institue." http://www.claymath.org/.

Cortes, C., and Vapnik, V. N. (1995). "Support Vector Networks." *Machine Learning*, 20(3), 273-297.

Cristianini, N., and Shawe-Taylor, J. (2000). *An Introduction to Support Vector Machines and other kernel-based learning methods*, Cambridge University Press, London, UK.

Crossett, K. M., Culliton, T. J., Wiley, P. C., and Goodspeed, T. R. (2004). "Population Trends Along the Coastal United States:1980-2008." National Oceanic and Atmospheric Administration (NOAA).

Cuomo, G., Shimosako, K.-i., and Takahashi, S. (2009). "Wave-in-deck loads on coastal bridges and the role of air." *Coastal Engineering*, 56(8), 793-809.

Currie, I. G. (1974). *Fundamental Mechanics of Fluids*, McGraw-Hill.

Dean, R. G. (1965). "Stream Function Representation of Nonlinear Ocean Waves." *J. Geophys. Res.*, 70(18), 4561-4572.

Dean, R. G., and Dalrymple, R. A. (1984). *Water Wave Mechanics for Engineers and Scientists*, Prentice-Hall, New Jersey.

DesRoches, R., and Muthukumar, S. (2002). "Effect of pounding and restrainers on seismic response of multiple-frame bridges." *Journal of Structural Engineering*, 128(7), 860-869.

DOTD. (2010). "Twin Span Bridge." http://www.twinspanbridge.com/Project_News.htm.

Douglass, S. L., Chen, Q., Olsen, J. M., Edge, B. L., and Brown, D. (2006). "Wave Forces on Bridge Decks." Office of Bridge Technology, Washington, D.C.

Douglass, S. L., Hughes, S. A., Rogers, S., and Chen, Q. J. (2004). "The impact of Hurricane Ivan on the coastal roads of Florida and Alabama: A preliminary report." Coastal transportation engineering research and education center.

Eligehausen, R., Mallee, R., and Silva, J. F. (2006). *Anchorage in concrete construction*, Ernst & Sohn, Berlin.

Ellingwood, B., and Hwang, H. (1985). "Probabilistic descriptions of resistance of safety-related structures in nuclear plants." *Nuclear Engineering and Design*, 88(2), 169-178.

Ellingwood, B. R., and Kinali, K. (2010). "Quantifying and communicating uncertainty in seismic risk assessment." *Structural Safety*, 31, 179-187.

Ellingwood, B. R., and Wen, Y. K. (2005). "Risk-benefit-based design decisions for low-probability/high consequence earthquake events in Mid-America." *Progress in Structural Engineering and Materials*, 7(2), 56-70.

FEMA. (1997). *NEHRP guidelines for seismic rehabilitation of buildings*, Federal Emergency Management Agency, Washington (DC).

FEMA. (2003). *HAZUS-MH MR1: Technical Manual*, Federal Emergency Management Agency, Washington DC.

FEMA, R. V. (2010). "Flood Insurance Study: Coastal Counties, Texas - Intermediate Submission 1: Scoping and Data Review."

Franchin, P., Lupoi, A., Pinto, P. E., and Schotanus, M. I. (2003). "Seismic fragility of reinforced concrete structures using a response surface approach." *Journal of Earthquake Engineering*, 7(sup001), 45-77.

Frangopol, D. M., Kawatani, M., and Kim, C. W. (2007). *Reliability and Optimization of Structural Systems: Assessment, Design, and Life-Cycle Performance*, Taylor & Francis, London, UK.

Gholizadeh, S., and Salajegheh, E. (2010). "Optimal Design of Structures for Earthquake Loading by Self Organizing Radial Basis Function Neural Networks." *Advances in Structural Engineering*, 13(2), 339-356.

Gil-Martín, L. M., Hernández-Montes, E., and Aschheim, M. (2006). "Optimal design of planar frames based on stability criterion using first-order analysis." *Engineering Structures*, 28(13), 1780-1786.

Hastie, T., Tibshirani, R., and Friedman, J. (2009). *The Elements of Statistical Learning: Data Mining, Inference, and Prediction*, Springer, New York, NY.

Hayter, A. J. (2002). *Probability and Statistics for Engineers and Scientists*, Duxbury, Pacific Grove.

Hirt, C. W., and Nichols, B. D. (1981). "Volume of fluid (VOF) method for the dynamics of free boundaries." *Journal of Computational Physics*, 39(1), 201-225.

Holmes, W. T. (2000). "A vision for a complete performance-based earthquake engineering system." 12th World Conference on Earthquake Engineering, Auckland, New Zealand.

Hsu, C.-W., Chang, C.-C., and Lin, C.-J. (2010). "A Practical Guide to Support Vector Classification." Available at http://www.csie.ntu.edu.tw/~cjlin/papers/guide/guide.pdf.

Huang, C. J., and Dong, C. M. (2001). "On a 2-D Numerical Wave Tank in Viscous Fluid." Proceedings of the 11th International Offshore and Polar Engineering Conference, The International Society of Offshore and Polar Engineers, Stavangar, Norway, 148-155.

Huang, W., and Xiao, H. (2009). "Numerical modeling of dynamic wave force acting on Escambia bay bridge deck during Hurricane Ivan." *Journal of Waterway, Port, Coastal and Ocean Engineering*, 135(4), 164-175.

ICF. (2007). "The Potential Impacts of Global Sea Level Rise on Transportation Infrastructure, Phase 1 Final Report: the District of Columbia, Maryland, North Carolina and Virginia." ICF_International.

JCSS. (2001). "JCSS PROBABILISTIC MODEL CODE - PART 3: RESISTANCE MODELS." Joint Committee on Structural Safety.

Jin, J., and Meng, B. (2011). "Computation of wave loads on the superstructures of coastal highway bridges." *Ocean Engineering*, 38(17-18), 2185-2200.

Jin, R., Chen, W., and Simpson, T. W. (2001). "Comparative studies of metamodelling techniques under multiple modelling criteria." *Structural and Multidisciplinary Optimization*, 23(1), 1-13.

Kaplan, P., Murray, J. J., and Yu, W. C. "Theoretical analysis of wave impact forces on platform deck structures." *Proc., Int. Conf. on Offshore Mechanics and Arctic Engineering*, Copenhagen, Denmark.

Karim, K. R., and Yamazaki, F. (2001). "Effect of earthquake ground motions on fragility curves of highway bridge piers based on numerical simulation." *Earthquake Engineering and Structural Dynamics*, 30(12), 1839-1856.

Kennedy, A., Rogers, S., Sallenger, A., Gravois, U., Zachry, B., Dosa, M., and Zarama, F. (2011). "Building Destruction from Waves and Surge on the Bolivar Peninsula during Hurricane Ike." *Journal of Waterway, Port, Coastal, and Ocean Engineering*, 137(3), 132-141.

Kraft, L. M., Jr., Focht, J. A., Jr., and Amerasinghe, S. F. (1981). "Friction Capacity of Piles Driven into Clay." *Journal of the Geotechnical Engineering Division*, 107(11), 1521-1541.

Le Roux, J. P. (2007). "A simple method to determine breaker height and depth for different deepwater wave height/length ratios and sea floor slopes." *Coastal Engineering*, 54(3), 271-277.

Lee, Y.-J., Song, J., Gardoni, P., and Lim, H.-W. (2010). "Post-hazard flow capacity of bridge transportation network considering structural deterioration of bridges." *Structure and Infrastructure Engineering*.

Leet, K., and Bernal, D. (1997). *Reinforced concrete design*, McGraw-Hill Co., New York.

Lewis, D. D., and Gale, W. A. (1994). "A sequential algorithm for training text classifiers." Proceedings of the 17th annual international ACM SIGIR conference on Research and development in information retrieval, Springer-Verlag New York, Inc., Dublin, Ireland, 3-12.

Lo, Z., Haigh, S. K., and Bolton, M. D. (2010). "The Behavior of a Single Pile under Cyclic Axial Loads." Deep foundations and geotechnical in situ testing: GeoShanghai 2010, ASCE, Shanghai, China, 143-148.

Longuet-Higgins, M. S. (1983). "On the Joint Distribution of Wave Periods and Amplitudes in a Random Wave Field." *Proceedings of the Royal Society of London. Series A, Mathematical and Physical Sciences*, 389(1797), 241-258.

Lupoi, G., Franchin, P., Lupoi, A., and Pinto, P. E. (2004). "Seismic fragility analysis of structural systems." 13th World Conference on Earthquake Engineering (13th WCEE), Vancouver, B.C., Canada.

MacGregor, J. G. (1997). *Reinforced concrete: mechanics and design*, Prentice Hall, New Jersy.

Mackie, K. R., and Stojadinović, B. (2005). "Fragility Basis for California Highway Overpass Bridge Seismic Decision Making." *PEER Report 2005/02*, Pacific Earthquake Engineering Research Center, University of California, Berkeley.

Mander, J. B., Priestley, M. J. N., and Park, R. (1988). "Theoretical Stress-Strain Model for Confined Concrete." *Journal of Structural Engineering*, 114(8), 1804-1826.

Marin, J., and Sheppard, D. M. "Storm Surge and Wave Loading on Bridge Superstructures." *Structures Congress 2009*, Austin, Texas, 62-72.

Massel, S. R. (1996). *Ocean surface Waves: Their Physics and Prediction*, World Scientific Publishing Co.

MathWorks, T. (2004). "Matlab ", http://www.mathworks.com/, Natick, MA.

McKay, M. D., Beckman, R. J., and Conover, W. J. (1979). "A Comparison of Three Methods for Selecting Values of Input Variables in the Analysis of Output from a Computer Code." *Technometrics*, 21, 239-245.

McPherson, R. L. (2008). "Hurricane Induced Wave and Surge Forces on Bridge Decks," MS Thesis, Texas A&M University, College Station, Texas.

Meng, B., and Jin, J. (2007). "Uplift Wave Load on the Superstructure of Coastal Bridges." Structures Congress: New Horizons and Better Practices, Long Beach, California, USA.

Mohle, J., and Kunnath, S. (2006). "Reinforcing Steel Material." OpenSees User's Manual, www.opensees.berkeley.edu.

Morison, J. R., O'Brien, M. P., Johnson, J. W., and Schaaf, S. A. (1950). "The force exerted by surface waves on piles." *Journal of Petroleum. Technology*, 189, 149-154.

Mosqueda, G., Porter, K. A., O'Connor, J., and McAnany, P. (2007). "Damage to Engineered Buildings and Bridges in the Wake of Hurricane Katrina." Forensic Engineering Symposium, ASCE, Long Beach, California, USA, 4-14.

NBI. (2010). "National Bridge Inventory Database."

Neter, J., Kutner, M. H., Nachstheim, C. J., and Wasserman, W. (1996). *Applied Linear Statistical Models*, McGraw-Hill, Boston, MA.

Nielson, B., and DesRoches, R. (2007). "Seismic fragility curves for typical highway bridge classes in the central and southeastern United States." *Earthquake Spectra*, 23, 615-633.

Nielson, B. G. (2005). "Analytical Fragility Curves for Highway Bridges in Moderate Seismic Zones," Doctor of Philosophy Dissertation, Georgia Institute of Technology, Atlanta, Georgia.

NIST. (2006). "Performance of Physical Structures in Hurricane Katrina and Hurricane Rita: A Reconnaissance Report."

NOAA. (2010). "National Data Buoy Center." http://www.ndbc.noaa.gov/.

Okada, S., Mitamura, H., and Ishikawa, H. (2006). "The collapse mechanism and the temporary restoration of Omori Bridge damaged by the storm surge of Typhoon No. 18 in 2004." *Technical Memorandum of Public Works Research Institute*, 4009, 185-192.

Okeil, A. M., and Cai, C. S. (2008). "Survey of short- and medium-span bridge damage induced by Hurricane Katrina." *Journal of Bridge Engineering*, 13(4), 377-387.

OpenSees. (2012). "Open Source earthquake engineering system."

Ott, R. L., and Longnecker, M. (1993). *An introduction to statistical methods and data analysis*, Duxbury Press, Belmont, CA.

Padgett, J., Desroches, R., Nielson, B., Yashinsky, M., Kwon, O.-S., Burdette, N., and Tavera, E. (2008). "Bridge damage and repair costs from Hurricane Katrina." *Journal of Bridge Engineering*, 13(1), 6-14.

Padgett, J. E. (2007). "Seismic Vulnerability Assessment of Retrofitted Bridges Using Probabilistic Methods," Georgia Institute of Technology.

Padgett, J. E., and Desroches, R. (2007). "Sensitivity of Seismic Response and Fragility to Parameter Uncertainty." *Journal of Structural Engineering*, 133(12), 1710-1718.

Padgett, J. E., and DesRoches, R. (2009). "Retrofitted bridge fragility analysis for typical classes of multispan bridges." *Earthquake Spectra*, 25(1), 117-141.

Padgett, J. E., Spiller, A., and Arnold, C. (2009). "Statistical analysis of coastal bridge vulnerability based on empirical evidence from Hurricane Katrina." *Structure and Infrastructure Engineering*.

Palei, S. K., and Das, S. K. (2009). "Logistic regression model for prediction of roof fall risks in bord and pillar workings in coal mines: An approach." *Safety Science*, 47(1), 88-96.

Pan, Y., Agrawal, A. K., and Ghosn, M. (2007). "Seismic Fragility of Continuous Steel Highway Bridges in New York State." *Journal of Bridge Engineering*, 12(6), 689-699.

Picarda, R. R., and Cook, R. D. (1984). "Cross-Validation of Regression Models." *Journal of the American Statistical Association*, 79(387), 575-583.

Priestley, M. J. N., Seible, F., and Calvi, G. M. (1996). *Seismic Design and Retrofit of Bridges*, John Wiley & Sons, New York, NY.

Prinzie, A., and Van den Poel, D. (2008). "Random Forests for multiclass classification: Random MultiNomial Logit." *Expert Systems with Applications*, 34(3), 1721-1732.

Rajashekhar, M. R., and Ellingwood, B. R. (1993). "A new look at the response surface approach for reliability analysis." *Structural Safety*, 12(3), 205-220.

Rees, S. (2010). "Mississippi Coastal Improvement." SSPEED Conference, Rice University, Houston, TX.

Ren, W.-X., and Chen, H.-B. (2010). "Finite element model updating in structural dynamics by using the response surface method." *Engineering Structures*, 32(8), 2455-2465.

Robertson, I. N., Riggs, H. R., Yim, S. C. S., and Young, Y. L. (2007). "Lessons from Hurricane Katrina Storm Surge on Bridges and Buildings." *Journal of Waterway, Port, Coastal, and Ocean Engineering*, 133(6), 463-483.

Rosa, R. M. S. (2006). "Turbulence Theories." *Encyclopedia of Mathematical Physics*, 5, 292-302.

Sawyer, A. D. (2008). "Determination of hurricane surge wave forces on bridge superstructures and design/retrofit options to mitigate or sustain these forces," Master of Science, Auburn University, Auburn, AL.

Schumacher, T., Higgins, C., Bradner, C., Cox, D., and Yim, S. C. (2008). "Large-Scale Wave Flume Experiments on Highway Bridge Superstructures Exposed to Hurricane Wave Forces." The Sixth National Seismic Conference on Bridges & Highways, Charleston, South Carolina.

Schumacher, T., Higgins, C., Cox, D., and Bradner, C. (2012). "PREDICTION OF FORCES ON COASTAL HIGHWAY BRIDGES CAUSED BY HURRICANE- INDUCED WAVES BASED ON LARGE-SCALE EXPERIMENTAL OBSERVATIONS " ATC-SEI Advances in Hurricane Engineering, Miami, FL.

Seo, J., Dueñas-Osorio, L., Craig, J. I., and Goodno, B. J. (2012). "Metamodel-based regional vulnerability estimate of irregular steel moment-frame structures subjected to earthquake events." *Engineering Structures*, 45, 585-597.

Sheppard, D. M., and Marin, J. (2009). "Wave loading on Bridge Decks." Florida Department of Transportation, Tallahassee, Florida.

Shinozuka, M., Feng, M. Q., Kim, H.-K., and Kim, S.-H. (2000). "Nonlinear Static Procedure for Fragility Curve Development." *Journal of Engineering Mechanics*, 126(12), 1287-1295.

Simpson, T. W., Poplinski, J. D., Koch, P. N., and Allen, J. K. (2001). "Metamodels for computer-based engineering design: survey and recommendations." *Engineering with computers*, 17(2), 129-150.

Sorenson, R. M. (1993). *Basic Wave Mechanics: for coastal and ocean engineering*, John Wiley & Sons.

Stearns, M., and Padgett, J. (2010). "Impact of 2008 Hurricane Ike on Bridge Infrastructure in the Houston/Galveston Region." *ASCE Journal of Performance of Constructed Facilities* (doi:10.1061/(ASCE)CF.1943-5509.0000213).

Strano, M., and Colosimo, B. M. (2006). "Logistic regression analysis for experimental determination of forming limit diagrams." *International Journal of Machine Tools and Manufacture*, 46(6), 673-682.

SWAN. (2010). "Simulating WAVes Nearshore." www.swan.tudelft.nl.

Wriggers, P. (2008). *Nonlinear Finite Element Methods*, Springer, Berlin, Germany.

Xu, F., Perrie, W., Toulany, B., and Smith, P. C. (2007). "Wind-generated waves in Hurricane Juan." *Ocean Modelling*, 16(3-4), 188-205.

Zamora, N. A., Cook, R. A., Konz, R. C., and Consolazio, G. R. (2003). "Behavior and Design of Single, Headed and Unheaded, Grouted Anchors under Tensile Load." *ACI Structural Journal*, 100(2), 222-230.

Zhang, Y. (2006). "Probabilistic structural seismic performance assessment methodology and application to an actual bridge-foundation-ground system," Ph.D. dissertation, University of California, San Diego, San Diego.

Appendix I
Wave Loads Experimental Test Data

This appendix provides the experimental test data that are used to evaluate the bias removal functions (presented in Chapter 3). Table I-1 and

Table I-2 present the experimental test data extracted from Bradner (2008) and Sheppard and Marin (2009) respectively.

Table I-1. Experimental test data from Bradner (2008).

W (m)	d_g (m)	d_b (m)	d_s (m)	Z_c (m)	T_p (s)	H (m)	F_V (N)
1.94	0.23	0.05	1.61	0.28	2.5	0.54	2.01
1.94	0.23	0.05	1.61	0.28	2.5	0.57	1.74
1.94	0.23	0.05	1.61	0.28	2.5	0.68	4.36
1.94	0.23	0.05	1.61	0.28	2.5	0.71	4.63
1.94	0.23	0.05	1.61	0.28	3	0.49	0.84
1.94	0.23	0.05	1.61	0.28	3	0.62	3.73
1.94	0.23	0.05	1.61	0.28	3	0.78	11.69
1.94	0.23	0.05	1.61	0.28	3.5	0.48	0.91
1.94	0.23	0.05	1.61	0.28	3.5	0.73	5.71
1.94	0.23	0.05	1.61	0.28	3.5	0.98	10.92
1.94	0.23	0.05	1.61	0.28	4	0.48	0.62
1.94	0.23	0.05	1.61	0.28	4	0.7	6.52
1.94	0.23	0.05	1.61	0.28	4	0.84	15.64
1.94	0.23	0.05	1.61	0.28	4.5	0.5	1.28
1.94	0.23	0.05	1.61	0.28	4.5	0.73	16.59
1.94	0.23	0.05	1.61	0.28	4.5	0.84	24.07
1.94	0.23	0.05	1.75	0.14	2	0.44	2.9
1.94	0.23	0.05	1.75	0.14	2	0.49	3.63
1.94	0.23	0.05	1.75	0.14	2	0.58	5.4
1.94	0.23	0.05	1.75	0.14	2.5	0.42	3.52
1.94	0.23	0.05	1.75	0.14	2.5	0.52	5.49
1.94	0.23	0.05	1.75	0.14	2.5	0.61	7.96
1.94	0.23	0.05	1.75	0.14	2.5	0.79	13.24
1.94	0.23	0.05	1.75	0.14	3	0.43	6.03

W (m)	d_g (m)	d_b (m)	d_s (m)	Z_c (m)	T_p (s)	H (m)	F_V (N)
1.94	0.23	0.05	1.75	0.14	3	0.53	9.96
1.94	0.23	0.05	1.75	0.14	3	0.63	13.173
1.94	0.23	0.05	1.75	0.14	3	0.68	15.69
1.94	0.23	0.05	1.75	0.14	3	0.81	17.31
1.94	0.23	0.05	1.75	0.14	3.5	0.51	3.94
1.94	0.23	0.05	1.75	0.14	3.5	0.58	11.06
1.94	0.23	0.05	1.75	0.14	3.5	0.73	15.79
1.94	0.23	0.05	1.75	0.14	3.5	0.94	20.51
1.94	0.23	0.05	1.75	0.14	4	0.48	3.35
1.94	0.23	0.05	1.75	0.14	4	0.68	11.33
1.94	0.23	0.05	1.75	0.14	4	0.81	19.29
1.94	0.23	0.05	1.75	0.14	4.5	0.5	3.35
1.94	0.23	0.05	1.75	0.14	4.5	0.72	16.82
1.94	0.23	0.05	1.75	0.14	4.5	0.86	25.26
1.94	0.23	0.05	1.89	0	2	0.21	3.16
1.94	0.23	0.05	1.89	0	2	0.32	7.9
1.94	0.23	0.05	1.89	0	2	0.41	10.2
1.94	0.23	0.05	1.89	0	2	0.5	11.32
1.94	0.23	0.05	1.89	0	2	0.58	13.25
1.94	0.23	0.05	1.89	0	2	0.63	14.39
1.94	0.23	0.05	1.89	0	2.5	0.2	3.82
1.94	0.23	0.05	1.89	0	2.5	0.32	6.58
1.94	0.23	0.05	1.89	0	2.5	0.41	11.01
1.94	0.23	0.05	1.89	0	2.5	0.5	13.63
1.94	0.23	0.05	1.89	0	2.5	0.63	20.19
1.94	0.23	0.05	1.89	0	2.5	0.82	26.43
1.94	0.23	0.05	1.89	0	3	0.2	3.38
1.94	0.23	0.05	1.89	0	3	0.32	6.44
1.94	0.23	0.05	1.89	0	3	0.41	10.92
1.94	0.23	0.05	1.89	0	3	0.5	16.58
1.94	0.23	0.05	1.89	0	3	0.61	22.59
1.94	0.23	0.05	1.89	0	3	0.83	30.71
1.94	0.23	0.05	1.89	0	3.5	0.23	3.97
1.94	0.23	0.05	1.89	0	3.5	0.5	11.54
1.94	0.23	0.05	1.89	0	3.5	0.59	14.01
1.94	0.23	0.05	1.89	0	3.5	0.72	18.01
1.94	0.23	0.05	1.89	0	3.5	0.91	29.2
1.94	0.23	0.05	1.89	0	4	0.23	4.08
1.94	0.23	0.05	1.89	0	4	0.46	8.82
1.94	0.23	0.05	1.89	0	4	0.66	15.09

W (m)	d_g (m)	d_b (m)	d_s (m)	Z_c (m)	T_p (s)	H (m)	F_V (N)
1.94	0.23	0.05	1.89	0	4	0.86	19
1.94	0.23	0.05	1.89	0	4.5	0.23	11.37
1.94	0.23	0.05	1.89	0	4.5	0.71	16.6
1.94	0.23	0.05	1.89	0	4.5	0.85	19
1.94	0.23	0.05	2.03	-0.14	2	0.32	4.25
1.94	0.23	0.05	2.03	-0.14	2	0.41	7.57
1.94	0.23	0.05	2.03	-0.14	2	0.54	16.57
1.94	0.23	0.05	2.03	-0.14	2.5	0.32	5.77
1.94	0.23	0.05	2.03	-0.14	2.5	0.44	9.38
1.94	0.23	0.05	2.03	-0.14	2.5	0.68	17.29
1.94	0.23	0.05	2.03	-0.14	2.5	0.79	23.8
1.94	0.23	0.05	2.03	-0.14	3	0.33	7.23
1.94	0.23	0.05	2.03	-0.14	3	0.42	12.28
1.94	0.23	0.05	2.03	-0.14	3	0.6	19.72
1.94	0.23	0.05	2.03	-0.14	3	0.79	34.32
1.94	0.23	0.05	2.03	-0.14	3.5	0.49	14.14
1.94	0.23	0.05	2.03	-0.14	3.5	0.68	31.24
1.94	0.23	0.05	2.03	-0.14	3.5	0.9	41.6
1.94	0.23	0.05	2.03	-0.14	4	0.48	13.39
1.94	0.23	0.05	2.03	-0.14	4	0.71	18.75
1.94	0.23	0.05	2.03	-0.14	4	0.86	23.91
1.94	0.23	0.05	2.03	-0.14	4.5	0.48	17.1
1.94	0.23	0.05	2.03	-0.14	4.5	0.68	19.5
1.94	0.23	0.05	2.03	-0.14	4.5	0.83	23.33
1.94	0.23	0.05	2.17	-0.28	2	0.31	4.15
1.94	0.23	0.05	2.17	-0.28	2	0.41	5.16
1.94	0.23	0.05	2.17	-0.28	2	0.46	6.18
1.94	0.23	0.05	2.17	-0.28	2	0.54	7.28
1.94	0.23	0.05	2.17	-0.28	2.5	0.31	4.52
1.94	0.23	0.05	2.17	-0.28	2.5	0.41	5.62
1.94	0.23	0.05	2.17	-0.28	2.5	0.5	8.9
1.94	0.23	0.05	2.17	-0.28	2.5	0.56	8.31
1.94	0.23	0.05	2.17	-0.28	3	0.33	6.2
1.94	0.23	0.05	2.17	-0.28	3	0.42	7.61
1.94	0.23	0.05	2.17	-0.28	3	0.51	9.6
1.94	0.23	0.05	2.17	-0.28	3	0.56	10.5
1.94	0.23	0.05	2.17	-0.28	3.5	0.47	10.4
1.94	0.23	0.05	2.17	-0.28	3.5	0.61	13.38
1.94	0.23	0.05	2.17	-0.28	4	0.47	10.57

W (m)	d_g (m)	d_b (m)	d_s (m)	Z_c (m)	T_p (s)	H (m)	F_V (N)
1.94	0.23	0.05	2.17	-0.28	4	0.64	14.28
1.94	0.23	0.05	2.17	-0.28	4.5	0.47	12.45
1.94	0.23	0.05	2.17	-0.28	4.5	0.62	17.46

Table I-2. Experimental test data from Sheppard and Marin (2009).

W (ft)	d_g (ft)	d_b (ft)	d_s (ft)	Z_c (ft)	T_p (s)	λ (ft)	H (ft)	F_V (lb)
4	0.5	0.083333	1.42	0.17	3.5	22.93	0.77	134.92
4	0.5	0.083333	1.42	0.17	3.5	22.93	0.45	61.48
4	0.5	0.083333	1.42	0.17	3	19.59	0.75	89.51
4	0.5	0.083333	1.42	0.17	3	19.59	0.48	86.36
4	0.5	0.083333	1.42	0.17	2.5	16.1	0.86	138.2
4	0.5	0.083333	1.42	0.17	2.5	16.1	0.64	71.77
4	0.5	0.083333	1.42	0.17	2	12.53	0.71	119.09
4	0.5	0.083333	1.42	0.17	2	12.53	0.59	48.98
4	0.5	0.083333	1.42	0.17	1.5	8.82	0.76	99.5
4	0.5	0.083333	1.42	0.17	1.5	8.82	0.79	86.25
4	0.5	0.083333	1.58	0	3.5	24.24	1.01	159.69
4	0.5	0.083333	1.58	0	3.5	24.24	0.64	109.95
4	0.5	0.083333	1.58	0	3	20.64	0.75	237.74
4	0.5	0.083333	1.58	0	3	20.64	0.55	194.99
4	0.5	0.083333	1.58	0	2.5	16.92	1.04	199.44
4	0.5	0.083333	1.58	0	2.5	16.92	0.71	158.43
4	0.5	0.083333	1.58	0	2	13.12	0.66	245.97
4	0.5	0.083333	1.58	0	2	13.12	0.55	153.99
4	0.5	0.083333	1.58	0	1.5	9.17	0.76	214.95
4	0.5	0.083333	1.58	0	1.5	9.17	0.84	176.06
4	0.5	0.083333	1.88	-0.29	3.5	26.31	0.79	129.01
4	0.5	0.083333	1.88	-0.29	3.5	26.31	0.64	100.05
4	0.5	0.083333	1.88	-0.29	3	22.31	0.54	126.55
4	0.5	0.083333	1.88	-0.29	3	22.31	0.42	93.46
4	0.5	0.083333	1.88	-0.29	2.5	18.23	0.92	125.82
4	0.5	0.083333	1.88	-0.29	2.5	18.23	0.87	125.27
4	0.5	0.083333	1.88	-0.29	2	14.05	0.82	123.6
4	0.5	0.083333	1.88	-0.29	2	14.05	0.56	101.28
4	0.5	0.083333	1.88	-0.29	1.5	9.67	0.81	113.19
4	0.5	0.083333	1.88	-0.29	1.5	9.67	0.77	131.02
4	0.5	0.083333	2.21	-0.63	3.5	28.41	1.14	113.66
4	0.5	0.083333	2.21	-0.63	3.5	28.41	0.65	57.77

W (ft)	d_g (ft)	d_b (ft)	d_s (ft)	Z_c (ft)	T_p (s)	λ (ft)	H (ft)	F_V (lb)
4	0.5	0.083333	2.21	-0.63	3	24.02	0.72	101.49
4	0.5	0.083333	2.21	-0.63	3	24.02	0.53	62.26
4	0.5	0.083333	2.21	-0.63	2.5	19.55	0.85	91.19
4	0.5	0.083333	2.21	-0.63	2.5	19.55	0.69	64.48
4	0.5	0.083333	2.21	-0.63	2	14.96	0.77	75.88
4	0.5	0.083333	2.21	-0.63	2	14.96	0.77	71.89
4	0.5	0.083333	2.21	-0.63	1.5	10.13	0.94	84.16
4	0.5	0.083333	2.21	-0.63	1.5	10.13	0.9	71.81
4	0.5	0.083333	1.75	0.17	3.5	25.45	0.65	94.83
4	0.5	0.083333	1.75	0.17	3.5	25.45	0.72	132.89
4	0.5	0.083333	1.75	0.17	3	21.62	0.61	121.57
4	0.5	0.083333	1.75	0.17	3	21.62	0.58	100
4	0.5	0.083333	1.75	0.17	2.5	17.69	0.85	140.28
4	0.5	0.083333	1.75	0.17	2.5	17.69	0.68	123.77
4	0.5	0.083333	1.75	0.17	2	13.67	0.78	100.1
4	0.5	0.083333	1.75	0.17	2	13.67	0.81	166.78
4	0.5	0.083333	1.75	0.17	1.5	9.47	0.79	129.69
4	0.5	0.083333	1.75	0.17	1.5	9.47	0.81	122.79
4	0.5	0.083333	1.92	0	3.5	26.59	0.86	167.44
4	0.5	0.083333	1.92	0	3.5	26.59	0.58	82.52
4	0.5	0.083333	1.92	0	3	22.54	0.71	253.15
4	0.5	0.083333	1.92	0	3	22.54	0.53	193.28
4	0.5	0.083333	1.92	0	2.5	18.4	0.83	244.98
4	0.5	0.083333	1.92	0	2.5	18.4	0.71	182.19
4	0.5	0.083333	1.92	0	2	14.17	0.84	271.43
4	0.5	0.083333	1.92	0	2	14.17	0.91	259.62
4	0.5	0.083333	1.92	0	1.5	9.74	0.8	213.21
4	0.5	0.083333	1.92	0	1.5	9.74	0.69	182.97
4	0.5	0.083333	2.21	-0.29	3.5	28.41	0.8	141.62
4	0.5	0.083333	2.21	-0.29	3.5	28.41	0.62	100.51
4	0.5	0.083333	2.21	-0.29	3	24.02	0.64	148.43
4	0.5	0.083333	2.21	-0.29	3	24.02	0.48	115.34
4	0.5	0.083333	2.21	-0.29	2.5	19.55	0.88	129.38
4	0.5	0.083333	2.21	-0.29	2.5	19.55	0.82	113.64
4	0.5	0.083333	2.21	-0.29	2	14.96	1.12	127.71
4	0.5	0.083333	2.21	-0.29	2	14.96	0.99	123.85
4	0.5	0.083333	2.21	-0.29	1.5	10.13	0.91	167.65
4	0.5	0.083333	2.21	-0.29	1.5	10.13	0.85	132.61
4	0.5	0.083333	2.54	-0.63	3.5	30.31	1.06	96.26
4	0.5	0.083333	2.54	-0.63	3.5	30.31	0.79	77.57

W (ft)	d_g (ft)	d_b (ft)	d_s (ft)	Z_c (ft)	T_p (s)	λ (ft)	H (ft)	F_V (lb)
4	0.5	0.083333	2.54	-0.63	3	25.57	0.94	109.11
4	0.5	0.083333	2.54	-0.63	3	25.57	0.62	84.41
4	0.5	0.083333	2.54	-0.63	2.5	20.73	0.8	104.2
4	0.5	0.083333	2.54	-0.63	2.5	20.73	0.65	60.22
4	0.5	0.083333	2.54	-0.63	2	15.74	1.42	100.67
4	0.5	0.083333	2.54	-0.63	2	15.74	0.96	74.13
4	0.5	0.083333	2.54	-0.63	1.5	10.48	1.03	109.77
4	0.5	0.083333	2.54	-0.63	1.5	10.48	1.02	106.09
4	0.5	0.083333	2.08	-0.17	3.5	27.65	0.83	195.75
4	0.5	0.083333	2.08	-0.17	3.5	27.65	0.53	70.43
4	0.5	0.083333	2.08	-0.17	3	23.4	0.92	176.96
4	0.5	0.083333	2.08	-0.17	3	23.4	0.52	72.41
4	0.5	0.083333	2.08	-0.17	2.5	19.08	0.86	158.7
4	0.5	0.083333	2.08	-0.17	2.5	19.08	0.64	81.39
4	0.5	0.083333	2.08	-0.17	2	14.63	0.89	173.22
4	0.5	0.083333	2.08	-0.17	2	14.63	0.75	142.16
4	0.5	0.083333	2.08	-0.17	1.5	9.97	0.91	133.49
4	0.5	0.083333	2.08	-0.17	1.5	9.97	0.81	126.7
4	0.5	0.083333	2.25	0	3.5	28.66	1.07	141.6
4	0.5	0.083333	2.25	0	3.5	28.66	0.71	131.95
4	0.5	0.083333	2.25	0	3	24.23	0.87	307.08
4	0.5	0.083333	2.25	0	3	24.23	0.6	222.8
4	0.5	0.083333	2.25	0	2.5	19.71	1.01	264.39
4	0.5	0.083333	2.25	0	2.5	19.71	0.86	201.26
4	0.5	0.083333	2.25	0	2	15.06	1.04	276.31
4	0.5	0.083333	2.25	0	2	15.06	0.9	266.12
4	0.5	0.083333	2.25	0	1.5	10.18	1.01	285.11
4	0.5	0.083333	2.25	0	1.5	10.18	0.96	242.84
4	0.5	0.083333	2.54	-0.29	3.5	30.31	1.14	175.29
4	0.5	0.083333	2.54	-0.29	3.5	30.31	0.69	103.2
4	0.5	0.083333	2.54	-0.29	3	25.57	0.92	150.8
4	0.5	0.083333	2.54	-0.29	3	25.57	0.6	106.55
4	0.5	0.083333	2.54	-0.29	2.5	20.73	1.03	177.69
4	0.5	0.083333	2.54	-0.29	2.5	20.73	0.72	108.15
4	0.5	0.083333	2.54	-0.29	2	15.74	1.28	199.86
4	0.5	0.083333	2.54	-0.29	2	15.74	1.02	115.77
4	0.5	0.083333	2.54	-0.29	1.5	10.48	1.08	143.13
4	0.5	0.083333	2.54	-0.29	1.5	10.48	1.07	145.11
4	0.5	0.083333	2.88	-0.63	3.5	32.05	1.11	93.45
4	0.5	0.083333	2.88	-0.63	3.5	32.05	0.75	69.03

W (ft)	d_g (ft)	d_b (ft)	d_s (ft)	Z_c (ft)	T_p (s)	λ (ft)	H (ft)	F_V (lb)
4	0.5	0.083333	2.88	-0.63	3	26.97	1.05	118.44
4	0.5	0.083333	2.88	-0.63	3	26.97	0.78	82.36
4	0.5	0.083333	2.88	-0.63	2.5	21.78	0.94	108.51
4	0.5	0.083333	2.88	-0.63	2.5	21.78	0.61	67.11
4	0.5	0.083333	2.88	-0.63	2	16.41	1.56	97.91
4	0.5	0.083333	2.88	-0.63	2	16.41	1.35	93.13
4	0.5	0.083333	2.88	-0.63	1.5	10.76	1.28	124.76
4	0.5	0.083333	2.88	-0.63	1.5	10.76	1.09	69.96
4	0.5	0.083333	2.42	-0.17	3.5	29.62	0.85	123.77
4	0.5	0.083333	2.42	-0.17	3.5	29.62	0.57	73.78
4	0.5	0.083333	2.42	-0.17	3	25.01	0.82	202.88
4	0.5	0.083333	2.42	-0.17	3	25.01	0.63	145.12
4	0.5	0.083333	2.42	-0.17	2.5	20.3	1.05	236.5
4	0.5	0.083333	2.42	-0.17	2.5	20.3	0.72	111.44
4	0.5	0.083333	2.42	-0.17	2	15.46	1.19	189.8
4	0.5	0.083333	2.42	-0.17	2	15.46	0.98	179.99
4	0.5	0.083333	2.42	-0.17	1.5	10.36	1.1	170.61
4	0.5	0.083333	2.42	-0.17	1.5	10.36	1.05	123.36
4	0.5	0.083333	2.58	0	3.5	30.54	0.82	156.94
4	0.5	0.083333	2.58	0	3.5	30.54	0.63	98.09
4	0.5	0.083333	2.58	0	3	25.75	0.86	252.65
4	0.5	0.083333	2.58	0	3	25.75	0.55	185.75
4	0.5	0.083333	2.58	0	2.5	20.87	1.04	323.82
4	0.5	0.083333	2.58	0	2.5	20.87	0.78	204.78
4	0.5	0.083333	2.58	0	2	15.83	1.23	263.28
4	0.5	0.083333	2.58	0	2	15.83	1.14	227.56
4	0.5	0.083333	2.58	0	1.5	10.52	1.03	232.95
4	0.5	0.083333	2.58	0	1.5	10.52	1.01	239.81
4	0.5	0.083333	2.88	-0.29	3.5	32.05	1.2	157.31
4	0.5	0.083333	2.88	-0.29	3.5	32.05	0.78	96.76
4	0.5	0.083333	2.88	-0.29	3	26.97	1.04	151.4
4	0.5	0.083333	2.88	-0.29	3	26.97	0.81	118.61
4	0.5	0.083333	2.88	-0.29	2.5	21.78	0.97	193.91
4	0.5	0.083333	2.88	-0.29	2.5	21.78	0.63	129.62
4	0.5	0.083333	2.88	-0.29	2	16.41	1.64	241.72
4	0.5	0.083333	2.88	-0.29	2	16.41	1.39	137.61
4	0.5	0.083333	2.88	-0.29	1.5	10.76	1.2	133.33
4	0.5	0.083333	2.88	-0.29	1.5	10.76	1.11	139.93
4	0.5	0.083333	1.42	0.17	3.5	22.93	0.92	35.53
4	0.5	0.083333	1.42	0.17	3.5	22.93	0.58	87.13

W (ft)	d_g (ft)	d_b (ft)	d_s (ft)	Z_c (ft)	T_p (s)	λ (ft)	H (ft)	F_V (lb)
4	0.5	0.083333	1.42	0.17	3	19.59	0.73	4.08
4	0.5	0.083333	1.42	0.17	3	19.59	0.63	52.09
4	0.5	0.083333	1.42	0.17	2.5	16.1	0.86	43.59
4	0.5	0.083333	1.42	0.17	2.5	16.1	0.81	94.08
4	0.5	0.083333	1.42	0.17	2	12.53	0.69	7.06
4	0.5	0.083333	1.42	0.17	2	12.53	0.63	53.97
4	0.5	0.083333	1.42	0.17	1.5	8.82	0.84	35.51
4	0.5	0.083333	1.42	0.17	1.5	8.82	0.72	69.66
4	0.5	0.083333	1.58	0	3.5	24.24	0.74	107.4
4	0.5	0.083333	1.58	0	3.5	24.24	0.59	245.83
4	0.5	0.083333	1.58	0	3	20.64	0.68	81.52
4	0.5	0.083333	1.58	0	3	20.64	0.46	307.99
4	0.5	0.083333	1.58	0	2.5	16.92	1.11	177.28
4	0.5	0.083333	1.58	0	2.5	16.92	0.79	255.79
4	0.5	0.083333	1.58	0	2	13.12	0.69	166.11
4	0.5	0.083333	1.58	0	2	13.12	0.58	237.5
4	0.5	0.083333	1.58	0	1.5	9.17	0.8	165.28
4	0.5	0.083333	1.58	0	1.5	9.17	0.73	241.31
4	0.5	0.083333	1.88	-0.29	3.5	26.31	1.22	103.13
4	0.5	0.083333	1.88	-0.29	3.5	26.31	0.65	205.82
4	0.5	0.083333	1.88	-0.29	3	22.31	0.59	94.48
4	0.5	0.083333	1.88	-0.29	3	22.31	0.45	205.49
4	0.5	0.083333	1.88	-0.29	2.5	18.23	1.03	105.72
4	0.5	0.083333	1.88	-0.29	2.5	18.23	0.67	176.52
4	0.5	0.083333	1.88	-0.29	2	14.05	0.78	106.92
4	0.5	0.083333	1.88	-0.29	2	14.05	0.56	197.51
4	0.5	0.083333	1.88	-0.29	1.5	9.67	0.85	161.74
4	0.5	0.083333	1.88	-0.29	1.5	9.67	0.69	253.49
4	0.5	0.083333	2.21	-0.63	3.5	28.41	0.96	68.44
4	0.5	0.083333	2.21	-0.63	3.5	28.41	0.67	112.38
4	0.5	0.083333	2.21	-0.63	3	24.02	0.7	69.06
4	0.5	0.083333	2.21	-0.63	3	24.02	0.45	144.9
4	0.5	0.083333	2.21	-0.63	2.5	19.55	1.02	83.51
4	0.5	0.083333	2.21	-0.63	2.5	19.55	0.82	127.52
4	0.5	0.083333	2.21	-0.63	2	14.96	0.82	79.89
4	0.5	0.083333	2.21	-0.63	2	14.96	0.71	145.38
4	0.5	0.083333	2.21	-0.63	1.5	10.13	0.9	155.11
4	0.5	0.083333	2.21	-0.63	1.5	10.13	0.85	221.1
4	0.5	0.083333	1.75	0.17	3.5	25.45	0.95	27.18
4	0.5	0.083333	1.75	0.17	3.5	25.45	0.54	164.9

W (ft)	d_g (ft)	d_b (ft)	d_s (ft)	Z_c (ft)	T_p (s)	λ (ft)	H (ft)	F_V (lb)
4	0.5	0.083333	1.75	0.17	3	21.62	0.77	23.76
4	0.5	0.083333	1.75	0.17	3	21.62	0.47	181.01
4	0.5	0.083333	1.75	0.17	2.5	17.69	0.95	48.19
4	0.5	0.083333	1.75	0.17	2.5	17.69	0.63	141.37
4	0.5	0.083333	1.75	0.17	2	13.67	0.77	53.84
4	0.5	0.083333	1.75	0.17	2	13.67	0.7	121.06
4	0.5	0.083333	1.75	0.17	1.5	9.47	0.86	72.01
4	0.5	0.083333	1.75	0.17	1.5	9.47	0.75	122.9
4	0.5	0.083333	1.92	0	3.5	26.59	1.02	122.97
4	0.5	0.083333	1.92	0	3.5	26.59	0.5	329.96
4	0.5	0.083333	1.92	0	3	22.54	0.6	126.61
4	0.5	0.083333	1.92	0	3	22.54	0.39	242.46
4	0.5	0.083333	1.92	0	2.5	18.4	0.86	153.61
4	0.5	0.083333	1.92	0	2.5	18.4	0.66	238.45
4	0.5	0.083333	1.92	0	2	14.17	0.63	177.84
4	0.5	0.083333	1.92	0	2	14.17	0.46	323.21
4	0.5	0.083333	1.92	0	1.5	9.74	0.77	224.7
4	0.5	0.083333	1.92	0	1.5	9.74	0.64	259.98
4	0.5	0.083333	2.21	-0.29	3.5	28.41	0.79	102.68
4	0.5	0.083333	2.21	-0.29	3.5	28.41	0.46	192.49
4	0.5	0.083333	2.21	-0.29	3	24.02	0.73	88.77
4	0.5	0.083333	2.21	-0.29	3	24.02	0.44	205.98
4	0.5	0.083333	2.21	-0.29	2.5	19.55	0.92	119.12
4	0.5	0.083333	2.21	-0.29	2.5	19.55	0.66	209.04
4	0.5	0.083333	2.21	-0.29	2	14.96	0.95	159.81
4	0.5	0.083333	2.21	-0.29	2	14.96	0.65	253.5
4	0.5	0.083333	2.21	-0.29	1.5	10.13	0.83	293.58
4	0.5	0.083333	2.21	-0.29	1.5	10.13	0.65	286.83
4	0.5	0.083333	2.54	-0.63	3.5	30.31	1.33	79.21
4	0.5	0.083333	2.54	-0.63	3.5	30.31	0.72	131.99
4	0.5	0.083333	2.54	-0.63	3	25.57	0.92	91.2
4	0.5	0.083333	2.54	-0.63	3	25.57	0.62	130.73
4	0.5	0.083333	2.54	-0.63	2.5	20.73	0.96	96.85
4	0.5	0.083333	2.54	-0.63	2.5	20.73	0.63	137.17
4	0.5	0.083333	2.54	-0.63	2	15.74	1.15	88.12
4	0.5	0.083333	2.54	-0.63	2	15.74	0.78	133.81
4	0.5	0.083333	2.54	-0.63	1.5	10.48	1.13	139.97
4	0.5	0.083333	2.54	-0.63	1.5	10.48	0.62	229.86
4	0.5	0.083333	2.08	-0.17	3.5	27.65	0.6	39.69
4	0.5	0.083333	2.08	-0.17	3.5	27.65	0.38	202.87

W (ft)	d_g (ft)	d_b (ft)	d_s (ft)	Z_c (ft)	T_p (s)	λ (ft)	H (ft)	F_V (lb)
4	0.5	0.083333	2.08	-0.17	3	23.4	0.73	62.29
4	0.5	0.083333	2.08	-0.17	3	23.4	0.48	111.11
4	0.5	0.083333	2.08	-0.17	2.5	19.08	0.8	90.07
4	0.5	0.083333	2.08	-0.17	2.5	19.08	0.62	159.24
4	0.5	0.083333	2.08	-0.17	2	14.63	1	101.87
4	0.5	0.083333	2.08	-0.17	2	14.63	0.65	165.76
4	0.5	0.083333	2.08	-0.17	1.5	9.97	0.86	127.2
4	0.5	0.083333	2.08	-0.17	1.5	9.97	0.59	162.04
4	0.5	0.083333	2.25	0	3.5	28.66	0.91	93.3
4	0.5	0.083333	2.25	0	3.5	28.66	0.57	225.25
4	0.5	0.083333	2.25	0	3	24.23	0.68	248.82
4	0.5	0.083333	2.25	0	3	24.23	0.59	359.37
4	0.5	0.083333	2.25	0	2.5	19.71	0.99	185.23
4	0.5	0.083333	2.25	0	2.5	19.71	0.73	277.13
4	0.5	0.083333	2.25	0	2	15.06	0.94	237.08
4	0.5	0.083333	2.25	0	2	15.06	0.76	343.61
4	0.5	0.083333	2.25	0	1.5	10.18	0.84	200.77
4	0.5	0.083333	2.25	0	1.5	10.18	0.72	268.86
4	0.5	0.083333	2.54	-0.29	3.5	30.31	0.98	111.58
4	0.5	0.083333	2.54	-0.29	3.5	30.31	0.61	216.26
4	0.5	0.083333	2.54	-0.29	3	25.57	0.88	133.32
4	0.5	0.083333	2.54	-0.29	3	25.57	0.6	228.12
4	0.5	0.083333	2.54	-0.29	2.5	20.73	0.92	120.2
4	0.5	0.083333	2.54	-0.29	2.5	20.73	0.63	271
4	0.5	0.083333	2.54	-0.29	2	15.74	1.41	150.45
4	0.5	0.083333	2.54	-0.29	2	15.74	1.1	280.22
4	0.5	0.083333	2.54	-0.29	1.5	10.48	1.08	220.79
4	0.5	0.083333	2.54	-0.29	1.5	10.48	0.95	286.69
4	0.5	0.083333	2.88	-0.63	3.5	32.05	0.89	70.02
4	0.5	0.083333	2.88	-0.63	3.5	32.05	0.52	128.78
4	0.5	0.083333	2.88	-0.63	3	26.97	0.74	77.87
4	0.5	0.083333	2.88	-0.63	3	26.97	0.61	151.22
4	0.5	0.083333	2.88	-0.63	2.5	21.78	0.75	91.27
4	0.5	0.083333	2.88	-0.63	2.5	21.78	0.57	138.39
4	0.5	0.083333	2.88	-0.63	2	16.41	1.32	91.83
4	0.5	0.083333	2.88	-0.63	2	16.41	1.21	185.32
4	0.5	0.083333	2.88	-0.63	1.5	10.76	1.01	143.1
4	0.5	0.083333	2.88	-0.63	1.5	10.76	0.97	196.64
4	0.5	0.083333	2.42	-0.17	3.5	29.62	0.97	60.28
4	0.5	0.083333	2.42	-0.17	3.5	29.62	0.58	144.51

W (ft)	d_g (ft)	d_b (ft)	d_s (ft)	Z_c (ft)	T_p (s)	λ (ft)	H (ft)	F_V (lb)
4	0.5	0.083333	2.42	-0.17	3	25.01	0.85	104.74
4	0.5	0.083333	2.42	-0.17	3	25.01	0.6	219.76
4	0.5	0.083333	2.42	-0.17	2.5	20.3	0.96	151.6
4	0.5	0.083333	2.42	-0.17	2.5	20.3	0.76	249.92
4	0.5	0.083333	2.42	-0.17	2	15.46	1.14	114.69
4	0.5	0.083333	2.42	-0.17	2	15.46	0.8	249.27
4	0.5	0.083333	2.42	-0.17	1.5	10.36	1.02	156.02
4	0.5	0.083333	2.42	-0.17	1.5	10.36	0.78	190.69
4	0.5	0.083333	2.58	0	3.5	30.54	0.97	96.52
4	0.5	0.083333	2.58	0	3.5	30.54	0.55	217.1
4	0.5	0.083333	2.58	0	3	25.75	0.79	224.29
4	0.5	0.083333	2.58	0	3	25.75	0.52	382.22
4	0.5	0.083333	2.58	0	2.5	20.87	0.83	255.87
4	0.5	0.083333	2.58	0	2.5	20.87	0.74	370.92
4	0.5	0.083333	2.58	0	2	15.83	1.15	247.25
4	0.5	0.083333	2.58	0	2	15.83	1.26	308.24
4	0.5	0.083333	2.58	0	1.5	10.52	0.99	248.67
4	0.5	0.083333	2.58	0	1.5	10.52	0.85	320.25
4	0.5	0.083333	2.88	-0.29	3.5	32.05	1	121.05
4	0.5	0.083333	2.88	-0.29	3.5	32.05	0.72	254.24
4	0.5	0.083333	2.88	-0.29	3	26.97	1.04	156
4	0.5	0.083333	2.88	-0.29	3	26.97	0.77	328.29
4	0.5	0.083333	2.88	-0.29	2.5	21.78	0.92	187.29
4	0.5	0.083333	2.88	-0.29	2.5	21.78	0.7	367.99
4	0.5	0.083333	2.88	-0.29	2	16.41	1.45	202.82
4	0.5	0.083333	2.88	-0.29	2	16.41	1.32	275.27
4	0.5	0.083333	2.88	-0.29	1.5	10.76	1.14	299.39
4	0.5	0.083333	2.88	-0.29	1.5	10.76	1.03	269.18
4	0.5	0.083333	1.42	0.17	3.5	22.93	0.77	6.36
4	0.5	0.083333	1.42	0.17	3.5	22.93	0.45	89.03
4	0.5	0.083333	1.42	0.17	3	19.59	0.75	0.9
4	0.5	0.083333	1.42	0.17	3	19.59	0.48	89.93
4	0.5	0.083333	1.42	0.17	2.5	16.1	0.86	117.43
4	0.5	0.083333	1.42	0.17	2.5	16.1	0.64	120.32
4	0.5	0.083333	1.42	0.17	2	12.53	0.71	49.58
4	0.5	0.083333	1.42	0.17	2	12.53	0.59	75.19
4	0.5	0.083333	1.42	0.17	1.5	8.82	0.76	30.59
4	0.5	0.083333	1.42	0.17	1.5	8.82	0.79	62.27
4	0.5	0.083333	1.58	0	3.5	24.24	1.01	112.02
4	0.5	0.083333	1.58	0	3.5	24.24	0.64	278.93

W (ft)	d_g (ft)	d_b (ft)	d_s (ft)	Z_c (ft)	T_p (s)	λ (ft)	H (ft)	F_V (lb)
4	0.5	0.083333	1.58	0	3	20.64	0.75	77.52
4	0.5	0.083333	1.58	0	3	20.64	0.55	268.89
4	0.5	0.083333	1.58	0	2.5	16.92	1.04	174.19
4	0.5	0.083333	1.58	0	2.5	16.92	0.71	247.44
4	0.5	0.083333	1.58	0	2	13.12	0.66	187.22
4	0.5	0.083333	1.58	0	2	13.12	0.55	264.27
4	0.5	0.083333	1.58	0	1.5	9.17	0.76	163.26
4	0.5	0.083333	1.58	0	1.5	9.17	0.84	201.03
4	0.5	0.083333	1.88	-0.29	3.5	26.31	0.79	97.34
4	0.5	0.083333	1.88	-0.29	3.5	26.31	0.62	207.12
4	0.5	0.083333	1.88	-0.29	3	22.31	0.54	77.68
4	0.5	0.083333	1.88	-0.29	3	22.31	0.42	196.41
4	0.5	0.083333	1.88	-0.29	2.5	18.23	0.92	112.87
4	0.5	0.083333	1.88	-0.29	2.5	18.23	0.87	199.45
4	0.5	0.083333	1.88	-0.29	2	14.05	0.82	126.02
4	0.5	0.083333	1.88	-0.29	2	14.05	0.56	228.09
4	0.5	0.083333	1.88	-0.29	1.5	9.67	0.81	254.94
4	0.5	0.083333	1.88	-0.29	1.5	9.67	0.77	323.63
4	0.5	0.083333	2.21	-0.63	3.5	28.41	1.14	97.95
4	0.5	0.083333	2.21	-0.63	3.5	28.41	0.65	157.97
4	0.5	0.083333	2.21	-0.63	3	24.02	0.72	100.39
4	0.5	0.083333	2.21	-0.63	3	24.02	0.53	157.64
4	0.5	0.083333	2.21	-0.63	2.5	19.55	0.85	87.08
4	0.5	0.083333	2.21	-0.63	2.5	19.55	0.69	159.32
4	0.5	0.083333	2.21	-0.63	2	14.96	0.77	112.06
4	0.5	0.083333	2.21	-0.63	2	14.96	0.77	126.75
4	0.5	0.083333	2.21	-0.63	1.5	10.13	0.94	162.23
4	0.5	0.083333	2.21	-0.63	1.5	10.13	0.9	154.59
4	0.5	0.083333	1.75	0.17	3.5	25.45	0.65	34.95
4	0.5	0.083333	1.75	0.17	3.5	25.45	0.72	141.33
4	0.5	0.083333	1.75	0.17	3	21.62	0.61	7.77
4	0.5	0.083333	1.75	0.17	3	21.62	0.58	124.97
4	0.5	0.083333	1.75	0.17	2.5	17.69	0.85	53.35
4	0.5	0.083333	1.75	0.17	2.5	17.69	0.68	123.6
4	0.5	0.083333	1.75	0.17	2	13.67	0.78	64.33
4	0.5	0.083333	1.75	0.17	2	13.67	0.81	138.08
4	0.5	0.083333	1.75	0.17	1.5	9.47	0.79	40.34
4	0.5	0.083333	1.75	0.17	1.5	9.47	0.81	87.03
4	0.5	0.083333	1.92	0	3.5	26.59	0.86	93.01
4	0.5	0.083333	1.92	0	3.5	26.59	0.58	212.76

W (ft)	d_g (ft)	d_b (ft)	d_s (ft)	Z_c (ft)	T_p (s)	λ (ft)	H (ft)	F_V (lb)
4	0.5	0.083333	1.92	0	3	22.54	0.71	150.11
4	0.5	0.083333	1.92	0	3	22.54	0.53	356.06
4	0.5	0.083333	1.92	0	2.5	18.4	0.83	155.15
4	0.5	0.083333	1.92	0	2.5	18.4	0.71	347.52
4	0.5	0.083333	1.92	0	2	14.17	0.84	238.48
4	0.5	0.083333	1.92	0	2	14.17	0.91	306.92
4	0.5	0.083333	1.92	0	1.5	9.74	0.8	177.94
4	0.5	0.083333	1.92	0	1.5	9.74	0.69	274.2
4	0.5	0.083333	2.21	-0.29	3.5	28.41	0.8	111.37
4	0.5	0.083333	2.21	-0.29	3.5	28.41	0.62	196.61
4	0.5	0.083333	2.21	-0.29	3	24.02	0.64	129.52
4	0.5	0.083333	2.21	-0.29	3	24.02	0.48	239.33
4	0.5	0.083333	2.21	-0.29	2.5	19.55	0.88	132.14
4	0.5	0.083333	2.21	-0.29	2.5	19.55	0.82	195.61
4	0.5	0.083333	2.21	-0.29	2	14.96	1.12	205.02
4	0.5	0.083333	2.21	-0.29	2	14.96	0.99	268.48
4	0.5	0.083333	2.21	-0.29	1.5	10.13	0.91	272.77
4	0.5	0.083333	2.21	-0.29	1.5	10.13	0.85	280.39
4	0.5	0.083333	2.54	-0.63	3.5	30.31	1.06	110.19
4	0.5	0.083333	2.54	-0.63	3.5	30.31	0.79	169.47
4	0.5	0.083333	2.54	-0.63	3	25.57	0.94	101.01
4	0.5	0.083333	2.54	-0.63	3	25.57	0.62	176.34
4	0.5	0.083333	2.54	-0.63	2.5	20.73	0.8	103.88
4	0.5	0.083333	2.54	-0.63	2.5	20.73	0.65	166.32
4	0.5	0.083333	2.54	-0.63	2	15.74	1.42	91.96
4	0.5	0.083333	2.54	-0.63	2	15.74	0.96	142.48
4	0.5	0.083333	2.54	-0.63	1.5	10.48	1.03	193.86
4	0.5	0.083333	2.54	-0.63	1.5	10.48	1.02	203.54
4	0.5	0.083333	2.08	-0.17	3.5	27.65	0.83	83.75
4	0.5	0.083333	2.08	-0.17	3.5	27.65	0.53	175.44
4	0.5	0.083333	2.08	-0.17	3	23.4	0.92	68.12
4	0.5	0.083333	2.08	-0.17	3	23.4	0.52	236.43
4	0.5	0.083333	2.08	-0.17	2.5	19.08	0.86	84.79
4	0.5	0.083333	2.08	-0.17	2.5	19.08	0.64	160
4	0.5	0.083333	2.08	-0.17	2	14.63	0.89	112.59
4	0.5	0.083333	2.08	-0.17	2	14.63	0.75	169.92
4	0.5	0.083333	2.08	-0.17	1.5	9.97	0.91	126.55
4	0.5	0.083333	2.08	-0.17	1.5	9.97	0.81	141.69
4	0.5	0.083333	2.25	0	3.5	28.66	1.07	91.5
4	0.5	0.083333	2.25	0	3.5	28.66	0.71	244.19

W (ft)	d_g (ft)	d_b (ft)	d_s (ft)	Z_c (ft)	T_p (s)	λ (ft)	H (ft)	F_V (lb)
4	0.5	0.083333	2.25	0	3	24.23	0.87	188.36
4	0.5	0.083333	2.25	0	3	24.23	0.6	362.14
4	0.5	0.083333	2.25	0	2.5	19.71	1.01	233.24
4	0.5	0.083333	2.25	0	2.5	19.71	0.86	305.83
4	0.5	0.083333	2.25	0	2	15.06	1.04	239.02
4	0.5	0.083333	2.25	0	2	15.06	0.9	351.81
4	0.5	0.083333	2.25	0	1.5	10.18	1.01	193.79
4	0.5	0.083333	2.25	0	1.5	10.18	0.96	278.17
4	0.5	0.083333	2.54	-0.29	3.5	30.31	1.14	108.02
4	0.5	0.083333	2.54	-0.29	3.5	30.31	0.69	268.11
4	0.5	0.083333	2.54	-0.29	3	25.57	0.92	103.83
4	0.5	0.083333	2.54	-0.29	3	25.57	0.6	238.22
4	0.5	0.083333	2.54	-0.29	2.5	20.73	1.03	138.54
4	0.5	0.083333	2.54	-0.29	2.5	20.73	0.72	245.02
4	0.5	0.083333	2.54	-0.29	2	15.74	1.28	153.91
4	0.5	0.083333	2.54	-0.29	2	15.74	1.02	267.7
4	0.5	0.083333	2.54	-0.29	1.5	10.48	1.08	272.36
4	0.5	0.083333	2.54	-0.29	1.5	10.48	1.07	404.65
4	0.5	0.083333	2.88	-0.63	3.5	32.05	1.11	112.71
4	0.5	0.083333	2.88	-0.63	3.5	32.05	0.75	185.5
4	0.5	0.083333	2.88	-0.63	3	26.97	1.05	93.27
4	0.5	0.083333	2.88	-0.63	3	26.97	0.78	164.89
4	0.5	0.083333	2.88	-0.63	2.5	21.78	0.94	107.53
4	0.5	0.083333	2.88	-0.63	2.5	21.78	0.61	157.85
4	0.5	0.083333	2.88	-0.63	2	16.41	1.56	126.74
4	0.5	0.083333	2.88	-0.63	2	16.41	1.35	190.47
4	0.5	0.083333	2.88	-0.63	1.5	10.76	1.28	155.15
4	0.5	0.083333	2.88	-0.63	1.5	10.76	1.09	217.87
4	0.5	0.083333	2.42	-0.17	3.5	29.62	0.85	123.68
4	0.5	0.083333	2.42	-0.17	3.5	29.62	0.57	156.44
4	0.5	0.083333	2.42	-0.17	3	25.01	0.82	78.68
4	0.5	0.083333	2.42	-0.17	3	25.01	0.63	214.62
4	0.5	0.083333	2.42	-0.17	2.5	20.3	1.05	108.46
4	0.5	0.083333	2.42	-0.17	2.5	20.3	0.72	174.06
4	0.5	0.083333	2.42	-0.17	2	15.46	1.19	146.35
4	0.5	0.083333	2.42	-0.17	2	15.46	0.98	226.61
4	0.5	0.083333	2.42	-0.17	1.5	10.36	1.1	146.58
4	0.5	0.083333	2.42	-0.17	1.5	10.36	1.05	166.82
4	0.5	0.083333	2.58	0	3.5	30.54	0.82	128.73
4	0.5	0.083333	2.58	0	3.5	30.54	0.63	232.05

W (ft)	d_g (ft)	d_b (ft)	d_s (ft)	Z_c (ft)	T_p (s)	λ (ft)	H (ft)	F_V (lb)
4	0.5	0.083333	2.58	0	3	25.75	0.86	335.92
4	0.5	0.083333	2.58	0	3	25.75	0.55	354.55
4	0.5	0.083333	2.58	0	2.5	20.87	1.04	298.82
4	0.5	0.083333	2.58	0	2.5	20.87	0.78	347.5
4	0.5	0.083333	2.58	0	2	15.83	1.23	348.52
4	0.5	0.083333	2.58	0	2	15.83	1.14	380.72
4	0.5	0.083333	2.58	0	1.5	10.52	1.03	330.23
4	0.5	0.083333	2.58	0	1.5	10.52	1.01	293.63
4	0.5	0.083333	2.88	-0.29	3.5	32.05	1.2	124.44
4	0.5	0.083333	2.88	-0.29	3.5	32.05	0.78	209.24
4	0.5	0.083333	2.88	-0.29	3	26.97	1.04	173.38
4	0.5	0.083333	2.88	-0.29	3	26.97	0.81	267.1
4	0.5	0.083333	2.88	-0.29	2.5	21.78	0.97	216.4
4	0.5	0.083333	2.88	-0.29	2.5	21.78	0.63	330.97
4	0.5	0.083333	2.88	-0.29	2	16.41	1.64	231.9
4	0.5	0.083333	2.88	-0.29	2	16.41	1.39	266.94
4	0.5	0.083333	2.88	-0.29	1.5	10.76	1.2	368.38
4	0.5	0.083333	2.88	-0.29	1.5	10.76	1.11	394.33

Appendix II
Validation of the FSI Model Data

This appendix presents the selected simulations from the experimental test data that were used to validate the FSI model. The forces are scaled to the prototype size using the Froude number. The selected cases cover a wide range of hazard parameters. These cases for two different scale factors are presented in Table II-1 and Table II-2 respectively.

Table II-1. First set of data for FSI validation simulation. The prototype span length for this set is 17.25m and the scale factor is 5.

						Experimental		Numerical	
W (m)	d_g (m)	d_b (m)	d_s (m)	Z_c (m)	T_p (s)	H (m)	F_V (kN)	F_V (kN)	*Error* (%)
9.7	1.15	0.25	8.05	1.40	5.59	3.10	466.25	529.11	13.5
9.7	1.15	0.25	8.05	1.40	5.59	2.85	217.50	189.44	-12.9
9.7	1.15	0.25	8.75	0.70	4.47	2.20	362.50	413.25	14.0
9.7	1.15	0.25	8.05	1.40	8.94	3.50	815.00	900.58	10.5
9.7	1.15	0.25	8.05	0.70	6.71	2.15	753.80	663.34	-12.1
9.7	1.15	0.25	9.45	0.00	7.83	3.60	2251.30	2470.61	11.2
9.7	1.15	0.25	9.45	0.00	8.94	3.30	1886.20	1621.12	-14.1
9.7	1.15	0.25	10.15	-0.70	8.94	7.87	1673.80	1672.52	-0.51
9.7	1.15	0.25	10.15	-0.70	8.94	2.10	1535.00	1381.50	-10.1
9.7	1.15	0.25	10.85	-1.40	6.71	2.80	1312.50	1380.80	5.2
9.7	1.15	0.25	8.05	1.40	6.71	3.90	1461.25	1592.81	9.1
9.7	1.15	0.25	8.05	1.40	5.59	3.40	545.00	592.41	8.7
9.7	1.15	0.25	10.85	-1.40	6.71	1.65	775.00	885.82	14.3
9.7	1.15	0.25	10.85	-1.40	4.47	2.70	910.00	830.65	-8.7
9.7	1.15	0.25	9.45	0	6.71	1.60	805.00	897.56	11.3
9.7	1.15	0.25	9.45	0	4.47	1.05	395.00	436.48	10.5

Table II-2. Second set of data for FSI validation simulation. The prototype span length for this set is 4.88m and the scale factor is 8.

						Experimental		Numerical	
W (m)	d_g (m)	d_b (m)	d_s (m)	Z_c (m)	T_p (s)	H (m)	F_V (kN)	F_V (kN)	*Error* (%)
9.75	1.21	0.20	3.46	0.41	9.90	1.88	307.40	278.13	-9.5
9.75	1.21	0.20	3.46	0.41	9.90	1.10	140.08	134.05	-4.3
9.75	1.21	0.20	3.46	0.41	8.49	1.83	203.94	217.76	6.8
9.75	1.21	0.20	3.46	0.41	8.49	1.17	196.76	195.77	-0.5
9.75	1.21	0.20	3.46	0.41	7.07	2.10	314.87	338.52	7.5
9.75	1.21	0.20	3.46	0.41	7.07	1.56	163.52	198.02	21.1
9.75	1.21	0.20	3.46	0.41	5.66	1.73	271.33	261.74	-3.5
9.75	1.21	0.20	3.46	0.41	5.66	1.44	111.60	108.80	-2.5
9.75	1.21	0.20	3.46	0.41	4.24	1.85	226.70	242.94	7.2
9.75	1.21	0.20	3.46	0.41	4.24	1.93	196.51	182.50	-7.1
9.75	1.21	0.20	3.85	0.00	9.90	2.46	363.84	345.98	-4.9
9.75	1.21	0.20	3.85	0.00	9.90	1.56	250.51	225.25	-10.1
9.75	1.21	0.20	3.85	0.00	8.49	1.83	541.67	581.75	7.4
9.75	1.21	0.20	3.85	0.00	8.49	1.34	444.27	444.57	0.1
9.75	1.21	0.20	3.85	0.00	7.07	2.54	454.40	412.10	-9.3
9.75	1.21	0.20	3.85	0.00	7.07	1.73	360.97	385.46	6.8
9.75	1.21	0.20	3.85	0.00	5.66	1.61	560.42	575.30	2.7
9.75	1.21	0.20	3.85	0.00	5.66	1.34	350.85	354.80	1.1
9.75	1.21	0.20	3.85	0.00	4.24	1.85	489.74	483.82	-1.2
9.75	1.21	0.20	3.85	0.00	4.24	2.05	401.14	427.21	6.5
9.75	1.21	0.20	4.58	-0.71	9.90	1.93	293.94	269.28	-8.4
9.75	1.21	0.20	4.58	-0.71	9.90	1.56	227.95	235.51	3.3
9.75	1.21	0.20	4.58	-0.71	8.49	1.32	288.33	303.76	5.3
9.75	1.21	0.20	4.58	-0.71	8.49	1.02	212.94	207.04	-2.8
9.75	1.21	0.20	4.58	-0.71	7.07	2.24	286.67	315.12	9.9
9.75	1.21	0.20	4.58	-0.71	7.07	2.12	285.42	298.35	4.5
9.75	1.21	0.20	4.58	-0.71	5.66	2.00	281.61	304.18	8.0
9.75	1.21	0.20	4.58	-0.71	5.66	1.37	230.76	247.54	7.3
9.75	1.21	0.20	4.58	-0.71	4.24	1.98	257.89	241.46	-6.4
9.75	1.21	0.20	4.58	-0.71	4.24	1.88	298.52	271.97	-8.9
9.75	1.21	0.20	5.39	-1.54	9.90	2.78	258.96	248.55	-4.0
9.75	1.21	0.20	5.39	-1.54	9.90	1.58	131.62	131.06	-0.4
9.75	1.21	0.20	5.39	-1.54	7.07	2.07	207.77	212.56	2.3
9.75	1.21	0.20	5.39	-1.54	8.49	1.76	231.23	253.13	9.5

Appendix III
Wave and Surge Parameters Extracted from NOAA for Intensity Measure Study

Chapter 5 utilizes the data presented in this appendix in order to define the most influential hazard parameters (intensity measures). The wave and surge data is extracted from NOAA (2010) "National Data Buoy Center." For each scenario, ten different relative surge elevations are generated to reach to the number of 300 simulations. The relative surge elevation is selected uniformly from the range of -1m to $0.6H_{max}$ for each scenario.

Table III-1. Wave and surge parameters extracted from NOAA (2010) database for five different hurricane events.

Hurricane	No.	$H_{\max}$ (m)	T_p (s)	λ (m)
	1	1.96848	6.2	166.3312
Floyd	2	2.29656	3.8	73.36745
	3	2.263752	5.5	139.7522
	4	5.90544	5.9	155.0827
	5	6.660024	6.23	167.4439
Danny	6	7.87392	7.18	201.6002
	7	9.612744	7.48	211.9951
	8	10.59698	8.4	242.9632
	9	6	6	158.8566
	10	6.5	6	158.8566
	11	7	5.9	155.0827
	12	8	6.5	177.3606
Katrina	13	9.18624	7.5	212.6823
	14	15.09168	14	418.2445
	15	16.404	14	418.2445
	16	17.06016	14.1	421.2916
	17	18.0444	14.1	421.2916

Hurricane	No.	$H_{\max}$ (m)	T_p (s)	λ (m)
Rita	18	7.54584	14.1	421.2916
	19	10.49856	14.1	421.2916
	20	13.1232	14.1	421.2916
	21	11.81088	14.1	421.2916
	22	14.7636	7.6	216.1079
Ike	23	14.7636	14.1	421.2916
	24	15.41976	5.9	155.0827
	25	17.06016	6.1	162.6061
	26	17.71632	6.1	162.6061
	27	18.0444	6.2	166.3312
	28	20.99712	6.2	166.3312
	29	22.9656	6.4	173.7082
	30	23.94984	6.4	173.7082

Appendix IV
Anchorage in Concrete

Details of connection strength calculation that is used in Section 6.1 are provided in this appendix. Concrete breakout strength is estimated based on a failure cone with approximately 35° from the base of the anchor bolt (ACI 2008). Therefore, a full failure surface can be developed if the anchor has at least a distance of $1.5h_{ef}$ from the edges. h_{ef} is the effective length of the anchor, as shown in Figure IV-1.

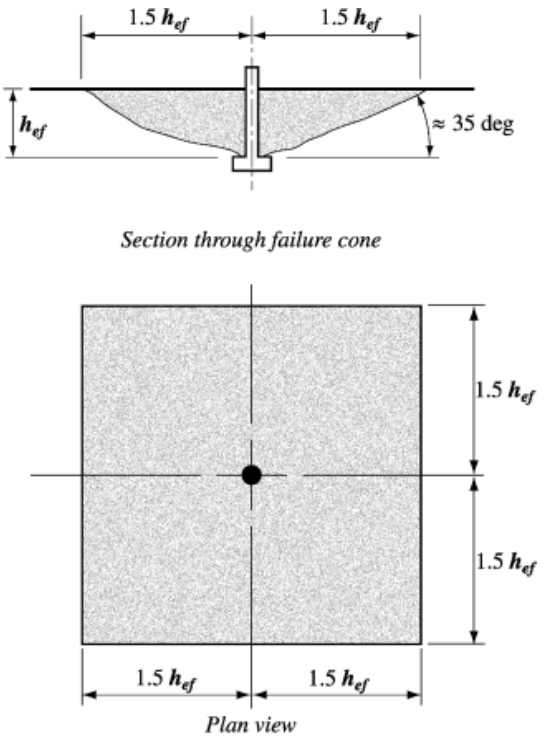

Figure IV-1. Failure cone for concrete breakout strength, A_{No} (ACI 2008).

Concrete breakout strength, as presented in Chapter 6 is as follows (ACI 2008):

$$N_{cb} = \frac{A_N}{A_{No}} \psi_2 \psi_3 N_b \tag{A-1}$$

where $_2$ is the modification factor that is equal to 1.25 for cast-in place and 1.4 for post-installed bolts. $_3$ is the modification for post-installed anchors. The region of study does not have any post-installed anchor; therefore, the value of $_3$ is equal to 1. N_b is defined as (ACI 2008):

$$N_b = k_c \lambda_c \sqrt{f'_c} h_{ef}^{1.5} \tag{A-2}$$

k_c is 24 for cast-in anchor and 17 for post-installed anchors. $_c$ takes into account the effect of concrete density and is equal to 1 for normal weight concrete.

The concrete pullout strength, which is the crushing strength of the concrete under the bolt head, is as follows (ACI 2008):

$$N_{pn} = \psi_4 N_p \tag{A-3}$$

where $_4$ is equal to 1.4 for in a region of concrete where analysis indicates no cracking, and 1 otherwise. N_p is defined as (ACI 2008):

$$N_p = 8 A_{brg} f'_c \tag{A-4}$$

where A_{brg} is the bearing area of the anchor.

Appendix V
Realizations of Random Variables

This appendix provides realizations of random variables that are generated for the reliability assessment of a case study simply supported coastal bridge that was implemented in Chapter 6 and Chapter 7. The 256 realizations are generated using quasi-Monte Carlo sampling technique. Table V-1 shows the random variable realizations.

Table V-1. Quasi-Monte Carlo realizations of random variables.

T_p (s)	f_y (MPa)	f'_c (MPa)	c (kPa)	ρ_C (kg/m^3)	μ
7.43821	377.2933	25.34459	103.7088	2641.924	0.620159
5.56321	436.3576	26.72182	89.98535	2367.922	0.682659
7.06321	391.715	20.72631	121.8759	2507.741	0.932659
6.31321	334.4308	30.62859	82.48615	2429.108	0.557659
7.81321	413.3458	24.00351	111.5773	2286.784	0.807659
5.09446	372.4004	25.68001	96.77303	2375.774	0.885784
6.59446	421.2749	18.5164	140.976	2523.239	0.635784
5.84446	448.3853	28.78715	67.02612	2437.09	0.760784
7.34446	400.2835	22.93542	101.9225	2300.66	0.510784
5.46946	433.0146	24.34287	88.22292	2406.112	0.698284
6.96946	388.5644	31.5569	118.9148	2212.469	0.948284
6.21946	410.7619	21.24634	80.31254	2342.725	0.573284
7.71946	481.7841	27.09004	109.465	2472.642	0.823284
5.28196	459.8576	20.13285	95.08967	2270.025	0.542034
6.78196	405.5853	26.36611	134.2151	2421.322	0.792034
6.03196	381.4692	23.65766	75.14431	2494.636	0.667034
7.53196	426.8946	29.91094	105.5509	2359.848	0.917034
5.65696	394.691	27.88078	91.70782	2571.376	0.854534
7.15696	439.9666	22.14759	125.2563	2391.055	0.604534
6.40696	415.9481	25.0113	84.50078	2323.54	0.979534
7.90696	357.4269	11.94082	113.8289	2453.935	0.729534
5.047585	401.6288	17.92286	98.46586	2425.194	0.643597
6.547585	450.8613	25.5119	152.2549	2278.866	0.893597

T_p (s)	f_y (MPa)	f'_c (MPa)	c (kPa)	ρ_c (kg/m^3)	μ
5.797585	422.6456	22.74602	63.31034	2363.917	0.518597
7.297585	374.9594	28.54565	101.046	2500.953	0.768597
5.422585	495.4423	31.05666	87.32125	2394.826	0.956097
6.922585	412.0525	24.17384	117.5535	2594.291	0.706097
6.172585	390.1648	26.90414	79.14509	2458.397	0.831097
7.672585	434.6572	20.99383	108.4519	2328.598	0.581097
5.235085	428.3676	27.67468	94.24821	2532.356	0.799847
6.735085	383.3718	21.93548	131.5759	2379.637	0.549847
5.985085	406.8856	34.27238	73.55682	2306.874	0.924847
7.485085	463.6851	24.84481	104.622	2441.176	0.674847
5.610085	362.37	23.4815	90.8506	2233.046	0.612347
7.110085	417.2612	29.59968	123.5041	2409.885	0.862347
6.360085	441.8972	19.79708	83.51002	2477.753	0.737347
7.860085	396.1277	26.19193	112.6836	2347.158	0.987347
5.141335	446.0855	23.83155	97.61761	2318.26	0.815472
6.641335	398.9203	30.25105	145.6723	2449.587	0.565472
5.891335	369.5424	20.4407	69.65417	2555.408	0.940472
7.391335	419.9223	26.54261	102.8096	2387.271	0.690472
5.516335	409.4719	25.17781	89.11016	2488.704	0.502972
7.016335	473.9303	15.95774	120.3514	2355.706	0.752972
6.266335	431.4227	28.09389	81.42291	2259.919	0.627972
7.766335	386.9057	22.35281	110.5057	2417.484	0.877972
5.328835	379.4516	29.04154	95.93083	2338.167	0.721722
6.828835	425.4523	23.12081	137.2827	2467.73	0.971722
6.078835	456.5253	25.84919	76.58224	2402.348	0.596722
7.578835	404.2772	19.00507	106.4973	2175.79	0.846722
5.703835	414.6436	21.48625	92.55877	2433.07	0.909222
7.203835	350.3081	27.28003	127.1592	2293.999	0.659222
6.453835	393.2218	24.51085	85.46352	2371.871	0.784222
7.953835	438.1241	32.16918	115.0183	2515.115	0.534222
5.024147	389.3714	24.92807	99.31911	2519.07	0.530315
6.524147	433.8291	35.49832	163.8659	2373.828	0.780315
5.774147	487.35	22.04246	60.44114	2297.391	0.655315
7.274147	411.407	27.77691	100.6113	2435.072	0.905315
5.399147	421.9578	26.27875	86.86418	2197.754	0.842815
6.899147	373.7119	19.96889	116.8979	2404.229	0.592815
6.149147	400.9582	29.75213	78.53605	2470.163	0.967815
7.649147	449.599	23.56989	107.9548	2340.463	0.717815
5.211647	440.9201	28.66492	93.82693	2419.399	0.936565
6.711647	395.4131	22.84126	130.3787	2265.159	0.686565

T_p (s)	f_y (MPa)	f'_c (MPa)	c (kPa)	ρ_c (kg/m^3)	μ
5.961647	360.0715	25.59584	72.68996	2357.787	0.811565
7.461647	416.6034	18.2361	104.1636	2491.627	0.561565
5.586647	406.2362	21.1218	90.4191	2389.165	0.749065
7.086647	461.6984	26.99661	122.6759	2562.83	0.999065
6.336647	427.627	24.2585	83.00259	2451.748	0.624065
7.836647	382.4335	31.29589	112.1259	2320.93	0.874065
5.117897	430.6438	19.22223	97.19494	2349.332	0.95219
6.617897	386.0515	25.93427	143.1625	2480.392	0.70219
5.867897	408.8265	23.21215	68.42644	2411.777	0.82719
7.367897	470.8966	29.17433	102.3646	2240.986	0.57719
5.492897	367.9672	32.54102	88.66819	2443.247	0.63969
6.992897	419.252	24.59454	119.6229	2309.839	0.88969
6.242897	444.9916	27.37673	80.87418	2381.556	0.51469
7.742897	398.231	21.60209	109.9817	2537.4	0.76469
5.305397	392.4734	26.63185	95.5102	2331.054	0.60844
6.805397	437.232	20.586	135.6856	2460.676	0.85844
6.055397	413.994	30.43446	75.8793	2611.81	0.73344
7.555397	344.7573	23.91775	106.0218	2396.708	0.98344
5.680397	455.0011	22.45312	92.13398	2504.282	0.79594
7.180397	403.6196	28.2034	126.1869	2365.927	0.54594
6.430397	378.392	16.63334	84.98537	2282.925	0.92094
7.930397	424.7415	25.26115	114.4177	2427.145	0.67094
5.071022	477.4767	25.42816	98.89178	2447.451	0.710003
6.571022	410.1169	17.56564	156.9757	2315.526	0.960003
5.821022	387.7429	28.4291	65.37331	2385.372	0.585003
7.321022	432.2127	22.64964	101.483	2548.813	0.835003
5.446022	399.6043	24.08886	87.77404	2353.604	0.897503
6.946022	447.2155	30.83523	118.2254	2485.862	0.647503
6.196022	420.5965	20.86212	79.73668	2415.576	0.772503
7.696022	371.0147	26.81256	108.9552	2254.225	0.522503
5.258522	354.2764	21.82653	94.66906	2465.34	0.866253
6.758522	415.2949	27.57397	132.8505	2335.836	0.616253
6.008522	439.0352	24.76149	74.37225	2122.861	0.991253
7.508522	393.9607	33.52958	105.0844	2400.468	0.741253
5.633522	426.1698	29.45294	91.2801	2290.469	0.553753
7.133522	380.4762	23.39244	124.3632	2431.082	0.803753
6.383522	404.9323	26.1056	84.0092	2511.346	0.678753
7.883522	458.1393	19.61633	113.2511	2369.903	0.928753
5.164772	412.6987	30.07693	98.04119	2274.578	0.756878
6.664772	511.9126	23.74487	148.6307	2423.253	0.506878

T_p (s)	f_y (MPa)	f'_c (MPa)	c (kPa)	ρ_c (kg/m^3)	μ
5.914772	435.4997	26.45405	70.75585	2497.742	0.881878
7.414772	390.9457	20.28986	103.2576	2361.891	0.631878
5.539772	452.1778	14.92378	89.54913	2581.547	0.569378
7.039772	402.2957	25.09453	121.1017	2392.942	0.819378
6.289772	376.151	22.251	81.95989	2326.095	0.694378
7.789772	423.3385	27.9864	111.0374	2456.151	0.944378
5.352272	417.9217	23.02858	96.35172	2377.71	0.663128
6.852272	364.4156	28.91259	139.0337	2527.654	0.913128
6.102272	396.8352	18.77102	77.2572	2439.124	0.538128
7.602272	442.9	25.76445	106.9778	2303.817	0.788128
5.727272	384.2862	27.18449	92.98239	2407.997	0.975628
7.227272	429.1169	21.36775	128.1779	2223.766	0.725628
6.477272	465.8491	31.8453	85.93573	2344.956	0.850628
7.977272	407.5336	24.42697	115.6312	2475.171	0.600628
5.012428	407.2097	27.42555	99.74803	2362.906	0.868206
6.512428	464.7426	21.65907	177.4309	2499.334	0.618206
5.762428	428.7411	32.75089	58.33388	2424.222	0.993206
7.262428	383.8318	24.63633	100.3948	2276.753	0.743206
5.387428	442.3953	23.25751	86.63393	2457.27	0.555706
6.887428	396.4823	29.24227	116.5758	2327.353	0.805706
6.137428	363.4201	19.32537	78.22437	2393.884	0.680706
7.637428	417.5911	25.97695	107.7085	2587.507	0.930706
5.199928	422.9914	16.90468	93.61608	2305.358	0.711956
6.699928	375.5618	25.30285	129.8059	2440.148	0.961956
5.949928	401.9627	22.50275	72.23406	2529.966	0.586956
7.449928	451.5123	28.25896	103.9358	2378.674	0.836956
5.574928	390.5568	30.53008	90.20252	2476.455	0.899456
7.074928	435.0766	23.96068	122.2725	2346.06	0.649456
6.324928	501.63	26.67674	82.74554	2228.606	0.774456
7.824928	412.3755	20.65675	111.8505	2408.941	0.524456
5.106178	457.3203	29.83069	96.9839	2552.021	0.665081
6.606178	404.6051	23.61385	142.0346	2386.322	0.915081
5.856178	379.968	26.32236	67.75176	2316.901	0.540081
7.356178	425.8102	20.05179	102.1432	2448.516	0.790081
5.481178	393.5924	22.09524	88.44598	2257.135	0.977581
6.981178	438.5772	27.82864	119.2664	2416.529	0.727581
6.231178	414.969	24.96968	80.59505	2487.274	0.852581
7.731178	352.4248	36.75143	109.7224	2354.658	0.602581
5.293678	370.2903	24.30072	95.29994	2401.408	0.758831
6.793678	420.2589	31.42337	134.936	2157.988	0.508831

T_p (s)	f_y (MPa)	f'_c (MPa)	c (kPa)	ρ_c (kg/m^3)	μ
6.043678	446.6458	21.18448	75.5161	2337.006	0.883831
7.543678	399.2629	27.0432	105.7857	2466.53	0.633831
5.668678	431.8163	25.63789	91.92108	2370.889	0.571331
7.168678	387.3264	18.37985	125.7167	2513.209	0.821331
6.418678	409.7944	28.72565	84.74391	2432.075	0.696331
7.918678	475.6273	22.88847	114.1219	2292.252	0.946331
5.059303	424.3885	22.3021	98.67865	2244.579	0.922894
6.559303	377.8478	28.0399	154.4359	2412.725	0.672894
5.809303	403.2898	15.51036	64.40859	2481.735	0.797894
7.309303	454.2689	25.13616	101.2642	2350.409	0.547894
5.434303	340.7072	26.49825	87.54816	2540.07	0.735394
6.934303	413.6697	20.36601	117.8873	2382.512	0.985394
6.184303	436.7927	30.16291	79.44295	2311.29	0.610394
7.684303	392.0955	23.78827	108.7027	2444.29	0.860394
5.246803	397.8843	32.00216	94.45868	2397.648	0.516644
6.746803	444.4572	24.46894	132.2028	2624.154	0.766644
5.996803	418.9182	27.23212	73.97041	2461.828	0.641644
7.496803	367.1346	21.42735	104.8527	2332.265	0.891644
5.621803	469.525	18.89036	91.06559	2428.125	0.829144
7.121803	408.5035	25.80678	123.9296	2284.878	0.579144
6.371803	385.6176	23.07481	83.7606	2366.926	0.954144
7.871803	430.2584	28.97661	112.9661	2505.994	0.704144
5.153053	381.9547	20.92846	97.82927	2436.079	0.594769
6.653053	427.2598	26.85825	147.0849	2299.04	0.844769
5.903053	460.7613	24.1314	70.21863	2374.802	0.719769
7.403053	405.911	30.94393	103.0332	2521.126	0.969769
5.528053	416.2754	28.48705	89.33	2341.598	0.782269
7.028053	358.8003	22.69798	120.7237	2471.397	0.532269
6.278053	395.053	25.47001	81.69281	2405.171	0.907269
7.778053	440.4405	17.75065	110.7705	2205.68	0.657269
5.340553	448.9864	26.14871	96.14123	2493.12	0.938519
6.840553	400.6214	19.7079	138.1369	2358.82	0.688519
6.090553	373.0647	29.52563	76.923	2267.634	0.813519
7.590553	421.6158	23.43706	106.737	2420.359	0.563519
5.715553	411.0844	24.80316	92.77071	2322.242	0.626019
7.215553	484.3605	33.86724	127.6624	2452.838	0.876019
6.465553	433.4202	21.88127	85.70033	2566.938	0.501019
7.965553	388.9696	27.62414	115.3231	2390.111	0.751019
5.035866	437.6758	21.30742	99.53336	2388.219	0.809612
6.535866	392.8488	27.13713	169.0892	2559	0.559612

T_p (s)	f_y (MPa)	f'_c (MPa)	c (kPa)	ρ_c (kg/m^3)	μ
5.785866	347.8176	24.38495	62.02249	2450.664	0.934612
7.285866	414.3186	31.69725	100.8284	2319.603	0.684612
5.410866	403.9487	28.84945	87.09327	2418.441	0.622112
6.910866	455.7528	22.98212	117.2237	2262.59	0.872112
6.160866	425.096	25.7222	78.84287	2356.749	0.747112
7.660866	378.9264	18.64656	108.2026	2490.155	0.997112
5.223366	386.4808	25.05291	94.03763	2188.148	0.653362
6.723366	431.0319	14.04292	130.9683	2403.289	0.903362
5.973366	472.36	27.93336	73.13041	2468.941	0.528362
7.473366	409.1492	22.1995	104.3923	2339.319	0.778362
5.598366	419.5867	23.70134	90.63512	2517.068	0.965862
7.098366	368.7688	29.99299	123.0863	2372.851	0.715862
6.348366	398.5763	20.21217	83.25738	2295.711	0.840862
7.848366	445.5342	26.41	112.4035	2434.07	0.590862
5.129616	395.7713	23.34765	97.40617	2502.602	0.731487
6.629616	441.4056	29.38152	144.3706	2364.924	0.981487
5.879616	416.932	19.52218	69.05845	2280.922	0.606487
7.379616	361.2571	26.06261	102.5867	2426.168	0.856487
5.504616	462.6718	27.52415	88.88957	2329.832	0.918987
7.004616	406.5611	21.77127	119.9845	2459.533	0.668987
6.254616	382.9057	33.23848	81.15009	2602.212	0.793987
7.754616	427.9963	24.7198	110.2427	2395.767	0.543987
5.317116	434.2414	30.73021	95.72049	2442.209	0.825237
6.817116	389.7697	24.04623	136.4668	2308.368	0.575237
6.067116	411.7297	26.76709	76.2345	2380.597	0.950237
7.567116	490.9323	20.79475	106.2589	2534.832	0.700237
5.692116	374.3431	17.36537	92.34653	2348.248	0.512737
7.192116	422.3011	25.38635	126.6675	2479.065	0.762737
6.442116	450.2237	22.601	85.22521	2410.831	0.637737
7.942116	401.294	28.37179	114.7165	2237.155	0.887737
5.082741	355.9291	28.14839	99.10526	2302.252	0.9893
6.582741	415.6212	22.40315	160.0266	2438.105	0.7393
5.832741	439.4983	25.21946	66.23843	2525.413	0.8643
7.332741	394.3269	16.32287	101.7024	2376.743	0.6143
5.457741	426.5313	20.514	87.99895	2473.9	0.6768
6.957741	380.9764	26.58715	118.5678	2343.844	0.9268
6.207741	405.2591	23.87471	80.02648	2218.431	0.5518
7.707741	458.9844	30.34151	109.2092	2407.054	0.8018
5.270241	479.5129	24.55272	94.87939	2360.872	0.58305
6.770241	410.4394	32.34807	133.5207	2496.177	0.83305

T_p (s)	f_y (MPa)	f'_c (MPa)	c (kPa)	ρ_C (kg/m^3)	μ
6.020241	388.1556	21.54449	74.76327	2422.286	0.70805
7.520241	432.6121	27.32823	105.3171	2272.338	0.95805
5.645241	399.9444	25.89169	91.49417	2455.04	0.77055
7.145241	447.7952	19.11557	124.8053	2324.824	0.52055
6.395241	420.9352	29.10743	84.2559	2391.999	0.89555
7.895241	371.7175	23.16658	113.5387	2576.215	0.64555
5.176491	413.0221	26.95026	98.25338	2414.624	0.536175
6.676491	313.0623	21.05826	150.3401	2251.175	0.786175
5.926491	391.3317	31.17383	71.26909	2352.545	0.661175
7.426491	435.9267	24.21621	103.4828	2484.469	0.911175
5.551491	376.728	22.79378	89.76757	2384.42	0.848675
7.051491	423.687	28.60493	121.4857	2545.763	0.598675
6.301491	452.8584	18.08418	82.2243	2446.392	0.973675
7.801491	402.6279	25.55384	111.3063	2314.132	0.723675
5.363991	407.8571	19.88403	96.56231	2676.903	0.879925
6.863991	467.0103	26.23528	139.9781	2399.528	0.629925
6.113991	429.495	23.52577	77.58526	2334.655	0.754925
7.613991	384.7352	29.67515	107.22	2464.16	0.504925
5.738991	443.4117	34.78491	93.19383	2288.647	0.692425
7.238991	397.1864	24.88644	128.7064	2430.093	0.942425
6.488991	365.363	27.7256	86.16976	2509.524	0.567425
7.988991	418.2531	21.98921	115.9426	2368.914	0.817425
5.006569	366.7057	18.58223	99.96314	2221.167	0.701214
6.506569	418.7516	25.70109	202.5344	2407.526	0.951214
5.756569	444.1929	22.9588	49.92764	2474.534	0.576214
7.256569	397.7104	28.8182	100.0439	2344.401	0.826214
5.381569	430.0666	31.62617	86.25718	2526.525	0.888714
6.881569	385.3989	24.36391	116.0603	2377.227	0.638714
6.131569	408.342	27.11355	77.70678	2303.038	0.763714
7.631569	468.8697	21.27698	107.3112	2438.614	0.513714
5.194069	453.9098	26.38804	93.27307	2392.471	0.857464
6.694069	403.1246	20.17272	128.9081	2578.812	0.607464
5.944069	377.5719	29.95174	71.45595	2455.595	0.982464